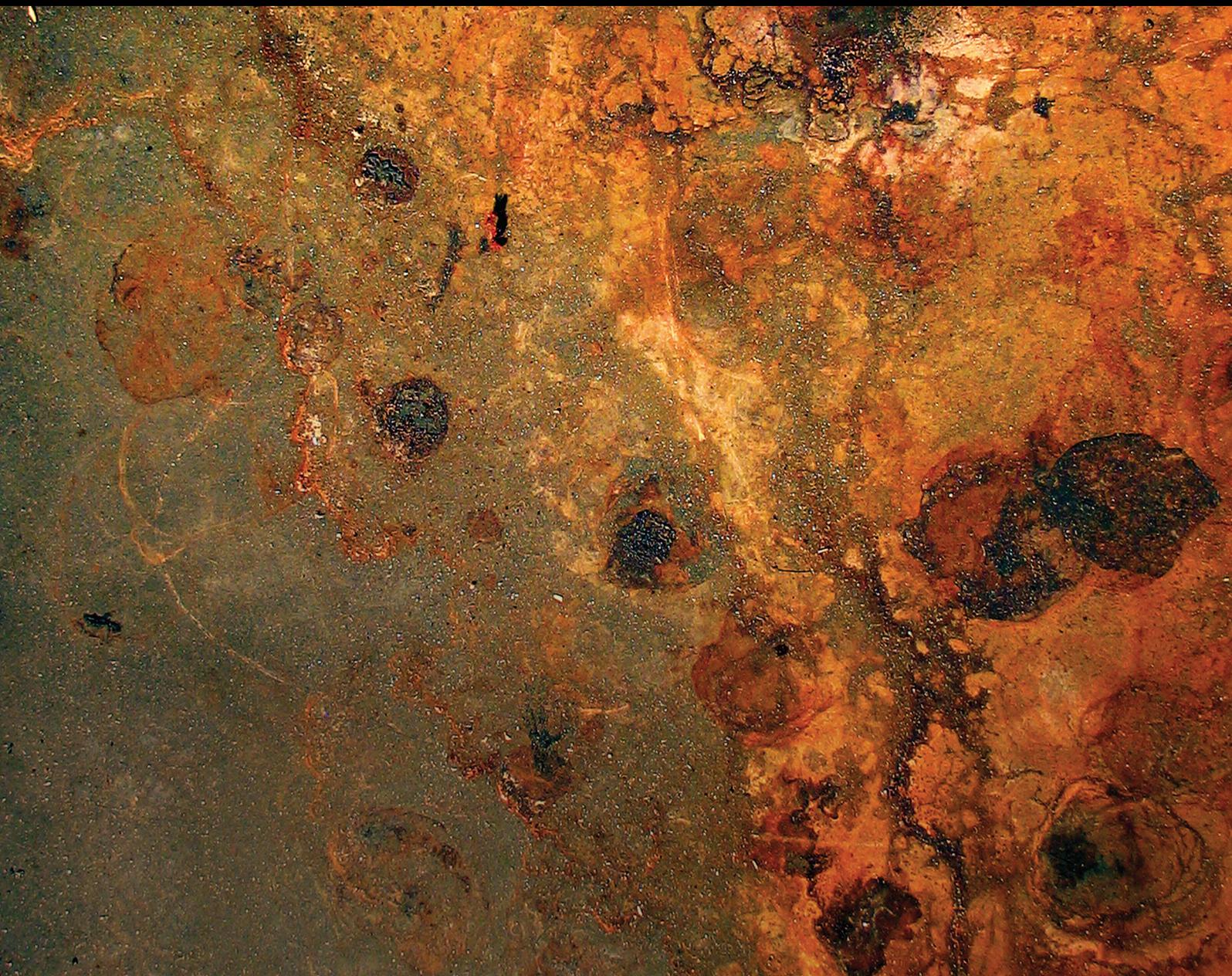


International Journal of Corrosion

Corrosion of Materials after Advanced Surface Processing, Joining, and Welding

Lead Guest Editor: Xizhang Chen

Guest Editors: Arvind Singh, Sergey Konovalov, Juergen R. Hirsch, and Kai Wang





Corrosion of Materials after Advanced Surface Processing, Joining, and Welding

International Journal of Corrosion

Corrosion of Materials after Advanced Surface Processing, Joining, and Welding

Lead Guest Editor: Xizhang Chen

Guest Editors: Arvind Singh, Sergey Konovalov, Juergen R. Hirsch,
and Kai Wang



Copyright © 2018 Hindawi. All rights reserved.

This is a special issue published in “International Journal of Corrosion.” All articles are open access articles distributed under the Creative Commons Attribution License, which permits unrestricted use, distribution, and reproduction in any medium, provided the original work is properly cited.

Editorial Board

Carmen Andrade, Spain

Jose María Bastidas Rull, Spain

Flavio Deflorian, Italy

Dongyang Y. Li, Canada

Vesna Mišković-Stanković, Serbia

Michael I. Ojovan, UK

Francisco Javier Perez Trujillo, Spain

Ramana M. Pidaparti, USA

Willem J. Quadakkers, Germany

Michael J. Schütze, Germany

Raman Singh, Australia

Ramazan Solmaz, Turkey

Jerzy A. Szpunar, Canada

Contents

Corrosion of Materials after Advanced Surface Processing, Joining, and Welding

Xizhang Chen , Arvind Singh , Sergey Konovalov , Juergen R. Hirsch, and Kai Wang 
Editorial (3 pages), Article ID 3569282, Volume 2018 (2018)

Corrosion Behavior of Welded Joint of Q690 with CMT Twin

Peng Liu , Shanguo Han, Yaoyong Yi , and Cuixia Yan 
Research Article (9 pages), Article ID 2368717, Volume 2018 (2018)

Improvement of Corrosion Behavior of Nanostructured Ni Coating by Jet Electrodeposition and Laser Remelting

Hui Fan , Yangpei Zhao, and Shankui Wang
Research Article (5 pages), Article ID 2786429, Volume 2018 (2018)

Effect of Rare-Earth Elements on the Corrosion Resistance of Flux-Cored Arc-Welded Metal with 10CrNi3MoV Steel

Kai Wang , Qinghua Lu, Zexin Jiang, Yaoyong Yi, Jianglong Yi , Ben Niu, Jinjun Ma, and Huiping Hu
Research Article (12 pages), Article ID 4071352, Volume 2018 (2018)

The Analysis of the Influence of Various Factors on the Development of Stress Corrosion Defects in the Main Gas Pipeline Walls in the Conditions of the European Part of the Russian Federation

A.V. Afanasyev, A. A. Mel'nikov, S. V. Konovalov , and M. I. Vaskov
Research Article (10 pages), Article ID 1258379, Volume 2018 (2018)

Pitting Corrosion of the Resistance Welding Joints of Stainless Steel Ventilation Grille Operated in Swimming Pool Environment

Mirosław Szala  and Daniel Łukasik
Research Article (7 pages), Article ID 9408670, Volume 2018 (2018)

Corrosion and Leaching Behaviours of Sn-0.7Cu-0.05Ni Lead-Free Solder in 3.5 wt.% NaCl Solution

Jan-Ervin C. Guerrero, Drexel H. Camacho , Omid Mokhtari, and Hiroshi Nishikawa
Research Article (11 pages), Article ID 6580750, Volume 2018 (2018)

Editorial

Corrosion of Materials after Advanced Surface Processing, Joining, and Welding

Xizhang Chen ¹, Arvind Singh ², Sergey Konovalov ³,
Juergen R. Hirsch⁴ and Kai Wang ⁵

¹College of Mechanical and Electrical Engineering, Wenzhou University, Wenzhou, China

²Department of Mechanical Engineering, Kumaraguru College of Technology (KCT), Tamil Nadu, India

³Department of Metals Technology and Aviation Materials, Samara National Research University, Samara, Russia

⁴Hydro Aluminium Deutschland GmbH, Bonn, Germany

⁵Department of Mechatronics Engineering, Foshan University, Foshan City, China

Correspondence should be addressed to Xizhang Chen; chenxizhang@wzu.edu.cn

Received 15 July 2018; Accepted 17 July 2018; Published 2 September 2018

Copyright © 2018 Xizhang Chen et al. This is an open access article distributed under the Creative Commons Attribution License, which permits unrestricted use, distribution, and reproduction in any medium, provided the original work is properly cited.

Corrosion has been a subject of keen scientific research for the past 150 years. It has a great impact on the safety and reliability in wide range of applications and also on the economy. Corrosion plays a crucial role in determining the life-cycle performance, safety, and cost of engineered products. Further, with the increasing demand for materials with multiple performance capability, advanced surface processing, surface coatings, joining, and welding techniques are being employed. As these materials and methods will be utilized in technologies for high-end applications (e.g., aerospace and nuclear engineering), investigation of corrosion of advanced surfaced materials becomes essential.

Metal joining is a controlled process that is widely employed to fuse similar/dissimilar metals. Among the several metal joining techniques, welding is one of the most widely used for a variety of applications. Metallurgical, physical, and chemical changes caused by welding processes severely affect the corrosion resistance of welds [1, 2]. Some of the recent and advanced welding processes include use of electron beam and laser beam for welding, and they have the advantage of narrow heat affected zone [3]. Even with the use of such advanced welding techniques, materials are still prone to corrosion, invariably due to (i) variation in composition, (ii) accumulation of residual stress, and (iii) modification in microstructure in the weld zone [1]. Similarly, solder joints undergo corrosion depending upon the local environmental conditions. Solder joints are severely prone

to galvanic corrosion as they are comprised of dissimilar metals or alloy components that are in contact with each other. In particular, the phenomenon of electromigration is prevalent in solder joints, wherein corrosion causes build-up of by-product material between the two metal structures of different electrical potentials, resulting in a short-circuit [4].

Another major corrosion phenomenon which is accelerated by the presence of stress is stress corrosion cracking (SCC). In SCC, the imposition of mechanical loads (in particular tensile stress) on the structure causes increased sensitivity to corrosion. The required tensile stress for SCC crack growth may be in the form of directly applied stress (i.e., external stress) or in the form of residual stress (internal) [5]. SCC causes catastrophic failure in weldments. Recently, nanocrystalline (NC) materials (i.e., average grain sizes < 100 nm) are under intense research for their surface properties. In particular, nanocrystalline Ni-coatings are preferred as corrosion resistant coatings for metallic substrates [6]. The small grain size and the high volume fraction of grain boundaries would result in corrosion behavior different from that of polycrystalline materials. However, the effect of nanocrystallinity on the corrosion behavior is reported to vary among metal systems and corrosion environments. This makes it difficult to predict the electrochemical behavior of nanocrystalline coatings from that of their coarse-grained counterparts [7].

While corrosion can act as a single most dominant form of degradation in metallic structures, in real-time applications, it is still a difficult problem to characterize, quantify, and eliminate. With advancement in analytical techniques and superior instrumentation, future research work will provide more efficient solutions to control, monitor, and prevent corrosion.

This special issue encompasses recent research on corrosion of materials after advanced surface processing, joining, and welding. It contains 6 original research articles addressing various aspects related to welding, stress corrosion, soldering, and nanocrystalline coatings used in a wide variety of applications, summarized as follows.

1. Corrosion of Weldments

1.1. Research Article: "Corrosion Behavior of Welded Joint of Q690 with CMT Twin". In this research article, low-alloy steel of Q690 was welded with the method of CMT Twin. Cold metal transfer (CMT) process is a combination of 2 independently functioning arc-welding processes into one single process. Q690 steel is low carbon bainitic steel used in offshore industry. The exposure of the steel to saline environment usually leads to severe corrosion problems. In particular, the presence of Cl^- ion from salts such as NaCl and MgCl_2 in the chloride environment destroys the protective film and increases the severity of corrosion. In this paper the corrosion behaviour of CMT weld joint in 3.5% NaCl solution was reported. Hardness increase due to the appearance of troostite has been observed. While the corrosion products of regions with varying microstructure remained the same, at the welded joints $\text{Fe}(\text{OH})_2$ changed to $\text{Fe}(\text{OH})_3$. Interestingly, the CMT weld zone showed lower corrosion when compared to the overheated zone and the base metal. The better corrosion behaviour at the weld zone was attributed to the presence of nickel. The degree of corrosion with respect to microstructure varied as follows: $\text{HAZ} > \text{BM} > \text{WZ}$.

1.2. Research Article: "Effect of Rare-Earth Elements on the Corrosion Resistance of Flux-Cored Arc-Welded Metal with 10CrNi3MoV Steel". In this research work, the flux-cored arc-welding (FCAW) process was used for welding. It involves the fusion of a flux-cored wire metal with a base metal and is a widely used semiautomatic/automatic process. 10CrNi3MoV steel is a high-strength low-alloy steel (HSLA) widely used in shipbuilding industry. In this work, the composition of the flux-cored wires was modified with varying amount of rare-earth element (cerium rich ferro silicon). The rare-earth element modified wire was used to weld the steel. The microstructural, mechanical, and electrochemical properties of the weldment were reported highlighting the effect of the rare-earth elements on the weld properties. The addition of rare-earth elements up to 0.3 wt.% resulted in refining the second phase particles and acicular ferrite structure of the base metal. Further, charge-transfer channel effect of the second phase particles was reduced by the addition of rare-earth elements. At the optimum composition of 0.3%

rare-earth element addition, both mechanical properties and corrosion resistance of the weldment improved.

1.3. Research Article: "The Analysis of the Influence of Various Factors on the Development of Stress Corrosion Defects in the Main Gas Pipeline Walls in the Conditions of the European Part of the Russian Federation". In this research article, investigation of the stress corrosion cracking of gas pipelines has been reported. The surveyed gas pipeline was made of large diameter rolled steel pipes (mostly produced by Khartsyzsk Pipe Plant, KhPP). In this paper, the influencing factors of stress corrosion defect formation and growth are reported, which were detected during the inspection and overhaul of the main gas pipeline section. Mechanical tests by cyclic loading of samples containing cracks (field testing) showed no crack growth in the absence of corrosive medium. Mechanism of development of SCC crack was proposed. It is reported that there was a consistent pattern between the width of the opening and the length of the crack. The appearance of cracks was found to be influenced by various factors during different stages of life cycle, such as (i) presence of harmful impurities that contaminate the metal pipe and (ii) presence of residual stresses in the pipe wall during manufacturing.

1.4. Research Article: "Pitting Corrosion of the Resistance Welding Joints of Stainless Steel Ventilation Grille Operated in Swimming Pool Environment". The pitting corrosion resistance of a stainless steel ventilation grill welded joint in a swimming pool environment is reported in this article. In swimming pools, in addition to plastics, stainless steel is used for structures/equipment such as ladders, ventilation systems, barriers, and drainage grills. Ventilation grills are usually welded using resistance welding. Corrosion behaviour of the welded joint showed pitting corrosion. The heat affected zone in the weldment showed severity of corrosion when compared to that of the base metal. The poor corrosion resistance of the weldment was attributed to the low quality finish of the weldment, which resulted in unstable weld microstructure that resulted in acceleration of pitting corrosion due to ease of migration of chloride ions.

2. Corrosion of Solders

2.1. Research Article: "Corrosion and Leaching Behaviours of Sn-0.7Cu-0.05Ni Lead-Free Solder in 3.5 wt.% NaCl Solution". In this research article, a new lead-free solder alloy with composition Sn-0.7Cu-0.05Ni was investigated for its corrosion and leaching behaviour in 3.5 wt.% NaCl solution. The highest corrosion rate was observed in the alloy when compared to Sn-Cu and Sn-Ag-Cu alloys, from potentiodynamic polarization measurements. In contrast, 30-day leaching measurements showed reduction in leaching rate in the developed Sn-Cu-Ni alloy solder joint when compared to that of the Sn-Cu and Sn-Ag-Cu joints. This was attributed to the formation of thin passivation film after 15 days. The joint showed higher leaching rate when compared to the alloy due to galvanic corrosion at the surface, which was confirmed by the presence of tin oxides on the surface.

3. Nanocrystalline Ni-Surface Coatings

3.1. *Research Article: "Improvement of Corrosion Behavior of Nanostructured Ni Coating by Jet Electrodeposition and Laser Remelting"*. In this research article, an effective method to improve the corrosion resistance of Ni coating predeposited on 304 stainless steel (1Cr18Ni9) by jet electrodeposition has been reported. The Ni coating was treated by laser remelting so as to improve the coating microstructure and interfacial properties. Corrosion experiments revealed that the as-coated Ni surface had optimal corrosion resistance due to fine grains and dense microstructure when compared to the uncoated substrate. After laser remelting, the corrosion rate decreased significantly owing to the modification in microstructure and enhanced bonding between the coating and substrate. It was identified that the corrosion behaviour of Ni coating on steel substrate can be greatly enhanced by employing laser remelting of the coating.

Xizhang Chen
Arvind Singh
Sergey Kononov
Juergen R. Hirsch
Kai Wang

References

- [1] G. Pimenta and T. A. Jarman, "The corrosion of metal joints, chapter 3-35, corrosion and degradation of engineering materials," in *Shreir's Handbook of Corrosion*, pp. 2447–2462, 3rd edition, 2010.
- [2] A. C. Murariu and N. Pleșu, "Investigations on corrosion behaviour of welded joint in ASTM A355P5 alloy steel pipe," *International Journal of Electrochemical Science*, vol. 10, no. 12, pp. 10832–10846, 2015.
- [3] C. T. Kwok, S. L. Fong, F. T. Cheng, and H. C. Man, "Pitting and galvanic corrosion behavior of laser-welded stainless steels," *Journal of Materials Processing Technology*, vol. 176, no. 1–3, pp. 168–178, 2006.
- [4] T. P. Vianco, "Corrosion Issues in Solder Joint Design and Service," Sandia National Laboratories, Report, 1999.
- [5] R. N. Parkins, *Uhlig's Corrosion Handbook*, chapter 14, John-Wiley & Sons, New Jersey, NJ, USA, 3rd edition, 2011.
- [6] L. Wang, J. Zhang, Y. Gao, Q. Xue, L. Hu, and T. Xu, "Grain size effect in corrosion behavior of electrodeposited nanocrystalline Ni coatings in alkaline solution," *Scripta Materialia*, vol. 55, no. 7, pp. 657–660, 2006.
- [7] R. Rofagha, R. Langer, A. M. El-Sherik, U. Erb, G. Palumbo, and K. T. Aust, "The corrosion behaviour of nanocrystalline nickel," *Scripta Materialia*, vol. 25, no. 12, pp. 2867–2872, 1991.

Research Article

Corrosion Behavior of Welded Joint of Q690 with CMT Twin

Peng Liu ^{1,2}, Shanguo Han,² Yaoyong Yi ², and Cuixia Yan ¹

¹Faculty of Materials Science and Engineering, Kunming University of Science and Technology, 68 Wenchang Road, Kunming, Yunnan 650093, China

²Guangdong Welding Institute (China-Ukraine E. O. Paton Institute of Welding), Guangdong Key Laboratory of Modern Welding Technology, 363 Changxing Road, Guangzhou, Guangdong 510650, China

Correspondence should be addressed to Yaoyong Yi; yiyayong@hotmail.com and Cuixia Yan; cuixiayan09@gmail.com

Received 4 January 2018; Revised 18 March 2018; Accepted 11 April 2018; Published 4 July 2018

Academic Editor: Sergey Kononov

Copyright © 2018 Peng Liu et al. This is an open access article distributed under the Creative Commons Attribution License, which permits unrestricted use, distribution, and reproduction in any medium, provided the original work is properly cited.

Low alloy steel of Q690 was welded with the method of CMT Twin. The corrosion behavior of welded joint had been investigated using scanning vibrating electrode technique (SVET) in 3.5% NaCl solution. The research results showed that the appearance of the troostite increased the hardness of the heat affected zone. Furthermore, the corrosion products of different microstructure were identical, and the white products ($\text{Fe}(\text{OH})_2$) of welded joint turned into products of rufous ($\text{Fe}(\text{OH})_3$). The quantitative information provided by SVET was discussed, and the corrosion degree was measured by some parameters. In comparison with other areas, the corrosion rates of the overheated zone and the base metal were higher. Then, the corrosion resistance of the weld zone with CMT Twin was greatly improved, when compared with that of the base metal. Therefore, Ni has significant influence on corrosion resistance of weld zone. In summary, it can be discovered that the corrosion rates of various zones were related to the welding heat input.

1. Introduction

Q690 steel is known as a typical low carbon bainite steel with excellent mechanical properties, and it is widely used in offshore engineering industry [1, 2]. However, the complex chloride environment tends to be invalidated ahead of lifetime in welded parts, so it is significant to study the corrosion behavior of welded parts [3, 4]. Furthermore, the chloride environment contains more inorganic salts (such as NaCl and MgCl_2) [5], and Cl^- is the most important corrosive ion. Subsequently, Cl^- is able to destroy the protective effect of the corrosion scales, and it significantly increases the activity of the matrix. So Cl^- can accelerate the corrosion rate, and eventually lifetime of the welded joint will be reduced. Owing to the difference of microstructure in the welded joint, the corrosion situation is different. Various traditional corrosion detection methods [6, 7] obtain the corrosion condition of the whole electrode only and cannot get the corrosion behavior of the microregions. On microstructure and grain size of the welded joint, the electrochemical method of microregion has peculiar advantages over the classical electrochemical method.

Scanning vibrating electrode technique (SVET) [8, 9] is to study the corrosion resistance of samples by detecting the local corrosion potential (current) information of samples without touching the surface of the sample. However, welding defects can affect the electric potential of SVET, thus affecting test results [10, 11]. Therefore, SVET has been widely used in the research of various types of corrosion, such as pitting, intergranular corrosion, and stress corrosion [12, 13].

In previous researches the corrosion behavior of welded joint was studied with SVET. Wang et al. studied the corrosion behavior of HAZ in acidic soil solution with SVET [14]. The results demonstrated that microstructure of granular bainite mixed with ferrite was with the highest charge transfer resistance and the most positive current density value. Acicular ferrite of base metal displayed the lowest charge transfer resistance and the most negative current density. Liu et al. studied the corrosion properties of welded joints with different heat input in high strength low alloy steel [15]. Fuertes et al. used SVET to investigate oxide dissolution and initiation and propagation of corrosion on the welded zone [16]. Luo et al. used SVET to study stress corrosion cracking in heat affected zone [17]. The formation and development

TABLE 1: The chemical compositions of the tested steel (Q690) and ER 110S-G (wt%).

| materials | C | Si | Mn | P | S | V | Ti | Cr | Ni | Cu |
|-----------|-------|---------|---------|--------|-------|-------|------|------|---------|---------|
| Q690 | ≤0.18 | ≤0.50 | ≤1.70 | ≤0.025 | ≤0.02 | ≤0.15 | ≤0.2 | ≤0.3 | ≤0.50 | ≤0.30 |
| ER 110S-G | ≤0.1 | 0.4-0.8 | 1.5-1.8 | ≤0.02 | ≤0.02 | — | — | — | 1.3-1.6 | 0.2-0.4 |

of stress corrosion cracking were explained. Ma et al. used SVET to investigate the localized corrosion behaviors of the welded joint [18]. They discovered that there were the maximum microhardness and the densest microstructure in the welded zone compared with the other zones. And the welded zone presented the lowest current density due to the presence of iron oxides and the densest microstructure, thus showing the excellent corrosion resistance. Indeed, the SVET results reveal that the corrosion rates of welded specimens are associated with the welding heat input and corrosion products.

The above studies indicate that the various microstructure of the welded joint is an important parameter of affecting corrosion resistance. Adopting local electrochemical measurement techniques for characterizing the localized corrosion of welded joint can better reveal the corrosion mechanism, and the corrosion behavior of welded joint with different microstructure is clearly evaluated. It is relatively rare to study the corrosion resistance of welded joints with SVET technology in chloride environment. Therefore, it is significant for the research of Q690 in 3.5% NaCl solution.

In this work, a SVET method provided further valuable information on different microstructure of the welded joints and evaluated the corrosion resistance of the welded joint. Combined with the microstructure and hardness analysis, the corrosion behavior of Q690 with CMT Twin in 3.5% NaCl solution was carried out.

2. Experimental

2.1. Materials. The low alloy steel of Q690 was welded with CMT Twin, and the dimension of groove was shown in Figure 1. In this work, the welding wire (type: OK AristoRod 69/ER110S-G, produced by ESAB company) of 1.2 mm in diameter was utilized as the filling material in welding groove. Moreover, a welding machine (type: TransPuls Synergic CMT 5000, produced by Fronius Company) was utilized, and a mixture of 82% Ar + 18% CO₂ was selected. The chemical compositions of the base material Q690 and the wire were shown in Table 1.

2.2. The Test Method

2.2.1. Hardness Analysis. Microhardness test was conducted through a nanoindentation measuring device (type: HVS 1000). The test force was 1 Kgf and the force duration was 10 s. The distance between each point was 0.5 mm. The connection between hardness value and microstructure is very close. The hardness is very important in mechanical properties of the materials.

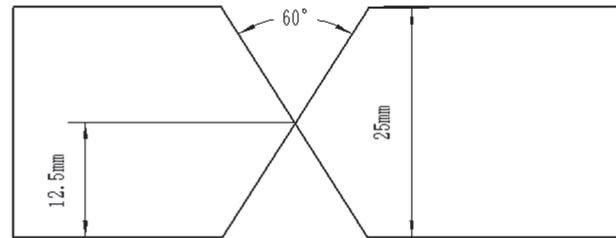


FIGURE 1: Schematic illustration of welded groove.

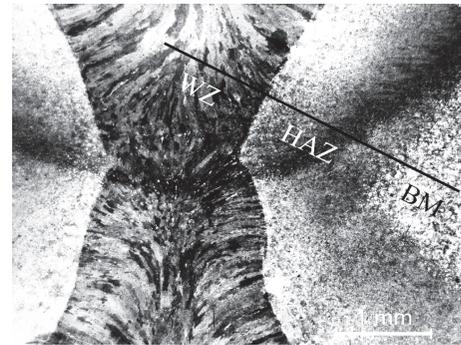


FIGURE 2: Cross section macro-images of the weld joint.

2.2.2. Microstructure Analysis. The micro-images of cross section were shown in Figure 2, which exhibited that joint had good welding quality. Microstructure samples were machined with 10 mm×10 mm×5 mm, which ensured that the specimen contained base metal (BM), heat affected zone (HAZ), and weld zone (WZ). Prior to microstructure testing, the sample was polished sequentially with the number of 120, 240, 400, 600, 800, and 1000 emery papers and then polished to the mirror with 1.5 mm diamond paste. After drying, the specimen was etched by a mixture of 4% nitric acid and ethanol (weight fraction). The sample was dried with air compressor; microstructure of the sample was observed with metalloscope.

2.2.3. Corrosion Behavior Analysis. All sides of the specimen were embedded in an epoxy resin except the exposure surface, and the working area was 14 mm×14 mm. Polish the face of the specimen, clean the surface with anhydrous ethanol, and dry it with air compressor. Subsequently, the SVET measurements were conducted through a PAR370 Scanning Electrochemical Workstation. The SVET test was adopted by the Versa SCAN electrochemical scanning system, and the scanning microprobe was a Pt-Ir microelectrode with a

diameter of 50 μm . At the beginning of the test, the sample was placed in the electrolytic cell, and the surface of the sample remained horizontal.

The scanning probe vibrated in the perpendicular direction at the surface of the sample, and the distance between the probe and sample surface was 100 μm . The vibrating amplitude of the microelectrode was 30 μm and the vibrating frequency was 50 Hz in the direction to the surface. The scanning area was 5 mm \times 3 mm, and it scanned from weld zone to base metal.

SVET measurements were carried out in electrochemical corrosion testing apparatus at room temperature in 3.5wt% NaCl solution [19–21]. And the probe was immersed into 3.5 wt% NaCl aqueous solution. The results of SVET were the ion potential difference of local oxidation-reduction reaction on the specimen surface, and the data were converted to local current density according to the specification of data processing in instrument.

The SVET current density maps and the statistical analysis of the data were performed with Origin software. The current densities were displayed in three-dimensional (3D) maps, showing the spatial distribution of the current density as a function of the (x,y) position in the scan region. The current values in the SVET map are positive for anodic currents and negative for cathodic currents. The contour map of the current densities is at the bottom of the 3D maps.

The integrated anodic current (I_{int}) was used to characterize the corrosion resistance of different microstructure. I_{int} was evaluated by integration of the overall anodic current (i_A) on SVET current density map. The whole scan area was split into 21 \times 21 small squares, and we calculated the scan area (S) and number (n) of measurement points in each microstructure. The scan area of WZ, overheated zone (OZ), normalized zone (NZ), incomplete normalized zone (INZ), and BM, respectively, was 4.9, 2.2, 2.5, 0.4, and 5.0 mm², and n of WZ, OZ, NZ, INZ, and BM, respectively, was 142, 56, 74, 20, and 149. We calculated the anodic current on each microstructure, and calculation formula is shown by

$$I_{\text{int}} = \frac{S \sum i_A}{n} \quad (1)$$

(see [22]) where i_A is the anodic current density ($i_A > 0$) measurement points in each microstructure.

3. Result and Discussion

3.1. The Hardness of the CMT Twin Welded Joint. The distribution of hardness in welded joint is shown in Figure 3. It can be shown that the hardness values of the welded joint are symmetric distribution as a centre of the welded zone. It can be concluded that the welded joint shows relatively uniform fluctuations of hardness in BM, and the value is maintained at about 275 HV. In the vicinity of the heat affected zone, the hardness of BM decreases to a certain extent, which is due to the growth of grain on the edge of the HAZ.

The hardness of the HAZ in Figure 3 rises relatively fast, where the troostite has a high hardness (about 310 ~ 332 HV). Simultaneously, the decrease of troostite near the WZ leads to

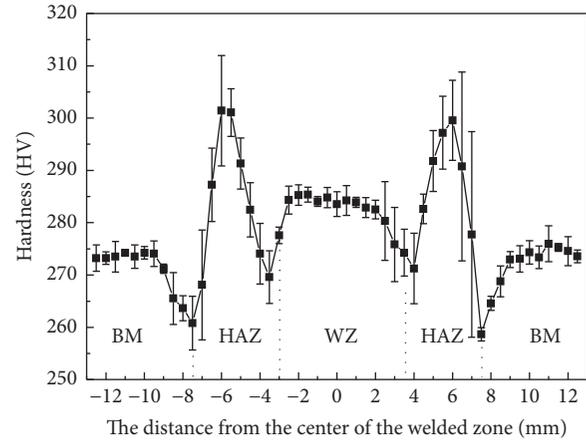


FIGURE 3: The distribution of the hardness in the welded joint.

further decrease of the hardness on the edge of the HAZ. And the amplitude of descent in hardness is little lower than that of the BM, as presented in Figure 3. It can be shown in Figure 3 that the welded joint shows obvious hardness fluctuation in HAZ, which reveals the inhomogeneous microstructure of HAZ. This leads to heavy corrosion for HAZ in 3.5% NaCl solution. However, the hardness of the HAZ is determined by the tendency of brittleness in the BM and the cooling speed of the HAZ. This means that the brittleness and hardness of the BM are determined by the chemical composition, while the cooling rate of the HAZ is mainly affected by the welding specification. Generally, the chemical composition of the BM is certain, and the hardness of the HAZ can only be improved by changing the cooling rate after welding. It can be confirmed that the microstructure of the WZ consists of the bainite and a small amount of acicular ferrite, and the hardness is kept at 285 HV, slightly higher than that of the BM.

3.2. Microstructure of the Welded Joint. It can be shown in Figure 4(a) that the microstructure of BM consists of a mixture of ferrite with low carbon slabs and carbide. Meanwhile, the same size of the bainite is parallel with arrangement in direction, which formed the bainite-rich region. The microstructure of lower bainite (LB) is mostly featured with the lath ferrite (F), and from the austenite grain boundary to the intragranular one the parallel growth of ferrite is shown. Simultaneously, the short rod-like black product with intermittent is cementite, which exists in lath ferrite. Moreover, it can be shown in Figure 4 that the welded joint shows obvious crystal boundary of austenite in BM, and the distribution of ferrite is very homogeneous. Specifically, the grain orientation in the region is larger, and plenty of bainite regions are formed.

Figure 4(b) shows optical micrographs of the cross section of the different welding regions (incomplete normalized zone (INZ) and NZ) of the welded joint. It can be shown that the troostite (black substance) is precipitated out of the coarse bainite in HAZ, and it gradually diffuses into the BM. It obviously detects the diffusion process of the troostite in

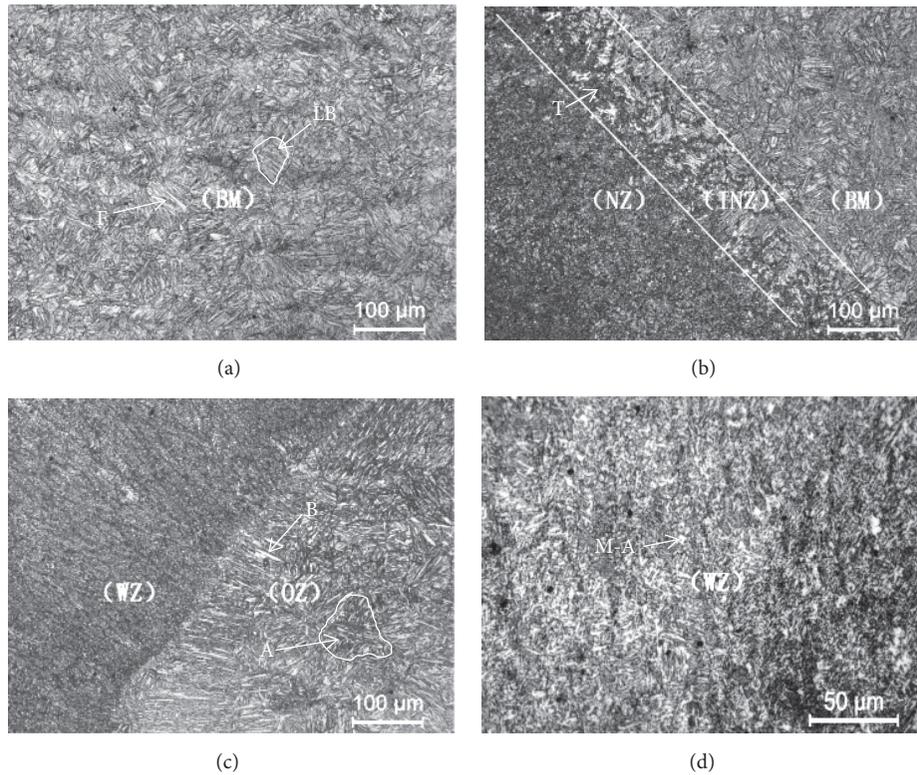


FIGURE 4: The microstructure of BM, INZ, NZ, OZ, and WZ.

INZ, while NZ is completely covered by the troostite (T). This means that this zone has high mechanical properties (hardness and strength).

Figure 4(c) shows the microstructure of OZ, in which the upper left corner is WZ. It can be seen that the microstructure adjacent to WZ is relatively coarse and the grain boundary is clear. Moreover, the microstructure adjacent to the fusion line shows that the microstructure of the welded zone is relatively finer compared with the BM, and there also exists black granular troostite in the grain boundary of austenite (A). In the area of BM adjacent to WZ, it can be clearly shown that the microstructure of the BM is basically perpendicular to the fusion line, and bainite (B) becomes longer. In HAZ, the grain boundary of austenite is obvious, and the microstructure of HAZ is obviously more coarse than that of BM, as presented in Figure 4. Owing to the lower heat input and high speed of cooling after welding, massive bainite with a high density dislocation is formed with dispersive distribution of carbide. The appearance of bainite presents a thin strip and a series of slabs are arranged in parallel. As a result, the same direction bainite grows to form a regional strip, and the slabs of the bainite intersect each other.

Figure 4(d) presents the microstructure of WZ; it can be shown in Figure 4(c) that the microstructure is finer. After magnification, the granular bainite (M-A constituent) is distributed homogeneously. It is well known that the cooling rate greatly affected the formation of granular bainite. The cooling rate influences the growth of factors such as the generation of a significantly quenched hardening structure. Moreover,

the low cooling rate increases the austenitic isothermal time, which is favorable for the short-range diffusion of carbon atoms. The quantity of the carbon concentrated in the primary austenite will be suppressed, being affected by the welding heat input, when the bainite ferrite is generated during the bainite transformation. The bainite ferrite formation is prevented by the primary austenite, while the carbon concentration reached a critical value. Therefore, the residual austenite transforms into the M-A island that is distributed within the ferrite matrix. Subsequently, the lath and granular bainite microstructures are generated. Therefore, a large number of small M-A islands are distributed evenly in ferrite matrix. In the process of granular bainite formation, ferrite with precipitating out of austenite firstly is featured with the shape of lath. Meanwhile, lath ferrite with high dislocation density leads to high strength of materials. Owing to the hard phase of M-A islands, the M-A islands are precipitated by way of small and dispersed precipitation. Indeed, the interaction between M-A islands and the dislocation hinders the dislocation movement. In other words, the way of dispersion strengthening improves the strength of the steel.

3.3. Corrosion Behavior of the CMT Twin Welded Joint. The corrosion of low carbon alloy steel in 3.5% NaCl solution is typical electrochemical corrosion. When low carbon alloy steel is immersed in 3.5% NaCl solution, the distribution of components, phase, and the surface stress of surface in material are not uniform. Indeed, the distribution of electrode potential between material surface and interface

of water is inhomogeneous on the microscale. There are countless corrosion microcells on the surface of the metal, resulting in the corresponding anode and cathode areas. The anode is an active dissolving reaction, namely, $\text{Fe}-2\text{e}=\text{Fe}^{2+}$. In the meantime, the corrosive particles in the environment are mainly O_2 and Cl^- , in which the concentration of oxygen is consistent, and the cathode is the depolarization reaction of oxygen, namely, $\text{O}_2+2\text{H}_2\text{O}+4\text{e}=4\text{OH}^-$. Therefore, the corrosion rate of the materials may be accelerated by influencing the adsorption behavior of the corrosive Cl^- . Furthermore, Cl^- is a characteristic adsorption ion, which is able to form a chemical bond of coordination with metal and adsorb on the surface of the metal. This effect usually causes the change of charge on the metal surface.

3.4. SVET Current Density Maps. The SVET current density maps for various periods in 3.5% NaCl solution are demonstrated in Figure 5. Simultaneously, the boundary lines of different microstructure were displayed in X axis. The anodic current appeared at different sites, and the anodic area is mainly located at the BM in 0 hour (Figure 5(a)). The 0 hour is the time for SVET to scan the once.

At the beginning of time (0 h), the corrosion resistance of the BM and HAZ is worse. In addition, due to the influence of the heat input during the process of welding, there is obvious differentiation of microstructure between BM and WZ. There is obvious potential difference between the WZ and BM, resulting in galvanic corrosion. Following this, the cathode region appears in the WZ and thus is protected. In the meantime, the microstructure in the HAZ is relatively coarse. As a result, the corrosion resistance of the WZ is better than BM. The microstructure of WZ consists of the granular bainite (M-A constituent), as presented in Figure 4. Granular bainite consists of a mixture of ferrite and austenite, and ferrite is surrounded by austenite. In addition, phase transition temperature of bainite is low, and the diffusion ability of alloy elements is relatively worse. Therefore, the uniform bainite reduces the potential difference between the anode and cathode. Thus, it is indicated that the corrosion rate reduces to some extent, especially the tendency of localized corrosion. In addition, grain boundary of bainite is small angle grain boundary, and interfacial energy can be lower, and the impurity content of grain boundary is low, making it shows excellent corrosion resistance.

It has been established that, with the increase of time (2 h), the SVET current density in anode region and cathode region decreases. In the initial period of corrosion, the unstable product $\text{Fe}(\text{OH})_2$ is formed on the surface of the sample, which to some extent inhibits the process of anodic dissolution of the corrosion reaction, thus reducing the corrosion rate [23]. The anodic current density peak appears in BM, and the area of higher anode current significantly reduces. In the meantime, the cathodic area appears in the HAZ, and the number significantly increases. When time is 4 h, the anodic current density peak appears in WZ. In other words, the anode area is moved from BM to the WZ. Owing to the porous structure of the new rust

layer, the rust layer cannot provide adequate protection, so the rust layer on the sample surface is continuously increasing, as shown in Figures 5(b)–5(d). When the corrosion time is 6 h, the peak current area and quantity of the anode decrease gradually. Thus, it means that the corrosion rate of the whole regional greatly reduces, and there are only scattered anode current peaks at the edge of the weld zone. The cathode region appears in HAZ and the BM, which improves the corrosion resistance of the two regions.

3.5. Current Peak of Anodic and Cathodic. It is possible to go further and attempt to extract more information from the SVET results. As shown in Figure 6, it can be observed that the welded joint exhibits the current peak of anodic ($i_{A,\text{max}}$), cathodic ($i_{C,\text{max}}$), and the average current density (i_{Ave}) in SVET maps. It can be seen from the graph that the peak of cathode current and anode current are decreasing gradually, while the average current is moving around zero. The test of corrosion was conducted without external polarization, so the anodic currents and cathodic currents are balanced and the net current should be zero. In general, the current peak of cathode and anode should be equal in value, and the average current density should be zero. However, the difference between the anode and cathode current peaks in SVET maps results in an average current deviation of zero. The reason for this deviation may be that the current density of the SVET maps is not measured at the same time. In the process of scanning, corrosion behavior and current distribution are constantly changing. As shown in Figures 5(a)–5(d), the current density of different microstructure varies considerably with the increase of corrosion time. This shows that the process of electrochemical is instantaneous, which changes at any time.

3.6. Corrosion Behavior of Different Zone. Integrated anodic current of different microstructure is as shown in Figure 7. It shows that the integrated anodic current (I_{Int}) of OZ and BM is larger than that of WZ in the whole corrosion process. Combined with SVET maps, the corrosion tendency of microstructure in WZ is relatively high and the corrosion rate is low. At the same time, the degree of corrosion in WZ is lower than that of BM. As the iron dissolves, the integrated anodic current in BM and OZ decreases gradually. Moreover, the corrosion products decrease the corrosion rate of WZ and BM. Due to the coarse microstructure in HAZ, the integrated anodic current increases (0–2 h). With the oxidation of $\text{Fe}(\text{OH})_2$, the integrated anodic current of BM and OZ increases slightly (2–4 h). As the size of microstructure varies, I_{Int} in the BM decreases, while I_{Int} in OZ is relatively stable (4–6 h). Generally, the size of the integrated anodic current reflects the corrosion rate of different regions. With the formation of corrosion products, the corrosion rate of NZ gradually decreases (2–6 h). The weld zone is protected by the cathode and the degree of corrosion is little. Compared with the NZ, the corrosion resistance of the INZ is enhanced, which is due to the decrease of the amount of the troostite.

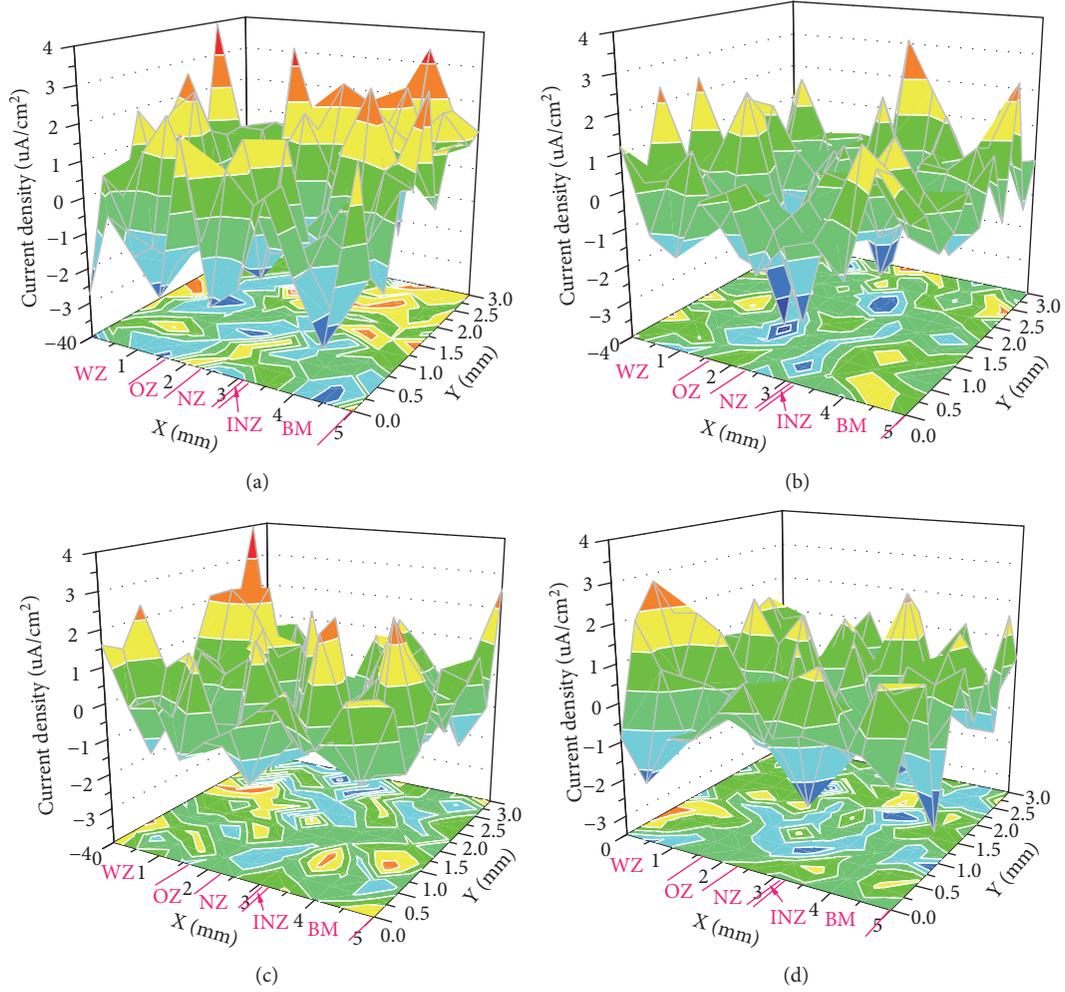


FIGURE 5: SVET current density maps of (a) 0 h, (b) 2 h, (c) 4 h, and (d) 6 h.

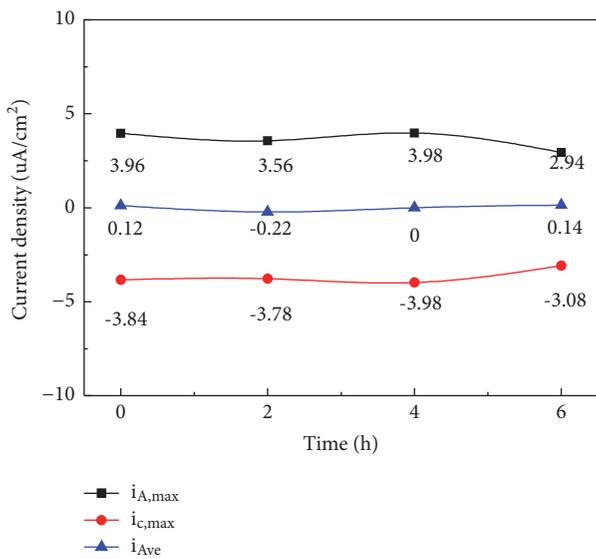


FIGURE 6: The current peak of anodic ($i_{A,max}$), cathodic ($i_{C,max}$), and the average current density (i_{Ave}) in SVET maps.

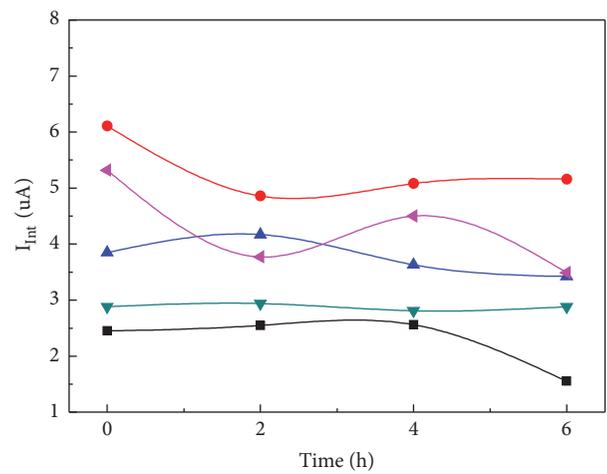


FIGURE 7: Integrated cathodic current (I_{Int}) of different microstructure.

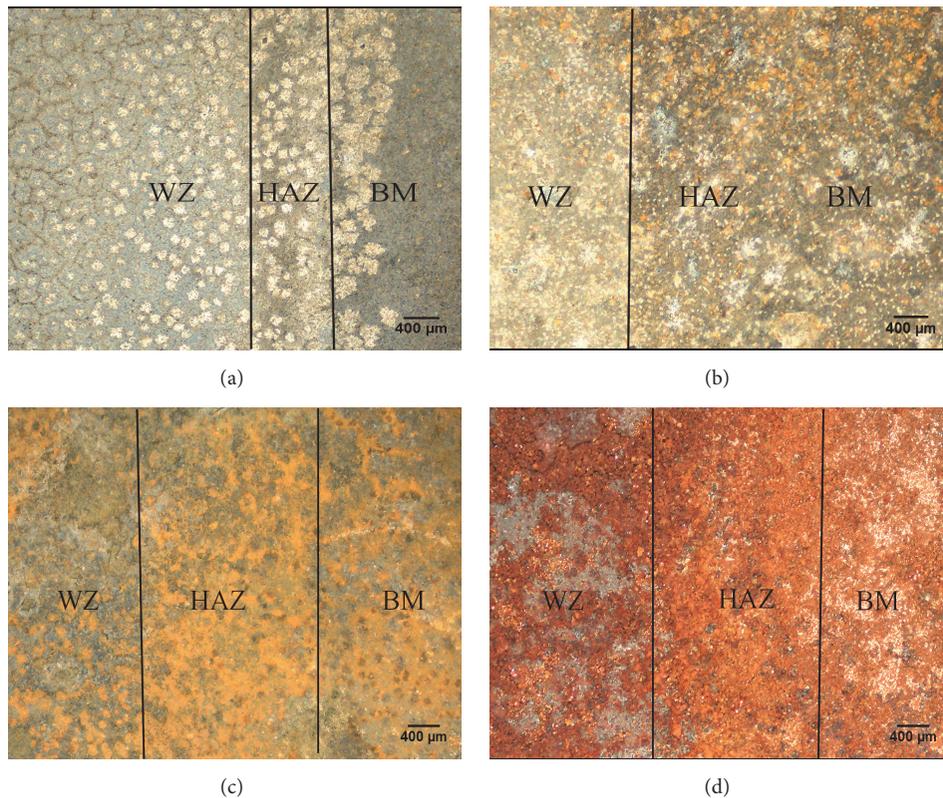


FIGURE 8: The macroscopic appearance of different corrosion time.

3.7. Macro Analysis of Welded Joint after Corrosion. The macroscopic appearance of different corrosion times in welded joint is demonstrated in Figure 8. Figure 8(a) reveals that different degrees of corrosion occurred in the BM, WZ, and HAZ. That is to say, the results are in agreement with the distribution of current density maps (Figure 5(a)). The white corrosion products, including $\text{Fe}(\text{OH})_2$, are mainly distributed in the HAZ and the zone adjacent to the HAZ (BM and WZ). In the WZ, the white corrosion products, which are away from the area of HAZ, gradually decrease. Moreover, on the right of Figure 8(a), the coarse microstructure of HAZ leads to lesser corrosion product.

When corrosion time is 2 h, white corrosion products disappeared, and a few corrosion products ($\text{Fe}(\text{OH})_2$) with rufous appear. Furthermore, it is apparent that the boundary of the HAZ and the BM basically disappeared. That is to say, the corrosion products of the BM and the HAZ are obviously more than the WZ. It is revealed that $\text{Fe}(\text{OH})_2$ is easily oxidized to products of gray-green. The products of rufous are mainly concentrated in the HAZ, and the BM has fewer corrosion products and the least ones in WZ, as presented in Figure 8(c). When corrosion time is 6 h, there are obvious differences in WZ, HAZ, and BM. Figure 8(d) shows the corrosion degree of WZ is the minimum, and the corrosion resistance is excellent. Furthermore, the corrosion products in BM have not been completely oxidized, and some corrosion products of white ($\text{Fe}(\text{OH})_2$) exist.

As Figure 8 shows, the corrosion degree of each region is not uniform at any time. The grains of granular bainite in

WZ are finer and evenly distributed, and the distribution of microstructure is uniform. It is well known that the content of granular bainite is high in Q690. In addition, the small cathode and large anode lead to reducing the corrosion rate of WZ in the process of corrosion. As shown in Figure 8, the WZ displays the excellent corrosion resistance. On the contrary, the HAZ with coarse microstructure exhibits the worst corrosion resistance. It may also be that nickel increases the corrosion resistance of the weld area. As shown in Table 1, there are more nickel elements in the weld zone, in comparison with BM. The study shows that the addition of nickel can form a protective rust layer on the surface, thus improving the corrosion resistance of the welded zone [24]. Ni has ability to resist the corrosive action of Cl^- ions. Accordingly, Ni exhibits high corrosion resistance in 3.5% NaCl solution. This indicates that, as a result of Ni in the welded zone, the aggressive action of Cl^- ions on the surface is suppressed. This behavior exhibits very important result that the Ni has influence on corrosion resistance in 3.5% NaCl solution.

In summary, it can be discovered that the corrosion rates of various zone are associated with the welding heat input. From this perspective, the corrosion degree of microstructure is mainly $\text{HAZ} > \text{BM} > \text{WZ}$.

4. Conclusions

The microstructure, hardness, and corrosion behavior in welded joint of Q690, which was welded with CMT Twin,

were studied. The experimental findings support the following major conclusions:

(1) The hardness of the base metal was the minimum, while the hardness of weld zone with tiny microstructure was higher than that of the base metal. Owing to the coarse microstructure, the hardness of overheated zone decreased. The hardness of normalized zone increased with the appearance of the troostite.

(2) As the corrosion time increases, the corrosion products of different microstructure were identical, and the white products of the welded joint were turned into products of rufous. In the role of oxygen, $\text{Fe}(\text{OH})_2$ was oxidized to $\text{Fe}(\text{OH})_3$. Also, the overheated zone and the base metal presented a high corrosion rate. The degree of corrosion in weld zone, which is protected by the cathode, was mild. The corrosion resistance of the weld zone with CMT Twin was greatly improved compared with that of the base metal. This was related to the existence of nickel.

Data Availability

The data used to support the findings of this study are available from the corresponding author upon request.

Conflicts of Interest

The authors declare that there are no conflicts of interest regarding the publication of this paper.

Acknowledgments

This research was finished with the fund of Science and Technology Project of Guangdong Province (2017A010106007, 2017A010102008, and 201101C0104901263) and Science and Technology Project of Guangzhou (201508030023). The authors are grateful to Guangdong Welding Institute (China-Ukraine E. O. Paton Institute of Welding).

References

- [1] Z. S. Li, S. L. Li, X. H. Zhang, and J. Z. Liu, "Interaction study of carbide precipitation and impurity segregation under temper embrittlement conditions in a coarse-grained heat-affected zone in Q690 steel," *Advanced Materials Research*, vol. 1015, pp. 189–193, 2014.
- [2] X. Chen and Y. Huang, "Hot deformation behavior of HSLA steel Q690 and phase transformation during compression," *Journal of Alloys and Compounds*, vol. 619, pp. 564–571, 2015.
- [3] H. Wan, C. Du, Z. Liu, D. Song, and X. Li, "The effect of hydrogen on stress corrosion behavior of X65 steel welded joint in simulated deep sea environment," *Ocean Engineering*, vol. 114, pp. 216–223, 2016.
- [4] R. Pérez-Mora, T. Palin-Luc, C. Bathias, and P. C. Paris, "Very high cycle fatigue of a high strength steel under sea water corrosion: A strong corrosion and mechanical damage coupling," *International Journal of Fatigue*, vol. 74, pp. 156–165, 2015.
- [5] Y. Ye, C. Wang, H. Chen, Y. Wang, J. Li, and F. Ma, "An analysis of the tribological mechanism of GLC film in artificial seawater," *RSC Advances*, vol. 6, no. 39, pp. 32922–32931, 2016.
- [6] F. Gan, G. Tian, Z. Wan, J. Liao, and W. Li, "Investigation of pitting corrosion monitoring using field signature method," *Measurement*, vol. 82, pp. 46–54, 2016.
- [7] V. Verdingovas, M. S. Jellesen, and R. Ambat, "Colorimetric visualization of tin corrosion: A method for early stage corrosion detection on printed circuit boards," *Microelectronics Reliability*, vol. 73, pp. 158–166, 2017.
- [8] D. Mata, M. Serdechnova, M. Mohedano et al., "Hierarchically organized Li-Al-LDH nano-flakes: A low-temperature approach to seal porous anodic oxide on aluminum alloys," *RSC Advances*, vol. 7, no. 56, pp. 35357–35367, 2017.
- [9] A. C. Bastos, M. C. Quevedo, O. V. Karavai, and M. G. Ferreira, "Review—on the application of the scanning vibrating electrode technique (svet) to corrosion research," *Journal of The Electrochemical Society*, vol. 164, no. 14, pp. C973–C990, 2017.
- [10] V. I. Danilov, L. B. Zuev, S. V. Konovalov et al., "On the effect of electric potential on resistance of metals surface to microindentation," *Journal of Surface Investigation X-ray Synchrotron and Neutron Techniques*, vol. 1, pp. 157–161, 2010.
- [11] S. A. Nevskii, S. V. Konovalov, and V. E. Gromov, "Effect of the electric potential of the aluminum surface on stress relaxation," *Technical Physics*, vol. 56, no. 6, pp. 877–880, 2011.
- [12] M. G. Taryba and S. V. Lamaka, "Plasticizer-free solid-contact pH-selective microelectrode for visualization of local corrosion," *Journal of Electroanalytical Chemistry*, vol. 725, pp. 32–38, 2014.
- [13] A. S. Gnedenkov, S. L. Sinebryukhov, D. V. Mashtalyar, and S. V. Gnedenkov, "Localized corrosion of the Mg alloys with inhibitor-containing coatings: SVET and SIET studies," *Corrosion Science*, vol. 102, pp. 269–278, 2016.
- [14] L. W. Wang, Z. Y. Liu, Z. Y. Cui, C. W. Du, X. H. Wang, and X. G. Li, "In situ corrosion characterization of simulated weld heat affected zone on api x80 pipeline steel," *Corrosion Science*, vol. 85, pp. 401–410, 2014.
- [15] W. Liu, H. Pan, L. Li et al., "Corrosion behavior of the high strength low alloy steel joined by vertical electro-gas welding and submerged arc welding methods," *Journal of Manufacturing Processes*, vol. 25, pp. 418–425, 2017.
- [16] N. Fuertes, V. Bengtsson, R. Pettersson, and M. Rohwerder, "Use of SVET to evaluate corrosion resistance of heat tinted stainless steel welds and effect of post-weld cleaning," *Materials and Corrosion*, vol. 68, no. 1, pp. 7–19, 2017.
- [17] L. Luo, Y. Huang, and F.-Z. Xuan, "Deflection behaviour of corrosion crack growth in the heat affected zone of CrNiMoV steel welded joint," *Corrosion Science*, vol. 121, pp. 11–21, 2017.
- [18] H. Ma, Y. Gu, H. Gao, X. Jiao, J. Che, and Q. Zeng, "Microstructure, chemical composition and local corrosion behavior of a friction stud welding joint," *Journal of Materials Engineering & Performance*, vol. 2, pp. 666–676, 2018.
- [19] B. Yan, H. Chen, and D. Kong, "Effects of laser remelting on salt spray corrosion behaviors of arc-sprayed Al coatings in 3.5% NaCl sea environment," *Transactions of the Indian Institute of Metals*, vol. 6, pp. 1–9, 2017.
- [20] S. Weng, Y. Huang, F. Xuan, and F. Yang, "Pit evolution around the fusion line of a NiCrMoV steel welded joint caused by galvanic and stress-assisted coupling corrosion," *RSC Advances*, vol. 8, no. 7, pp. 3399–3409, 2018.
- [21] H. S. Gadow, M. M. Motawea, and H. M. Elabbasy, "Investigation of myrrh extract as a new corrosion inhibitor for α -brass in 3.5% NaCl solution polluted by 16 ppm sulfide," *RSC Advances*, vol. 7, no. 47, pp. 29883–29898, 2017.

- [22] M. Yan, V. J. Gelling, B. R. Hinderliter, D. Battocchi, D. E. Tallman, and G. P. Bierwagen, "SVET method for characterizing anti-corrosion performance of metal-rich coatings," *Corrosion Science*, vol. 52, no. 8, pp. 2636–2642, 2010.
- [23] Y. Ma, Y. Li, and F. Wang, "The effect of β -FeOOH on the corrosion behavior of low carbon steel exposed in tropic marine environment," *Materials Chemistry and Physics*, vol. 112, no. 3, pp. 844–852, 2008.
- [24] H. M. Abd El-lateef, A. El-Sayed, and H. S. Mohran, "Role of Ni content in improvement of corrosion resistance of Zn–Ni alloy in 3.5% NaCl solution. Part I: Polarization and impedance studies," *Transactions of Nonferrous Metals Society of China*, vol. 25, no. 8, pp. 2807–2816, 2015.

Research Article

Improvement of Corrosion Behavior of Nanostructured Ni Coating by Jet Electrodeposition and Laser Remelting

Hui Fan ¹, Yangpei Zhao,² and Shankui Wang¹

¹Kewen College, School of Mechanical and Electrical Engineering, Jiangsu Normal University, Xuzhou 221116, China

²School of Mechanical and Electrical Engineering, Jiangsu Jiangzhu Institute, Xuzhou 221116, China

Correspondence should be addressed to Hui Fan; xzfanhui@163.com

Received 6 February 2018; Revised 4 April 2018; Accepted 16 April 2018; Published 2 July 2018

Academic Editor: Xizhang Chen

Copyright © 2018 Hui Fan et al. This is an open access article distributed under the Creative Commons Attribution License, which permits unrestricted use, distribution, and reproduction in any medium, provided the original work is properly cited.

An effective method to improve corrosion resistance for the nickel coating on the stainless steel(1Cr18Ni9) is described. The nickel coating was predeposited on the 1Cr18Ni9 by using the jet electrodeposition technology. Then the laser remelting was conducted on the predeposited Ni coating in order to strengthen the coating's microstructure and the interface between the substrate and the Ni coating. The experimental results revealed that, at current density of 40 A/dm², the deposited coating had the optimal corrosion resistance because of refined grains and dense interior-structure. After laser remelting, the bonding state between the coating and substrate evolved to a new metallurgical combination from originally mechanical combination. The corrosion rate comparison indicated that Ni coating with compound process of jet electrodeposition and laser remelting had higher corrosion resistance compared with bare 1Cr18Ni9 as well as jet electrodeposited Ni coating.

1. Introduction

Nanocoating technology has attracted wide attention in the surface engineering. As it is able to improve target material service performance including corrosion resistant by offering new mechanical and physical properties. Among nanocoating preparing methods, jet electrodeposition (JE) technology has special advantages and has been used for local coating reaction. Because electrolyte is impinged from the jet nozzle onto a cathode surface, high rate of mass transport is available to promote liquid-mass-transfer velocity of electrolyte. In comparison with other conventional electrodeposition manners, jet electrodeposition has two advantages. First, it allows increasing deposition rate as high as tens or even hundreds of times since a much higher current density can be used. Second, it provides nano-scaled refining grains of the deposited material because high current density in use greatly accelerates the nucleation rate and decreases the grain size as a result [1–7].

Laser remelting is another important technique to manufacturing high performance coating. By high-temperature melting the prefabricated coating material on a surface, high anticorrosion property or other well performance deposits

can be formed over material surface [8]. Therefore, given the above experimental facts, combining laser remelting with jet electrodeposition, it is likely to be achieved that coating material structure may be strengthened after laser scanning and the deposit qualities, especially the corrosion behavior, are also likely to be improved [9, 10].

This study is proposed to provide a simple way of improving 304 stainless steel corrosion behavior. It first uses JE to prefabricate a nanostructured Ni coating on the substrate and then makes use of laser radiation to process the coated substrate to provide a dense crystalline Ni coating, which is closely combined with the substrate material. Their characteristic properties were evaluated by scanning electron microscope (SEM) for the crystal structures characterization and by hydrochloric acid corrosion test for the corrosion behavior determination.

2. Experimental Procedure

A self-developed jet electrodeposition setup (see Figure 1) was used to prepare the coating material. The setup is mainly composed of the computer control system, framework,

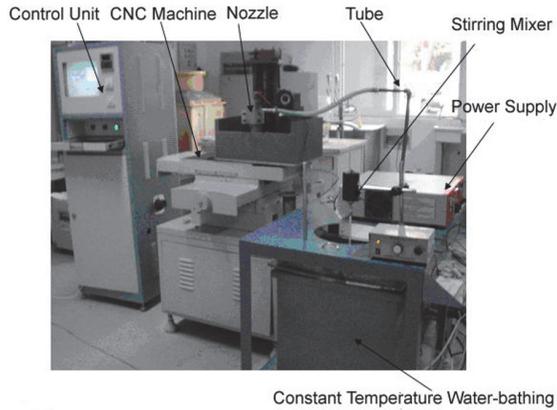


FIGURE 1: Experimental setup for nickel jet electrodeposition.

electrolyte circulatory system, nozzle and its hoisting mechanism, DC power, and other parts.

304 stainless steel (1Cr18Ni9) was chosen as substrate material, with specimen size 100mm×20mm×2mm. Pre-treatment process for the specimens was needed before experiment as follows. First, the specimens were grinded and polished, consequently using 400, 800, and 1000 mesh metallographic sandpapers. Afterwards, polished samples were cleaned by using distilled water as well as acetone soaking for degreasing treatment, for about 5 minutes. The electrolytes compositions are as follows: nickel sulphate 250 g/L, nickel chloride 60g/L, and boric acid 40g/L, the buffer reagent which maintains the pH value in electrolytic solution. At the predeposition procedure, the Ni coating was scan-deposited on the surface of specimen using JE, with the rectangular nozzle (size 20 mm×1 mm) and electrolyte velocity (170L/h, 2.5 m/s). The scan-deposit for each specimen underwent 600 layers, at the scan rate 10 mm/s. Prior to the JE deposition, a thin nickel layer with a thickness of 150 nm was preelectroplated over the substrate surface in a standard sulphate watt bath for use as an interlayer, in order to enhance the adhesion between substrate and nickel coating. During the electrodeposition, a group of direct current was being applied at current density of 30, 40, 50, and 60A/dm², respectively.

Afterwards, laser remelting process was conducted using a SLCF-X12 25 type of CO₂ laser. Remelting process parameters were as follows: laser power 1500 W, 2 mm spot diameter, scanning rate 850 mm/min, and overlapping amount 20%. Prior to the laser scanning, coating surface is painted black in order to increase laser absorption rate. Ar gas protection was used during laser scanning.

The corrosion resistance was determined through a mass loss mensuration, with each value being derived from average of three specimens. The corrosion test was performed in a large tank containing 5 L of 10%HCl aqueous solution as corrodent with room temperature (25°C) and not stirred or aerated. After each specimen was degreased and cleaned, they were all set suspended in the corrosive solution to achieve full corrosion. The coated samples were cut into small specimens with dimensions of 20mm×10mm×2mm. The corrosion rate

curve was plotted as function of the ratio of mass loss to the corrosive area and time. The mass loss was examined by a precision electronic balance with an accuracy of 10⁻⁴g.

3. Results and Discussion

The morphology of electrodeposited nickel coatings (Figures 2(a)–2(d)) displays Ni microstructures at nanometer scale under different current densities. The deposit coating appears mainly compact but still contains some macroscopical pores and defects. An uneven surface and rough grain size (see Figure 2(a)) were observed under relatively low current density of 20 A/dm². As current density increased, the deposit surface became more and more smooth till the current density reached 40 A/dm² (see Figure 2(c)). Afterwards, the overall deposit layer underwent a cellular-like growth and grew into a larger grain size and deteriorative surface flatness.

As shown in Figure 2, nanocrystalline nickel coating was electrodeposited on the substrate material-304 stainless steel(1Cr18Ni9). In the next procedure, high-energy density laser beam would be used to scan and melt the Ni coating over the specimen. During the rapid solidification generated by laser beam, the specimen surface formed a new layer of coating, as seen in Figure 3, that quite differed from substrate material composition, which provided substrate material surface with better performance such as corrosion resistance. Figure 3 also shows the cross-section of the specimen after laser remelting. It can be clearly seen that there were three zones over the cross-sectional surface: tempered zone, phase transformation hardening zone, and remelted zone [8]. The variation of the coating's microstructure after laser remelting, as shown in the Figure 3, is actually caused by laser's unique characteristics, rapid heating and cooling. When the laser beam is scanning, the coating was cooled dramatically from the melting state. The nucleus has no sufficient time grown-up and therefore forms a dense and fine crystal structure in the remelting layer. Simultaneously, under the laser radiation, the metal atoms of the deposit layer and the matrix mutually diffuse each other, which becomes a new metallic bond between atoms. This transition successfully generates a metallurgical bonding between the substrate material of stainless steel and the Ni coating, from the originally mechanical bonding, so that the adhesion of the protective coating with the substrate will be strengthened [9].

Figure 4 illustrates the corrosion kinetics of samples including substrate material-1Cr18Ni9, laser-processed specimens, jet electrodeposited specimens, and the specimens with jet electrodeposition and laser scanning process. As seen in the corrosion rate curve, during the first 8 h of exposure, the substrate material was in a very quick corrosion and then the corrosion rate became slow. In the first 20 h, substrate material appeared to deteriorate rapidly while the nanocomposite-coated ones seem to keep a gradually declining trend. Based on such results, it may be assumed that the nanocomposite exhibits an initial and transient corrosion stage that is different from the corrosion of 1Cr18Ni9 counterpart. At the onset of corrosion, the alloy may form a NiO scale containing many defects, such as pores and microcracks. In this case, the corrosive liquid penetrates

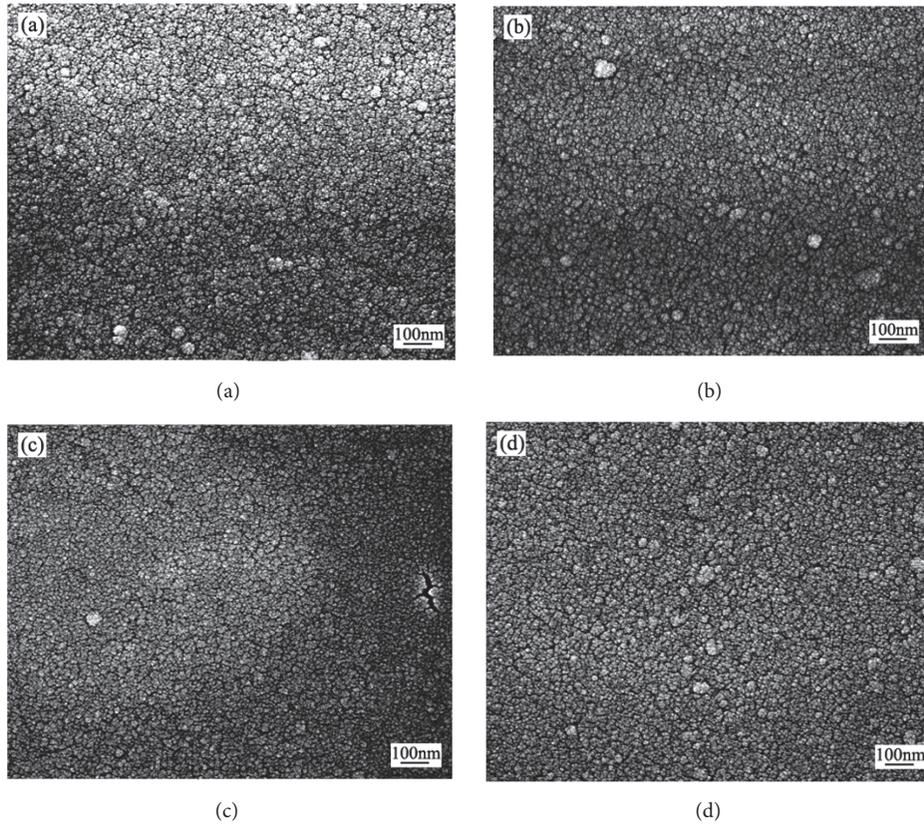


FIGURE 2: SEM micrograph under different current densities: (a) 20 A/dm²; (b)30 A/dm²; (c) 40 A/dm²; (d) 50A/dm².

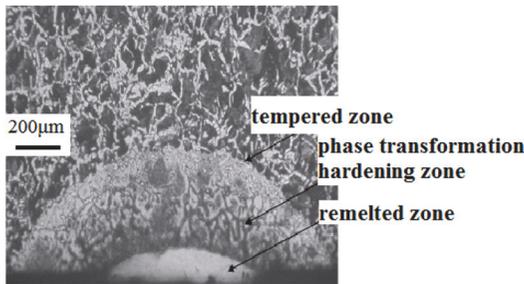


FIGURE 3: Laser melting area micrograph at view of 400 x metallographic microscope 200µm.

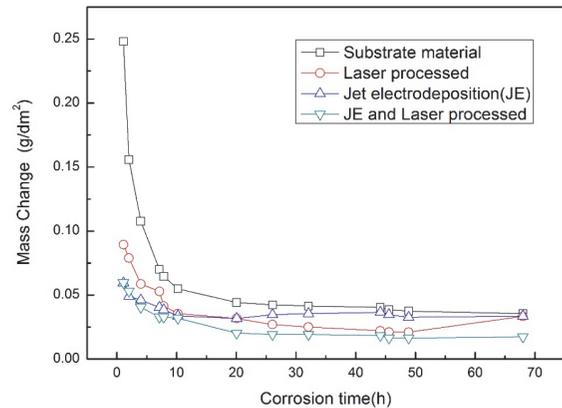


FIGURE 4: Corrosion rate versus time curve.

through the growing scale through these defects and reaches the scale/alloy interface.

Also from Figure 4, the corrosion rate is seen to be greatly reduced after 20 h. This is possibly associated with two factors. Firstly, the loss of the coated salt that was formed by corrosive liquid penetration would occur in the later exposure stage. Secondly, Cr-rich oxides are progressively formed below the NiO layer, which may significantly mitigate the continuous corrosive attack. With regard to the influence of laser, in contrast with other three curves in Figure 4, the curve representing compound process, namely, those specimens processed by both jet electrodeposition and laser scanning, can be observed to have better performance,

while those specimens only receiving the treatment of jet electrodeposition show higher corrosion rate than the ones merely processed by laser. The specimens only treated by jet electrodeposition have much higher corrosion rate after 26h, which is better only than the substrate material, unprocessed 304 stainless steel. This phenomenon might be related to the infiltration of the corrosive medium. On one hand, the laser enhancement refines the grains of electrodeposited coating. On the other hand, the corrosive medium from infiltrating is hardly to travel to the substrate material through the interface

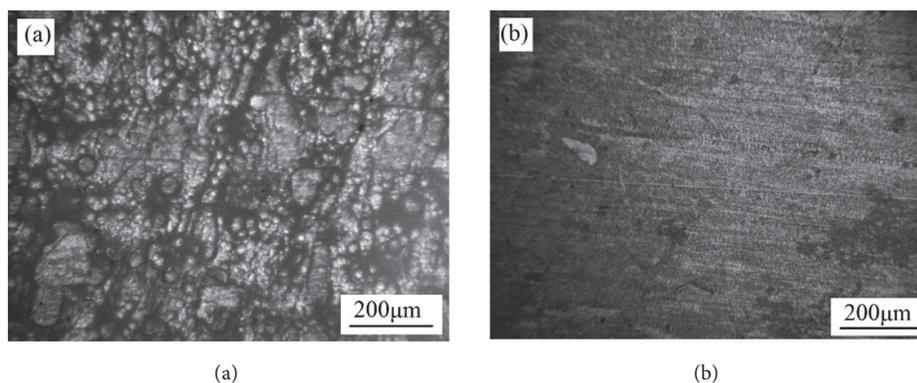


FIGURE 5: A metallographic image of the surface of the Ni coating after corrosion at view of 400 \times : (a) without laser processed and (b) with laser processed.

of coating and substrate which have already become denser metallurgical bonding [11, 12].

In terms of the corrosion failure mechanism of deposit coating, many researchers believe that it is the corrosion medium entering along the pores into the deposit that leads to the corrosion of metal substrates as well as the material peeling [13, 14]. In general, the key to improving the erosion of the deposit layer is to reduce the amount of the through-holes that actually plays an important role as corrosion medium penetrating path. However, nickel deposits are more susceptible to erosion due to its special high porosity. If the porosity was decreased in an appropriate way, the corrosion resistance of the Ni coating might be improved.

In fact, in the use of jet electrodeposition and by laser strengthening effect, all are in favor of the decrease of the porosity. This variation of microstructure favorably restrains corrosive medium from entering inside the coating. Simultaneously, many research results show that the laser remelting can eliminate the deposit's lamellar structure and make deposits into isometric and dendrites, therefore contributing to eliminating loose, porosity, and other defects in the coating layer. These strengthening effect prevents the infiltration of corrosive medium as well. However, in the process of laser remelting, laser, coating, and substrate have very complex interaction mutually. There exist not only thermal reactions between laser and nanocrystalline deposits, but also mutual infiltration between the deposit and substrate material. The compound process anticorrosion mechanism still needs to be further explored.

Figure 5 displays the morphology of the specimens after corrosion. According to Figure 5(a), the corrosion pits evenly are distributed on the surface of the specimen, indicating that most of corrosion occur at the surface of the specimens. In comparison, according to Figure 5(b), the specimen after laser remelting seems relatively smooth and flat, proving that laser remelting after jet electrodeposition can improve the corrosion resistance of the specimens.

4. Conclusions

We herein demonstrated that the corrosion resistance of stainless steel substrate can improve considerably by coating

their surfaces with Ni coatings using Jet electrodeposition. With the current density reaching 40 A/dm², a dense and grain-refining coating was achieved in favor of prevention of corrodent infiltrating. The Ni coating underwent the following laser treatment to form remelting area, which can further accelerate the formation of dense and fine structure and transform the originally mechanical combination between substrate and coating to the metallurgical combination, thus enhancing anticorrosion behavior again. The specimens processed by jet electrodeposition and laser scanning have the well corrosion performance, better than the specimens Ni coated by jet electrodeposition and the bare substrate material.

Data Availability

The data used to support the findings of this study are available from the corresponding author upon request.

Conflicts of Interest

The authors declare that there are no conflicts of interest regarding the publication of this paper.

Acknowledgments

This research was financially supported by the National Natural Science Foundation of China (51305178); Natural Science Foundation of Jiangsu Provincial University (17KJD460005); and Xuzhou Science and Technology Project (KC16SG285), which the authors would greatly appreciate.

References

- [1] K. R. Sriraman, S. G. S. Raman, and S. K. Seshadri, "Corrosion behaviour of electrodeposited nanocrystalline Ni-W and Ni-Fe-W alloys," *Materials Science and Engineering: A Structural Materials: Properties, Microstructure and Processing*, vol. 460-461, pp. 39-45, 2007.
- [2] G. Qiao, T. Jing, N. Wang et al., "High-speed jet electrodeposition and microstructure of nanocrystalline Ni-Co alloys," *Electrochimica Acta*, vol. 51, no. 1, pp. 85-92, 2005.

- [3] M. Kunieda, R. Katoh, and Y. Mori, "Rapid prototyping by selective electrodeposition using electrolyte jet," *CIRP Annals—Manufacturing Technology*, vol. 47, no. 1, pp. 161–164, 1998.
- [4] I. Baskaran, T. S. N. S. Narayanan, and A. Stephen, "Pulsed electrodeposition of nanocrystalline Cu-Ni alloy films and evaluation of their characteristic properties," *Materials Letters*, vol. 60, no. 16, pp. 1990–1995, 2006.
- [5] L. Wang, J. Zhang, Y. Gao, Q. Xue, L. Hu, and T. Xu, "Grain size effect in corrosion behavior of electrodeposited nanocrystalline Ni coatings in alkaline solution," *Scripta Materialia*, vol. 55, no. 7, pp. 657–660, 2006.
- [6] M. S. Rajput, P. M. Pandey, and S. Jha, "Modelling of high speed selective jet electrodeposition process," *Journal of Manufacturing Processes*, vol. 17, pp. 98–107, 2015.
- [7] H. Fan and Y. Huang, "Improved microstructure and corrosion resistance of nanostructured nickel coating via pulsed jet plating," *Corrosion Engineering, Science and Technology*, vol. 48, no. 1, pp. 48–50, 2013.
- [8] K. A. Qureshi, N. Hussain, J. I. Akhter, N. Khan, and A. Hussain, "Surface modification of low alloy steel by laser melting," *Materials Letters*, vol. 59, no. 6, pp. 719–722, 2005.
- [9] Y. Yao, S. Yao, L. Zhang, and H. Wang, "Electrodeposition and mechanical and corrosion resistance properties of Ni-W/SiC nanocomposite coatings," *Materials Letters*, vol. 61, no. 1, pp. 67–70, 2007.
- [10] X. H. Fang, "Research progress for ultrasound-assisted electroplating of ni and ni-based composite coatings," *Journal Materials Protection*, vol. 41, no. 5, pp. 58–60, 2008.
- [11] E. Celik, I. Ozdemir, E. Avci, and Y. Tsunekawa, "Corrosion behaviour of plasma sprayed coatings," *Surface and Coatings Technology*, vol. 193, no. 1-3, pp. 297–302, 2005.
- [12] Y.-L. Gao, C.-S. Wang, M. Yao, and H.-B. Liu, "The resistance to wear and corrosion of laser-cladding Al₂O₃ ceramic coating on Mg alloy," *Applied Surface Science*, vol. 253, no. 12, pp. 5306–5311, 2007.
- [13] E. Çelik, A. Demirkıran, and E. Avcı, "Effect of grit blasting of substrate on the corrosion behaviour of plasma-sprayed Al₂O₃ coatings," *Surface and Coatings Technology*, vol. 116-119, pp. 1061–1064, 1999.
- [14] G. Gravanis, A. Tsetsekou, T. Zambetakis, C. Stournaras, and E. Hontzopoulos, "Ceramic coatings and laser treatment," *Surface and Coatings Technology*, vol. 45, no. 1-3, pp. 245–253, 1991.

Research Article

Effect of Rare-Earth Elements on the Corrosion Resistance of Flux-Cored Arc-Welded Metal with 10CrNi3MoV Steel

Kai Wang ^{1,2}, Qinghua Lu,¹ Zexin Jiang,³ Yaoyong Yi,² Jianglong Yi ², Ben Niu,² Jinjun Ma,³ and Huiping Hu¹

¹Foshan University, Foshan, China

²Guangdong Welding Institute (China-Ukraine E. O. Paton Institute of Welding), Guangzhou, China

³Guangzhou Shipyard International Co., Ltd, Guangzhou, China

Correspondence should be addressed to Kai Wang; hfutwk927@gmail.com

Received 19 December 2017; Accepted 25 March 2018; Published 12 June 2018

Academic Editor: Flavio Deflorian

Copyright © 2018 Kai Wang et al. This is an open access article distributed under the Creative Commons Attribution License, which permits unrestricted use, distribution, and reproduction in any medium, provided the original work is properly cited.

We modified the content of rare-earth elements (REE) in the flux-cored wire used to produce welds of high-strength low-alloy (HSLA) steel. The effect of REE addition on the microstructure as well as on the mechanical and electrochemical properties of the welded metal (WM) was investigated. REE-modified welded metals show very different responses during electrochemical impedance spectroscopy and the potentiodynamic polarization tests. The results indicate that the addition of REE of 0.3 wt.% facilitates a more uniform microstructure and improves both mechanical properties and corrosion resistance in welded metals.

1. Introduction

Welding is a common joining method, which is commercially used worldwide. The welding process for the manufacturing of a steel ship, for example, takes up 30%~40% of the overall production time. Flux-cored arc welding (FCAW) is a semiautomatic or automatic arc-welding process that involves the fusion of a flux-cored wire metal with a base metal. FCAW in particular is one of the most widely used welding techniques in the modern shipbuilding industry. The properties of FCAW joints are largely determined by the used welding consumables and the base metals used during the welding process.

10CrNi3MoV steel is a typical high-strength low-alloy steel (HSLA) that combines strength, toughness, and weldability thanks to Q-tempered processing. This type of steel is generally used as hull material in high-performance marine vehicles [1]. Due to the high-performance requirements of the welded joints in these vehicles, both low-temperature impact toughness and corrosion resistance of the welded metal determine the overall performance of 10CrNi3MoV steel.

One of the most effective approaches to improve toughness and corrosion resistance of a welded metal is to alter the welded metal composition by introducing alloying elements

via the flux-cored wire to act as FCAW filler metals [2]. Generally, rare-earth elements (REE) are considered the most suitable microalloying elements for any mature alloy system. A minor addition of REE into the steel can significantly purify the liquid steel and modify any inclusions, which improves the steel properties [3–5]. The correct REE content can improve both impact toughness and temper brittleness of the welded components. This is due to its effect on grain refinement, grain boundary cleaning, and the suppression of grain boundary embrittlement [6]. Theoretical calculations show [7–9] that REE can increase the grain boundary cohesion in steel, which leads to toughening of the material via grain boundary segregation. Furthermore, the addition of REE can also enhance the high-temperature ductility of steel [10, 11]. Tomita [12] found that the addition of REE to vacuum-melted AF1410 steel can stabilize complex-inclusions and improve toughness. Gao et al. substantially improved the toughness of H13 steel by adding 0.015 wt.% REE, which favors finer and more dispersive inclusions [13]. The addition of REE to welded metals to SAW DH32 steel facilitates both inclusions and a small lattice disregistry, which improves elongation, tensile strength, and impact toughness of welded metals [14, 15]. It has also been reported that REE can improve the corrosion resistance of low-carbon steels [16, 17].

TABLE 1: Chemical composition of REE-Si-Fe (wt. %).

| Ce | La | Nd | Pr | Sm | Ca | Si | Fe |
|-------|------|------|------|------|-----|------|----|
| 12.56 | 4.43 | 1.41 | 0.55 | 4.53 | 3.1 | 40.9 | Re |

TABLE 2: Selected content of REE-Si-Fe for the weld samples in flux-cored wire (flux wt.%).

| Weld Sample | REE-Si-Fe addition |
|-------------|--------------------|
| REE0 | - |
| REE1 | 0.3 |
| REE2 | 0.5 |
| REE3 | 0.7 |
| REE4 | 1.0 |

However, the effects of REE on the features and properties of welded metal for 10CrNi3MoV steel, in particular, have received little attention, and no general agreement on the correct amount of REE in welded metal has been reported.

It is likely that REE elements can enhance the properties of welded metal through microstructural control during FCAW. In this work, the effect of REE addition to the flux-cored wire on both the microstructure and the properties of welded metal was investigated. In particular, we focused on the correlation between REE content and the resulting properties of the joints.

2. Experimental

The 10CrNi3MoV steel plates were arc-welded using flux-cored wires with different REE concentrations. REE (consisting of Ce-rich rare-earth ferrosilicon, REE-Si-Fe). The chemical composition of REE-Si-Fe is shown in Table 1. The flux-cored wires consist of a metal sheath and a powdered core; see Figure 1. They were prepared after the shaping of a cold-rolled strip and the filling of the hollow core with a powdered mixture and a XZ-YCX8 flux-cored wire production machine. In this study, the basic powdered core belongs to a rutile-fluorite alloying system with a filling ratio of 20%. The diameter of the finished wire was 1.2 mm. The chosen REE contents for the powdered cores are shown in Table 2. Five group samples with different REE concentrations in the welded metals were fabricated in the laboratory using identical welding conditions. The chemical composition and mechanical properties of the 10CrMo3NiV steel base metal are shown in Tables 3 and 4. The conditions and parameters for the FCAW process are listed in Table 5. The drawing of the FCAW grooves and welded metal samples for mechanical testing were prepared according to the Chinese standard GB/T17493-2008; see Figure 2.

The chemical composition of the welded metals (except for carbon, C) was determined using a JY ULTIMA inductive coupled plasma emission spectrometer. The C content was determined using a LECO CS600 carbon-sulphur spectrometer. The phases within welded metals were identified with a D/max-III A X-ray diffractometer (XRD). Each welded metal sample was observed and analyzed with a DMM-440D optical microscope (OM) and a JEOLJXA-8100 scanning electron

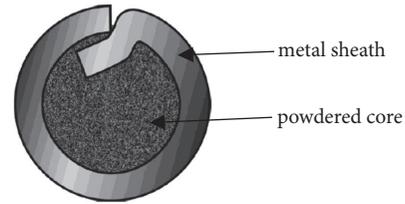


FIGURE 1: Schematic of a flux-cored wire.

microscope (SEM) and its accessory EDX (OXFORD-7412) after grinding, polishing and etching with a 4% nital solution. The microhardness of the welded metal was measured using a HVS-1000 micro Vickers hardness tester with a load of 0.3 kgf, using four points on the same circumference of the 1/2 radius for each sample. Samples for electrochemical impedance spectroscopy (EIS) and potentiodynamic polarization (PP) testing were taken from the center of the welded metals along the longitudinal direction. This was done via linear cutting into squares of 10 mm×10 mm×0.5 mm. Before the electrochemical tests, the samples were polished with 2000-grid sandpaper, degreased with acetone, washed with distilled water, and blow-dried. The working areas of the tested samples were 1cm², and the remaining areas of the samples were sealed with wax. The EIS and PP tests were carried out using an Ametek P4000 electrochemical workstation with a three-electrode system. The working electrode was the tested sample (1 cm² working area), the auxiliary electrode was a Pt plate, and the reference electrode was saturated calomel electrode (SCE). The electrolyte was a 3.5 wt.% NaCl water solution. The working electrode was soaked in the electrolyte in open-circuit-potential (OCP) mode for 30 min before testing. The EIS mode was set as a frequency of 10⁻² Hz ~ 10⁵ Hz versus OCP with an AC drive signal amplitude of ±5 mV. The following potentiodynamic polarization mode was chosen for a scanning potential range of -1.0 V ~ +1.5 V versus OCP with a scanning speed of 1 mV/s. The polarized samples were observed with a SEM.

3. Results and Discussion

3.1. Chemical Composition Analysis. The chemical compositions of the welded metals (only key elements) are listed in Table 6. The REE addition causes significant changes of the C and Ni content but only with slight variations in the Si, Mn, and Mo content of the welded metals. Furthermore, there are rare changes in the Al and Ti content of the welded metals.

3.2. Mechanical Properties of the Welded Metals. Table 7 and Figure 3 show the mechanical properties of the FCAW-welded metals with different REE added. In Figure 3(a), the values for tensile strength, yield strength, and elongation ratio increase suddenly after the REE addition of 0.3%. The above test results, however, indicate a gradual decrease when the REE content exceeds 0.3%, which is lower than for the REE-free welded metal (REE0) before the REE addition of 1.0%. Figure 3(b) shows the low-temperature impact energy for the welded metals. The impact energy for all welded metals with added REE is higher than for REE-free welded metals,

TABLE 3: Chemical composition of 10CrNi3MoV steel (wt. %).

| C | Si | Mn | Ni | Mo | Cr | V | P | S |
|------|------|------|------|------|------|------|-------|-------|
| 0.11 | 0.31 | 0.39 | 2.72 | 0.23 | 1.05 | 0.08 | 0.010 | 0.005 |

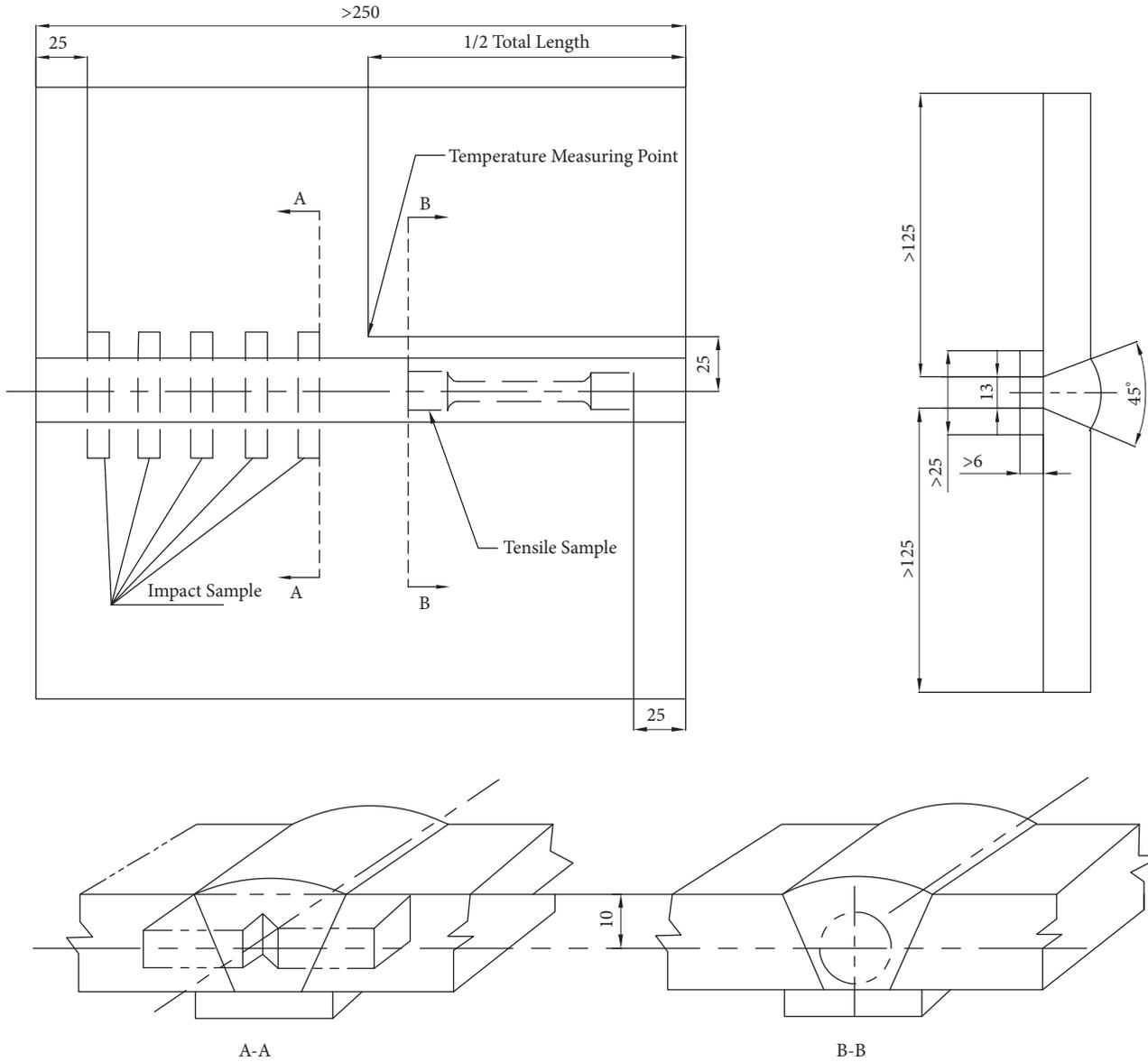


FIGURE 2: Schematic illustrating the grooves in the samples (mm).

TABLE 4: Mechanical properties of 10CrNi3MoV steel.

| Yield Strength/MPa | Tensile Strength/MPa | Elongation/% | A _k -20°C/J |
|--------------------|----------------------|--------------|------------------------|
| 590~745 | 670~850 | ≥16 | ≥80 |

and it increases significantly as the REE content increases to 0.3%. However, the impact energy of the welded metals causes a slight decrease followed by a further REE content increase to 1.0%. The microhardness of the relevant samples is very low. The slight fluctuation may be due to the presence

of C in the welded metals [18]. This is because a higher C content in the REE1 and REE2 welded metals was detected; see Table 6. In other words, adding REE improves indeed the mechanical properties of the welded metals significantly. The correct addition of the right amount of REE can improve the strength of the welded metals, while REE adding over 0.7% reduces the strength.

3.3. *Microstructural Analysis.* Figure 4 shows the optical morphologies of the FCAW-welded metals with different REE additions. It is hard to identify any prior austenite

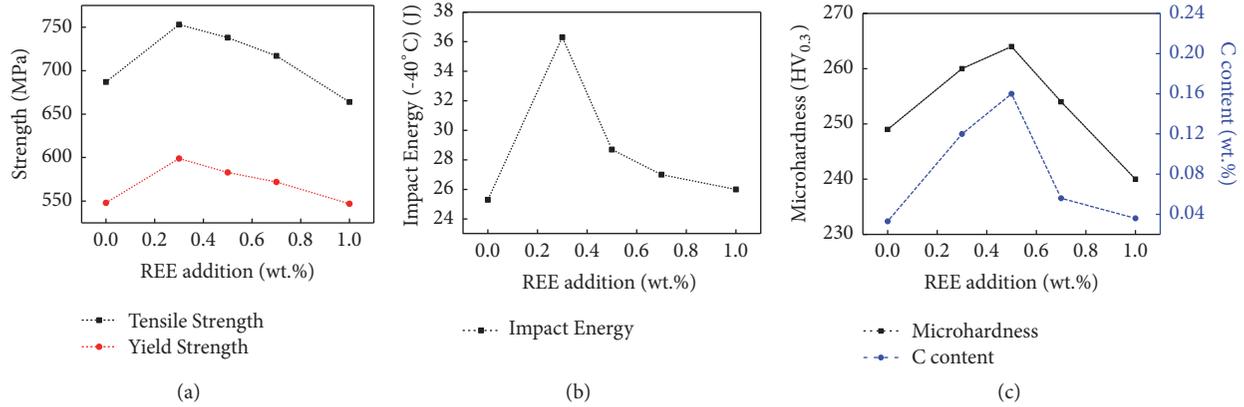


FIGURE 3: Mechanical properties of FCAW-welded metals for different REE contents: (a) tensile properties; (b) low-temperature impact toughness; and (c) microhardness.

TABLE 5: Welding parameters for FCAW.

| | |
|--------------------------------|-------------------------------------|
| Plate form and dimensions (mm) | Flat, 300 ×150 ×14 |
| Welding Machine | EWM |
| Power Mode | DCEP |
| Electrode | As-prepared wires |
| Protective gas | M21 (80% Ar + 20% CO ₂) |
| Gas flow rate (L/min) | 17 ~ 20 |
| Preheating temperature (°C) | 150 |
| Current (A) | 240 |
| Voltage (V) | 26 |
| Interpass temperature (°C) | 150 ~ 180 |
| Welding speed (mm/s) | 6.3 ~ 7.9 |
| Cooling after welding | Air |

grain boundaries (PAGB), which means a complete phase transformation (to ferrite) occurred during cooling. The microstructure of REE-free welded metal consists of proeutectoid ferrites (PF), acicular ferrites (AF), and a small amount of bainites (B); see Figure 4(a). No bainite was formed in the welded metals with REE added; see Figures 4(b)–4(e). This indicates that a microstructure of different forms of ferrites, i.e., AF, lath ferrites (LF), and granular ferrite (GF), was formed. After REE addition of 0.3% and 0.5%, as shown in Figures 3(b) and 3(c), the microstructure of the welded metals becomes more refined. In addition, the PF size is limited due to inhibited nucleation of PF. Furthermore, there is increased nucleation and AF growth due to the added REE. Some small LF formed due to the continuous growth of AF. The total amount of grain boundaries increases clearly because of the formation of AF. There is a high density of dislocations in the interior of the acicular ferrites, with few low-angle boundaries. These require higher energy for the microcracks to cross the AF, which improves crack growth-resistance [19]. Because there are many large-angle grain boundaries among adjacent grains, which can increase the resistance of dislocation motion and the plastic deformation, the formation of AF increases both strength and low-temperature impact toughness [20, 21]; see Figure 3. When

the REE content REE exceeds 0.5%, the inhibiting property of PF nucleation is restored. This is a result of the pollution of the grain boundaries by REE, which appears as disproportionate growth of PF [22]; see Figures 4(d) and 4(e). The REE addition of 0.3% and 0.5% can refine the grains by promoting the formation of AF effectively. This improves the mechanical properties of welded metals. When the REE content exceeds 0.5%, AF is limited with its growth promotion of LF and PF. This leads to a reduction in strength and low-temperature affects the toughness of the welded metals.

If second-phase particles are of suitable size with a uniform distribution, they could act as nuclei during the solidification process. Studies [23, 24] show that particles finer than 0.6 μm facilitate the nucleation of ferrite, while even more effective nucleation occurs in the 0.2–0.6 μm range. Figure 5 shows the SEM images of the welded metals with different amounts of REE added. The number of second-phase particles in the REE-free welded metal is small, and their size is relatively large (up to 3.3 μm in diameter); see the dark spots in Figure 5(a). It is clear that the number of second-phase particles increases significantly, while the average size decreases gradually REE for higher REE content; see Figures 5(b)–5(e). This is substantially different from the REE-free welded metal, based on the measurement of more than 100 particles. Following a further increase of the REE content (up to 1.00%), the number of second-phase particles continues to increase with a discrete distribution and reduced average size. Some second-phase particles (on a microscale) are beginning to appear in the field of view.

Both the number of second-phase particles and the fraction of different grain sizes were counted using the SEM images. The statistical results are shown in Figure 6. For a higher REE content, the size range for the second-phase particles becomes gradually smaller. Some oversized particles (up to 3.3 μm in the REE-free welded metal) do not appear in the REE-added welded metals. The fractions of second-phase particles between 0.2 and 0.6 μm in Figures 6(a)–6(e) are 70.2%, 77.8%, 74.4%, 49.9%, and 46.4%, respectively. This shows the first increasing and then decreasing trend if the REE content increases. However, the fractions of particles

TABLE 6: Chemical composition of the welded metals (wt. %).

| welded metal sample | C | Si | Mn | Mo | Al | Ti | Ni |
|---------------------|-------|------|------|------|-------|-------|------|
| REE0 | 0.033 | 0.30 | 1.59 | 0.23 | 0.013 | 0.030 | 2.39 |
| REE1 | 0.12 | 0.25 | 0.97 | 0.11 | 0.011 | 0.028 | 1.07 |
| REE2 | 0.16 | 0.29 | 1.44 | 0.17 | 0.014 | 0.031 | 1.77 |
| REE3 | 0.056 | 0.42 | 1.47 | 0.23 | 0.014 | 0.029 | 2.41 |
| REE4 | 0.036 | 0.33 | 1.42 | 0.25 | 0.013 | 0.032 | 2.34 |

TABLE 7: Mechanical properties of the welded metals with different amounts of REE.

| welded metal | Tensile Strength/MPa | Yield Strength/MPa | Elongation /% | Average Impact Energy at -40°C/J | Micro-hardness/HV _{0.3} |
|--------------|----------------------|--------------------|---------------|----------------------------------|----------------------------------|
| REE0 | 687 | 548 | 21.2 | 25.3 | 249 |
| REE1 | 753 | 599 | 22.5 | 36.3 | 260 |
| REE2 | 738 | 583 | 20 | 27.7 | 264 |
| REE3 | 717 | 572 | 14.2 | 27 | 254 |
| REE4 | 664 | 547 | 14.5 | 28 | 240 |

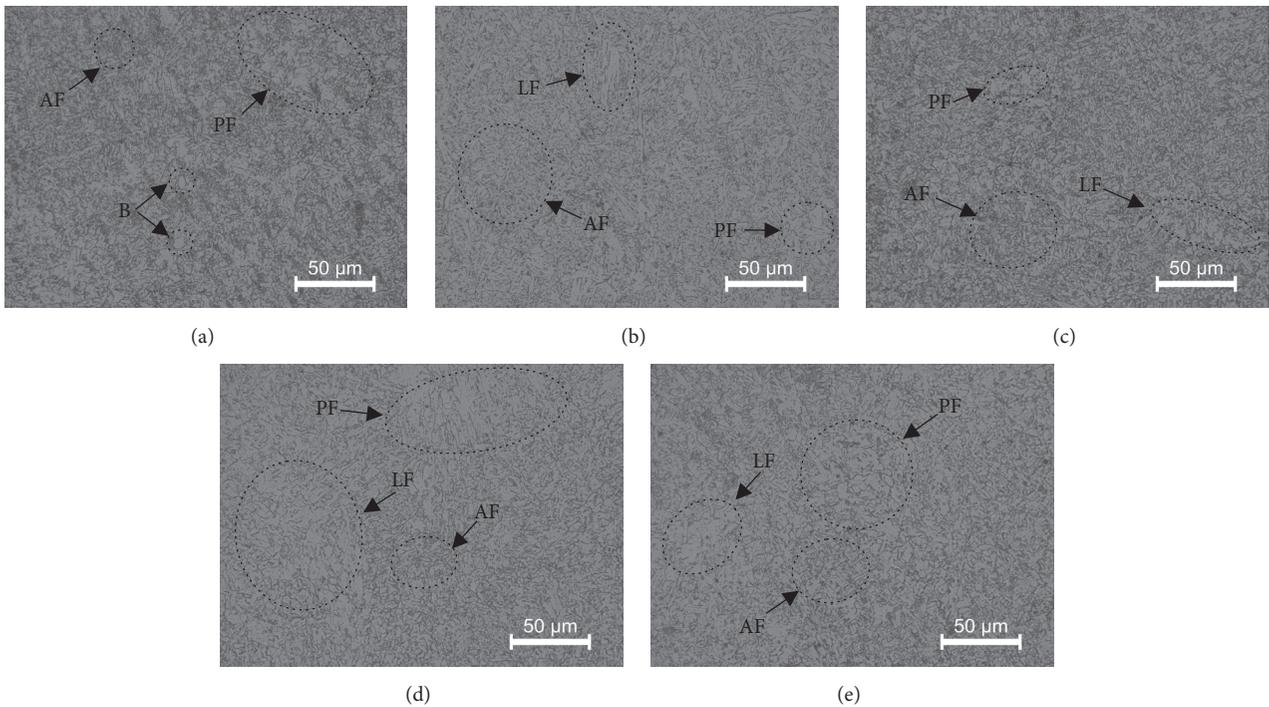


FIGURE 4: OM images of FCAW-welded metals for different REE contents:(a) REE-free, (b) 0.3 wt.%, (c) 0.5 wt.%, (d) 0.7 wt.%, and (e) 1.0 wt.%.

below $0.2 \mu\text{m}$ are 0%, 0%, 8.1%, 28.1%, and 44.9%, respectively, which represents an upward trend for increasing REE content. Hence, a very high REE content can reduce the size of the second-phase particles, and the slope describing the mechanical properties of welded metals becomes negative. When the REE content is optimal (0.3%), most of the second-phase particles form in the size range of 0.2 to $0.6 \mu\text{m}$, which facilitates the formation of AF and results in the best mechanical performance of welded metals.

The EDS results for the second-phase particles are shown in Table 8. There are mainly three elements (Fe, Mn, and Ni) in the matrix, with a fluctuating variation of the components.

However, the types and compositions of the elements in the particles of different samples are somewhat different, whose main elements consisted of O, Al, Si, Ti, Mn, and Fe. Because the particles are located within the matrix, the EDS determination will include part component of the matrix into the results. Moreover, the content of Fe is about 45%, the highest of all elements; it can be considered that the Fe mainly stems from the matrix. There is a small amount of S in the second-phase particles in three groups of samples with 0.3% REE, 0.5% REE, and 0.7% REE, respectively. A certain amount of S element in the alloy steel is beneficial to the improvement of its machinability. However, for the welded

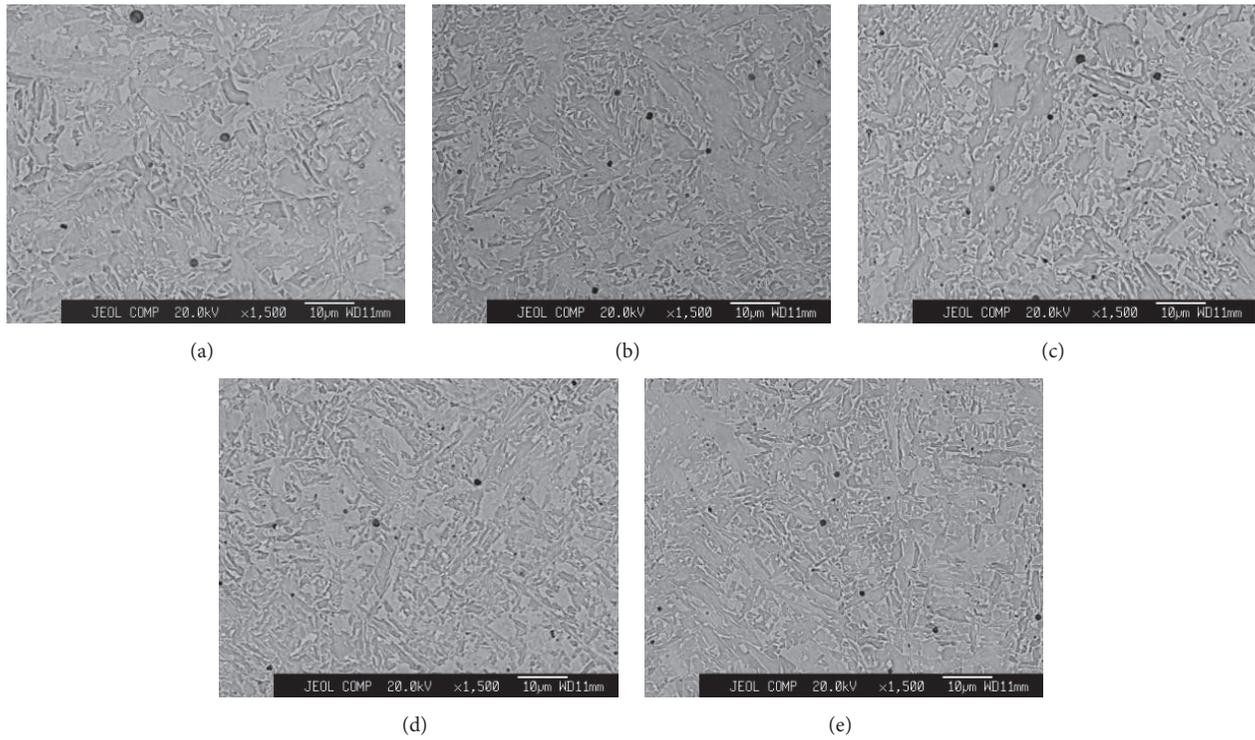


FIGURE 5: Typical SEM images of welded metals with different REE contents: (a) REE-free, (b) 0.3 wt.%, (c) 0.5 wt.%, (d) 0.7 wt.%, and (e) 1.0 wt.%.

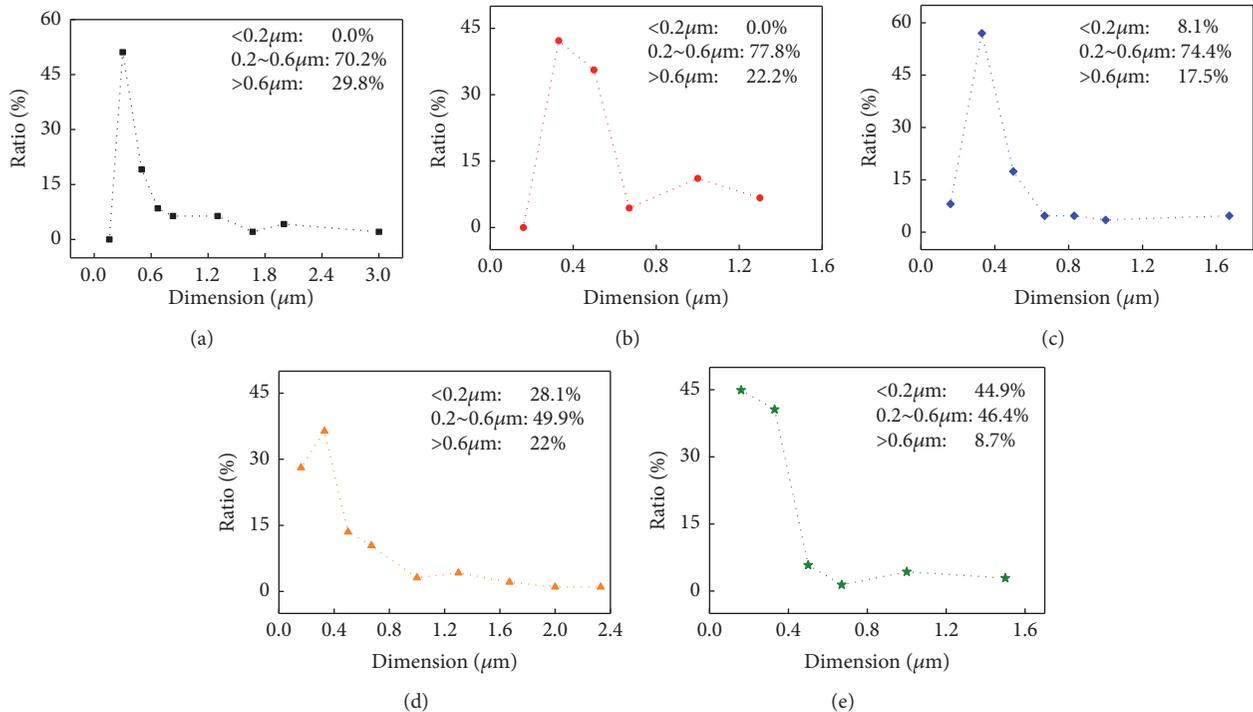


FIGURE 6: Dimension (size) and ratio of the second-phase particles in welded metals with different REE contents: (a) REE-free, (b) 0.3 wt.%, (c) 0.5 wt.%, (d) 0.7 wt.%, and (e) 1.0 wt.%.

TABLE 8: EDS results of the matrix or second-phase particles for each welded metal with varying REE content.

| Items | Matrix | | | | | Second-phase particle | | | | | |
|-------|--------|-------|------|-------|------|-----------------------|-------|-------|-------|------|------|
| | Mn/% | Fe/% | Ni/% | O/% | Al/% | Si/% | Ti/% | Mn/% | Fe/% | S/% | Ni/% |
| REE0 | 1.42 | 96.27 | 2.31 | 16.86 | 4.26 | 2.57 | 14.12 | 18.55 | 42.91 | / | 0.73 |
| REE1 | 1.72 | 96.13 | 2.15 | 16.92 | 3.91 | 6.47 | 6.73 | 15.34 | 49.85 | 0.14 | / |
| REE2 | 2.39 | 94.99 | 2.62 | 14.38 | 5.25 | 5.10 | 9.29 | 17.32 | 46.65 | 2.01 | / |
| REE3 | 1.43 | 95.61 | 2.96 | 20.61 | 6.09 | 6.00 | 12.25 | 13.30 | 39.25 | 2.50 | / |
| REE4 | 1.23 | 96.39 | 2.38 | 16.68 | 4.53 | 6.66 | 6.48 | 14.99 | 50.67 | / | / |

metal, a tiny amount of S can greatly reduce its performance. In this work, it can be found that correct REE content can aid S to accumulate into the second-phase particles, which originally dissolved in the matrix. Thus, it will reduce the harmful effects on the matrix to increase the strength of weld metal. This conclusion is consistent with the above discussion of the mechanical properties in Figure 2. With the increasing REE addition, the relative contents of the nonmetallic elements O, Si, and S in the second-phase particles show a rising trend, and the content of Al and Fe increased slightly, while Ti and Mn decreased slightly. Mn and Ti tend to deoxidize and remove impurities to form refractory-phase impurities like MnS or TiO, combined with S or O. These discharged from the welded metal into the welding slag with the right content of nonmetallic elements O and S. Enrichment with oxygen in the welded metal tends to increase the possibility of the generation of weld blowholes, which can induce cracks and become the sources of microcracks under external load. This decreases both the strength and the low-temperature impact toughness of the weld metal. Sulphur could form banded FeS, when combined with Fe and weaken the consistency of the weld metal. The right amount of Si cannot only act as a deoxidant but also form Al-Mn silicate particles and facilitate nucleation. Therefore, adding REE causes the elements of O, S, and Si to accumulate in the second-phase particles instead of the matrix, which purifies the matrix and refines the grains or microstructure effectively. As a result, the strength and low-temperature impact toughness of the weld metal are improved using REE.

Phase compositions for each sample were determined using XRD, and the results are shown in Figure 7. The matrix consists of α -Fe (AF), and the second phase consists mainly of an Al-Ti phase and $(Al, Mn)_x SiO_4$ (Al-Mn silicate) phase. Furthermore, $(Al, Mn)_x SiO_4$ is composed of a variety of metallic or nonmetallic oxides including Al_2O_3 , MnO, and SiO_2 , which play a strong role in deoxygenation and greatly reduce oxygen in the welded metals. During the solidification process of the weld pool, the second-phase particles, which consist of Al_2O_3 , MnO, and SiO_2 , formed preferably with high surface-energy [25], where the crystal nuclei for ferrite form. In this way it can substantially reduce the potential barrier for nucleation during the phase transformation from γ to α phase. The second-phase particles in the weld metal are mostly a complex mixture of different phases. Therefore, each phase can be regarded as a high-energy region and form a nucleus for acicular ferrite. Multidimensional nucleation occurs at the end and causes acicular ferrite to overlap, which results in refined grains.

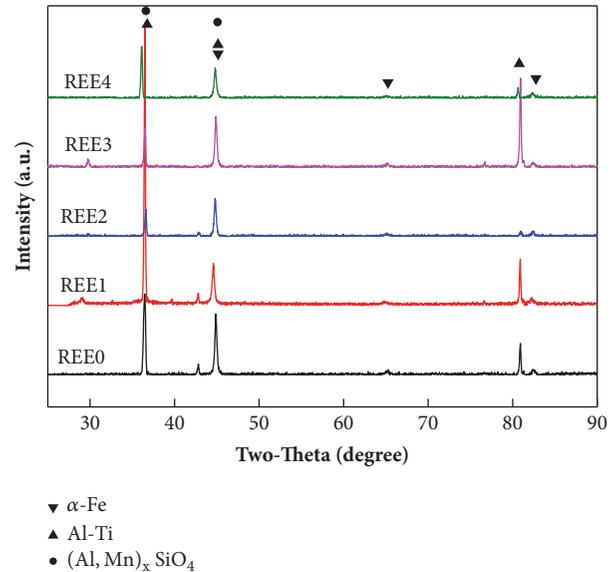


FIGURE 7: XRD analysis results of different FCAW-welded metals.

3.4. Electrochemical Properties. The EIS responses of the FCAW-welded metals with different REE contents in a 3.5 wt.% NaCl solution were measured to study effects on the electrochemical properties. Our results are shown as Nyquist, Bode, and Bode-phase plots in Figure 8. The Nyquist plots of all welded metals are imperfect semicircles (Figure 8(a)), i.e., capacitive arcs with similar capacitive response. Only a single depressed semicircle for each welded metal appears in the Nyquist plots, which indicates that only one time-constant is present in EIS. The imperfect semicircle-diameter for REE4 is the largest. It shows the largest capacitive arc and the best antidissolution properties. The imperfect semicircle-diameters for REE welded metals, with REE added (REE1, REE2 and REE3), are smaller than the REE-free welded metal. In the low-frequency range of the Bode plots (Figure 8(b)), the samples with higher electrical resistance possess stronger corrosion resistance. This is consistent with our analysis of the above Nyquist plots. In Figure 8(c), each spectrum shows one single sharp peak, with maximum phase-angles below 70° . This means the EIS capacitive response of the welded metals, with or without REE addition, is not pure or ideal. Hence, there is only one time-constant and low reactive resistance, which is similar to the results reported by R.M. Domene et al. [26].

To simulate the measured impedance data and explain the general corrosion process, the equivalent circuit shown

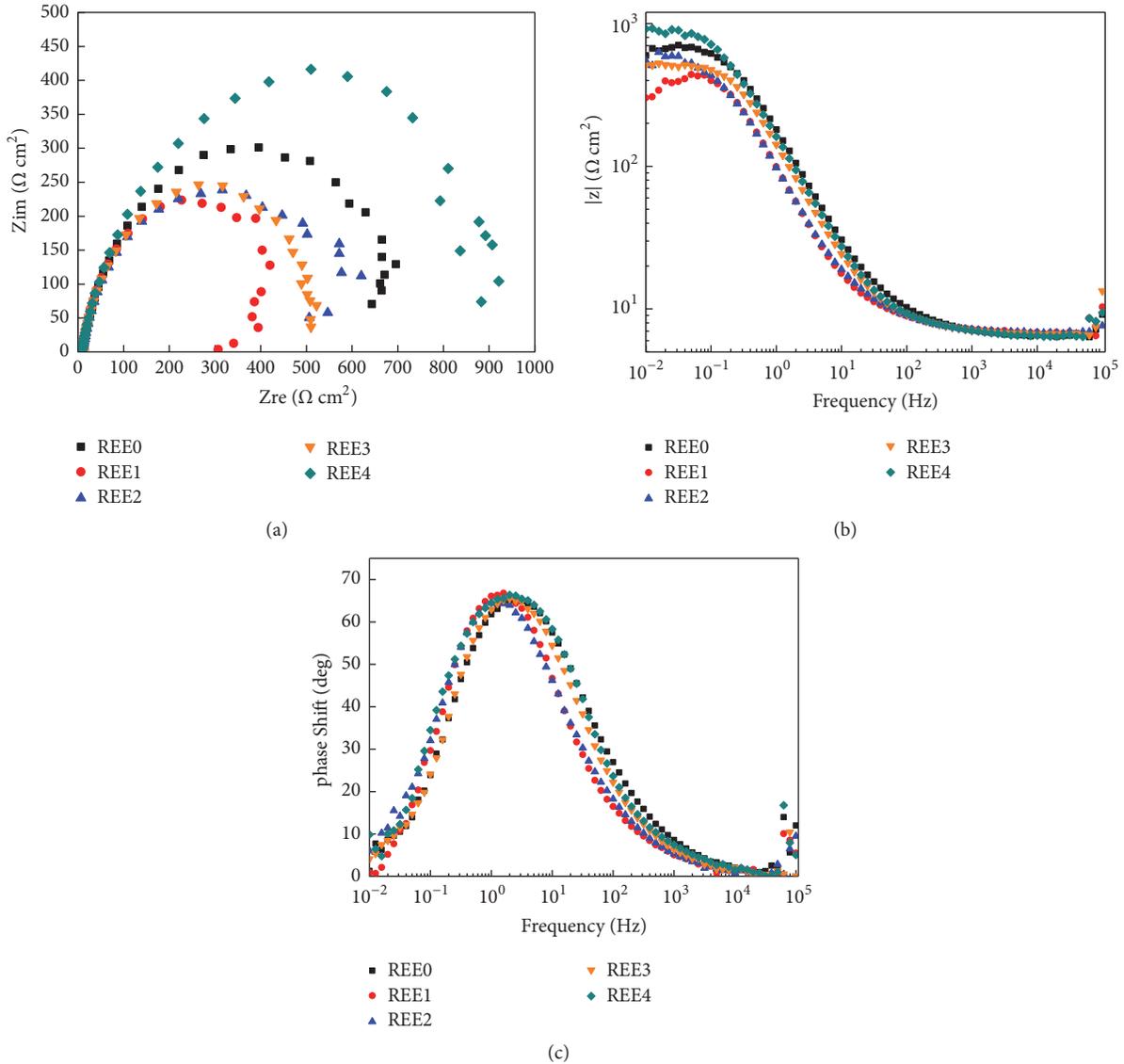


FIGURE 8: (a) Nyquist, (b) Bode, and (c) Bode-phase plots for the FCAW-welded metals with different REE contents versus OCP in a 3.5wt% NaCl solution.

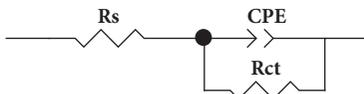


FIGURE 9: Equivalent circuit used to model the experimental EIS data.

in Figure 9 was adopted. The variations of the impedance parameters are shown in Table 9, and the respective errors are below 5%. Consistent with the active dissolution mechanism, R_s is the solution resistance, and R_{ct} represents the charge-transfer resistance from the metal to the electrolyte, which can be defined as the corrosion resistance for the sample in the electrolyte. Furthermore, C_{PE} accounts for the constant phase element corresponding to the metal in this equivalent model, as reported by Y. Chen et al. [27]. The welded metal

TABLE 9: Impedance parameters for the EIS-tested welded metals.

| welded metals | R_s ($\Omega\text{-cm}^2$) | Capacitance (F) | R_{ct} ($\Omega\text{-cm}^2$) |
|---------------|--------------------------------|-----------------|-----------------------------------|
| REE0 | 8.03 | 0.0006136 | 637.3 |
| REE1 | 8.17 | 0.001366 | 401.7 |
| REE2 | 8.19 | 0.001321 | 529.7 |
| REE3 | 8.13 | 0.0008468 | 493.8 |
| REE4 | 7.89 | 0.000742 | 843.7 |

(with 1.00 wt.% REE addition) has the highest R_{ct} (983.0 $\Omega\text{-cm}^2$), and the REE1 welded metal has the lowest R_{ct} (447.6 $\Omega\text{-cm}^2$). Only the REE4 welded metal with 1.00 wt.% REE content shows a higher R_{ct} than its counterpart for the REE-free welded metal.

TABLE 10: Electrochemical data of the welded metals with different REE contents as obtained from potentiodynamic polarization measurements in 3.5 wt.% NaCl solution.

| welded metals | E_{corr} (mV) | I_{corr} ($\mu\text{A}/\text{cm}^2$) | R_p (Ohms/ cm^2) |
|---------------|------------------------|---|------------------------------|
| REE0 | -344 | 24.9 | 10472 |
| REE1 | -546 | 13.4 | 1945.7 |
| REE2 | -544 | 14.0 | 1862.5 |
| REE3 | -403 | 13.6 | 1918.3 |
| REE4 | -527 | 16.5 | 1579.5 |

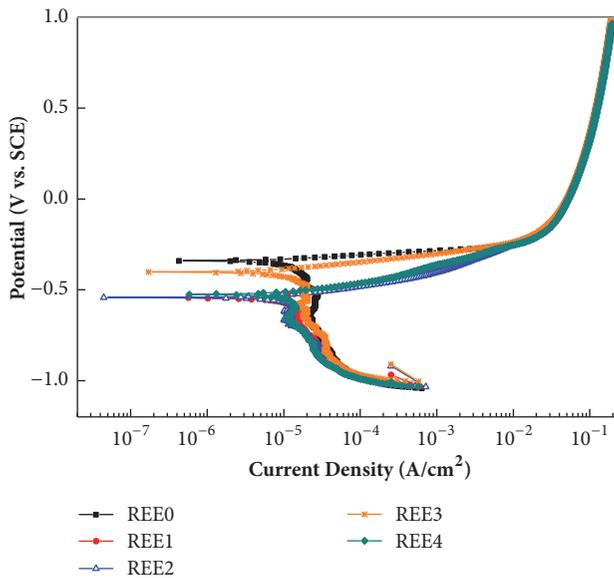


FIGURE 10: Potentiodynamic polarization curves for the welded metals with different REE contents.

After the EIS tests, potentiodynamic polarization measurements were carried out, in a 3.5 wt.% NaCl solution at room temperature. The results are shown in Figure 10 and Table 10. Corrosion potential (E_{corr}) is a static indicator for electrochemical corrosion resistance to describe corrosive susceptibility of a material. In this study, all welded metals with REE show a lower corrosion potential than the REE-free welded metal; see Table 10. The REE-free welded metal has the highest E_{corr} (-344 mV), while the REE1 with the minimum REE addition has the lowest E_{corr} (-546 mV). This indicates a small REE addition has already a significant effect on the corrosive susceptibility in welded metals. However, higher corrosive susceptibility does not mean the material corrodes easily. According to the Tafel rule, corrosion current density (I_{corr}) is a key factor and closely related to the corrosion-dissolution rate. Furthermore, the related polarization resistance (R_p) is used to determine the corrosion rate at any given time. In addition, lower I_{corr} and higher R_p indicate a higher corrosion resistance. The polarization curves for all welded metals with or without REE show typical signs of active dissolution in the 3.5 wt.%

NaCl solution. The active dissolution mechanism is further confirmed by the high I_{corr} compared to the calculated 10 $\mu\text{A}/\text{cm}^2$ for all welded metals; see Table 10. REE-free welded metal (REE0) has the highest I_{corr} (24.9 $\mu\text{A}/\text{cm}^2$) and the lowest R_p (10472 Ohms/ cm^2). REE could retard the anodic process and cathode process to reduce the corrosion rate of welded metal. E_{corr} negatively moved, due to greater effect of REE on the equilibrium potential of cathode reaction [28]. The shapes of all polarization curves are basically the same, which shows that the corrosion mechanism of different REE has not changed. Both I_{corr} and R_p of the welded metals improved, due to the addition of REE. They are better than for Re-free welded metal. The REE addition could reduce the corrosion-dissolution rate and improve corrosion resistance of welded metals. REE1, with an REE addition of 0.2%, shows the strongest corrosion reduction effect, for the highest R_p (1945.7 Ohms/ cm^2) and the lowest I_{corr} (13.4 $\mu\text{A}/\text{cm}^2$). In other words, the reduction effect weakens after adding REE, due to the increased I_{corr} and reduced R_p for REE2 to REE4.

It is interesting that R_{ct} and R_p of the welded metals with different REE contents show different trends. Considering the effect of REE, the difference between the R_{ct} and R_p values might depend on the second-phase particles. The correlations between second-phase particle size and the resistances are shown in Figure 11. It has been reported that a ferrite phase dissolves better during galvanic corrosion [29], and secondary phases act as a pathway in a corrosive environment [30]. The REE second-phase particles have no significant effect on the resistance of REE-free welded metals. REE R_{CT} changes inversely with the size of the second-phase particles in welded metals that contain REE; see Figures 11(b) and 11(d). The second-phase particles provide charge-transfer channels during the EIS tests. Large second-phase particles provide larger channels, which increase the active dissolution efficiency. By increasing the content of REE, the refining particles restrict the charge-transfer process between the welded metal and the electrolyte. This increases R_{ct} and leads to better corrosive resistance. The polarization test considers complex factors for the evaluation of corrosion properties, including the EIS response. For REE-containing welded metals, the R_p values are proportional to the second-phase particle sizes of the welded metals; see Figures 11(a) and 11(c). The R_p values are the opposite of the R_{ct} values. Welded metals with larger second-phase particles show higher R_p values. This can be due to the electric-potential increase of the second-phase particles containing REE. The REE content affects both sizes and ratios of the second-phase particles and the corrosion properties of HSLA welded metals as well as the mechanical properties.

The morphology of the welded metals after electrochemical testing is shown in Figure 12. Significant microcracks can be observed on the corrosive surface of the REE-free welded metal shown in Figure 12(a). The number of microcracks varies with the R_p values of the different REE-containing welded metals. No obvious microcracks were found on the corrosive surface of the REE1 sample; see Figure 12(b).

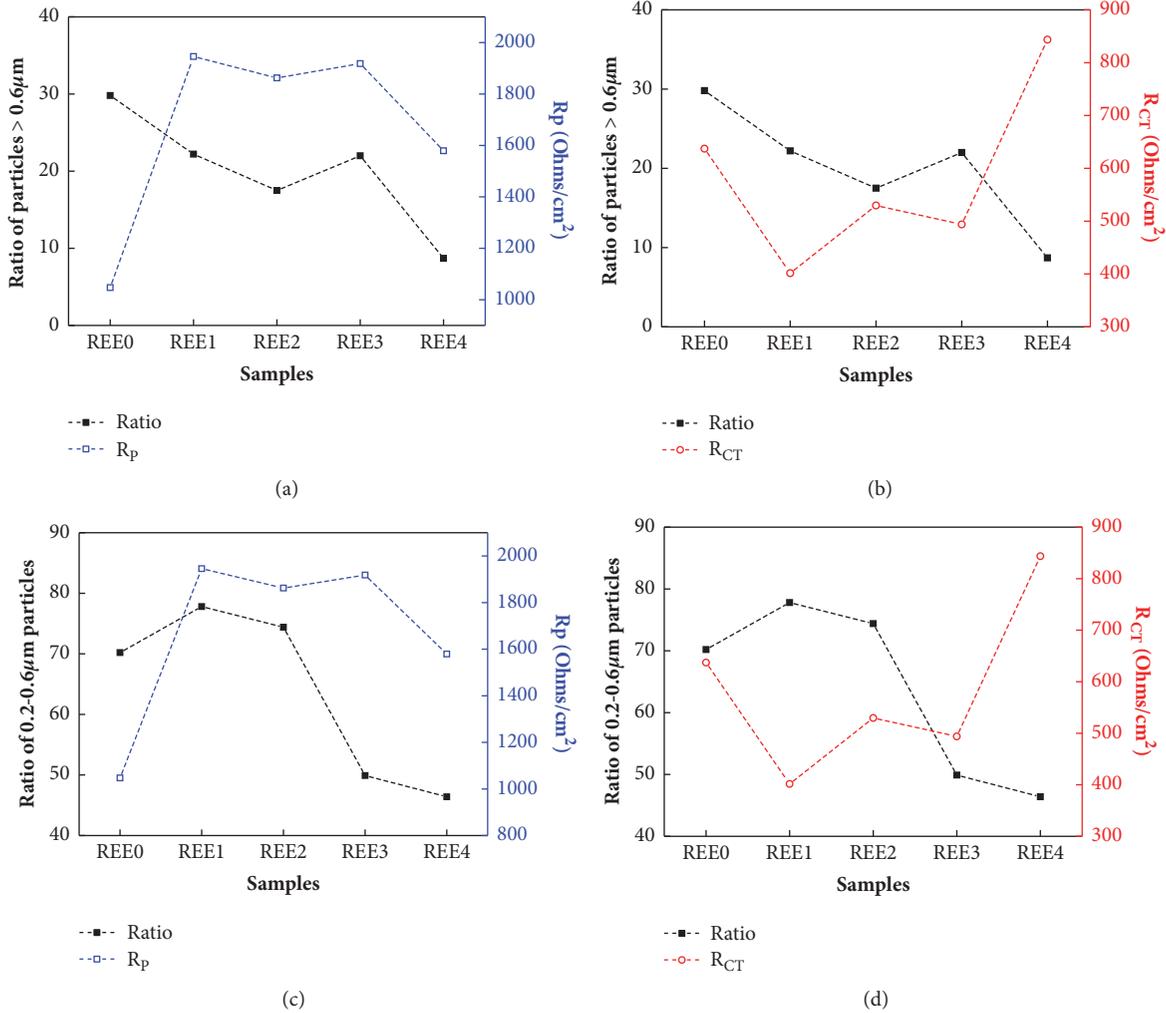


FIGURE 11: Correlation between second-phase particle sizes and the resistance in different welded metals.

However, microcracks REE can be seen clearly on the REE4 sample in Figure 12(e). During the electrochemical tests, the microcracks generated in the oxide films provide the channels for the electrolytes to infiltrate the oxide films. As a result, the charge-transfer process from the welded metal to the electrolyte accelerated. Both the REE-modified second-phase particles and microstructure of the welded metal facilitate the formation of dense oxide films thanks to the addition of REE.

For 10CrMo3NiV high-strength steel, the corrosion stability and the microstructure of the welded metal were significantly affected by the addition of REE, from the perspective of the effect on the size and ratio of second-phase particles. The result of the EIS tests and the potentiodynamic polarization curves indicates that the added REE in the flux-cored wire improves corrosion resistance in 10CrMo3NiV welded metals. To obtain detailed results of the second-phase particles affecting the electrochemical behavior of the welded metals, we plan to use scanning vibrating electrode technology (SVET) in further study. This will help reveal the underlying mechanism of

REE: how REE change for different corrosive times and electrolytes.

4. Conclusions

Rare-earth elements were added to the flux-cored wire to modify the performance of FCAW-welded metals with 10CrMo3NiV steel. Both OM and SEM studies indicate that the REE content changes the microstructure of welded metals by refining the second-phase particles. A content of 0.3 wt.% REE in the flux-cored wire is optimal to facilitate suitable second-phase particles in both the welded metal (0.2 μm to 0.6 μm in diameter) and the main acicular ferrite microstructure. This amount of REE also helps avoid the accumulation of nonmetallic elements and improves the mechanical properties of the welded metals. Both potentiodynamic polarization and EIS tests show that REE addition reduces the charge-transfer channel effect of the second-phase particles. Overall, the corrosion properties as well as the mechanical properties of a welded metal can be improved substantially by adding 0.3 wt.% REE.

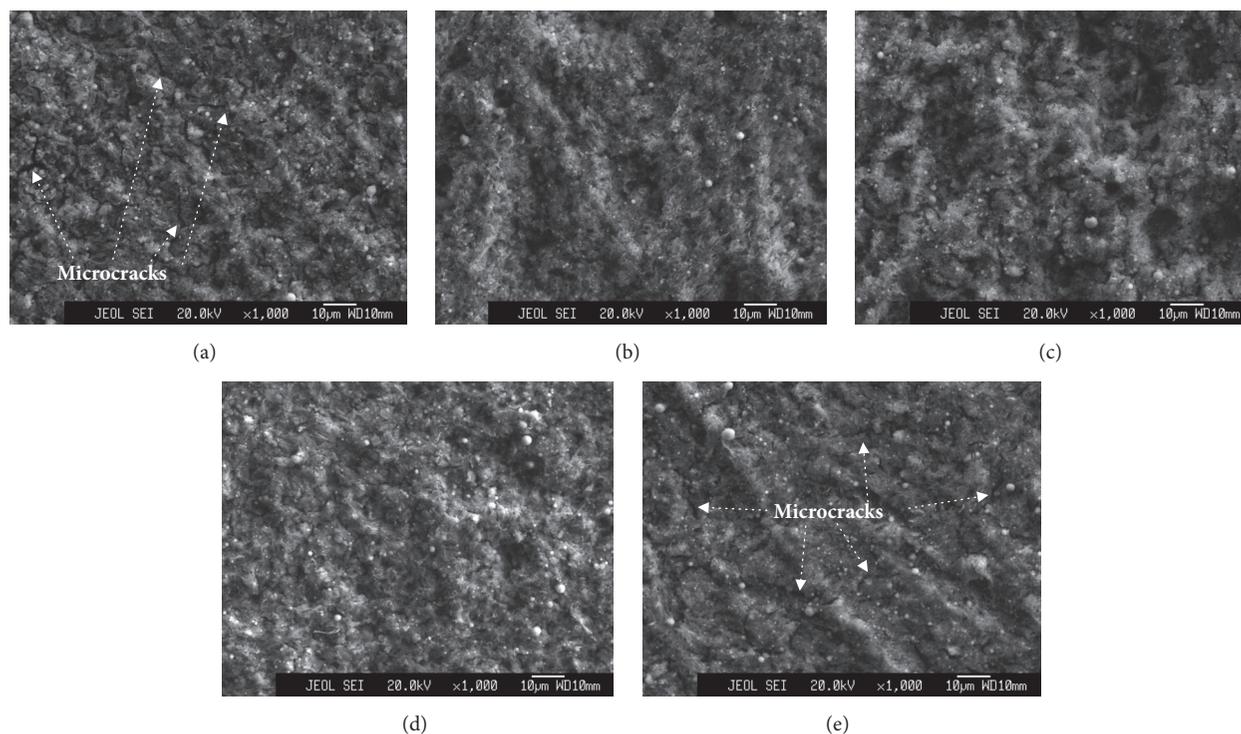


FIGURE 12: Morphology of the welded metals with different REE contents: (a) REE-free, (b) 0.3 wt.%, (c) 0.5 wt.%, (d) 0.7 wt.%, and (e) 1.0 wt.%, after electrochemical testing.

Conflicts of Interest

The authors declare that they have no conflicts of interest.

Acknowledgments

This research was supported by the National Natural Science Foundation of China (no. 51601043), the Scientific Program of GDAS (2016GDASPT-0205), the Technical Project of Guangdong and Guangzhou (201604046026, 2016B090918120, 201508030024, and 201704030112).

References

- [1] Committee on Effective Utilization of Weld Metal Yield Strength, *Effective Use of Weld Metal Yield Strength for HY Steels*, National Materials Advisory Board, Washington DC, Wash, USA, 1983.
- [2] J. H. Kim, J. S. Seo, H. J. Kim, H. S. Ryoo, K. H. Kim, and M. Y. Huh, "Effect of weld metal microstructures on cold crack susceptibility of FCAW weld metal," *Metals and Materials International*, vol. 14, no. 2, pp. 239–245, 2008.
- [3] Y.-W. Xu, S.-H. Song, and J.-W. Wang, "Effect of rare earth cerium on the creep properties of modified 9Cr-1Mo heat-resistant steel," *Materials Letters*, vol. 161, pp. 616–619, 2015.
- [4] J. Hufenbach, A. Helth, M.-H. Lee et al., "Effect of cerium addition on microstructure and mechanical properties of high-strength Fe85Cr4Mo8V2C1 cast steel," *Materials Science and Engineering: A Structural Materials: Properties, Microstructure and Processing*, vol. 674, pp. 366–374, 2016.
- [5] W. M. Garrison Jr. and J. L. Maloney, "Lanthanum additions and the toughness of ultra-high strength steels and the determination of appropriate lanthanum additions," *Materials Science and Engineering: A Structural Materials: Properties, Microstructure and Processing*, vol. 403, no. 1-2, pp. 299–310, 2005.
- [6] H.-L. Liu, C.-J. Liu, and M.-F. Jiang, "Effect of rare earths on impact toughness of a low-carbon steel," *Materials and Corrosion*, vol. 33, no. 1, pp. 306–312, 2012.
- [7] G. Liu, G. Zhang, and R. Li, "Electronic theoretical study of the interaction between rare earth elements and impurities at grain boundaries in steel," *Journal of Rare Earths*, vol. 21, no. 3, pp. 372–374, 2003.
- [8] D. Zhang, C. Wu, and R. Yang, "Interaction between cerium and phosphorus segregating in the grain boundaries in α -Fe studied by computer modelling and Auger electron spectroscopy," *Materials Science and Engineering: A Structural Materials: Properties, Microstructure and Processing*, vol. 131, no. 1, pp. 93–97, 1991.
- [9] S. Song, H. Sun, and M. Wang, "Effect of rare earth cerium on brittleness of simulated welding heat-affected zones in a reactor pressure vessel steel," *Journal of Rare Earths*, vol. 33, no. 11, pp. 1204–1211, 2015.
- [10] X. Jiang and S.-H. Song, "Enhanced hot ductility of a Cr-Mo low alloy steel by rare earth cerium," *Materials Science and Engineering: A Structural Materials: Properties, Microstructure and Processing*, vol. 613, pp. 171–177, 2014.
- [11] L. Chen, X. Ma, M. Jin, J. Wang, H. Long, and T. Mao, "Beneficial Effect of Microalloyed Rare Earth on S Segregation in High-Purity Duplex Stainless Steel," *Metallurgical and Materials Transactions A: Physical Metallurgy and Materials Science*, vol. 47, no. 1, pp. 33–38, 2016.

- [12] Y. Tomita, "Improved fracture toughness of ultrahigh strength steel through control of non-metallic inclusions," *Journal of Materials Science*, vol. 28, no. 4, pp. 853–859, 1993.
- [13] J. Gao, P. Fu, H. Liu, and D. Li, "Effects of rare earth on the microstructure and impact toughness of H13 steel," *Metals*, vol. 5, no. 1, pp. 383–394, 2015.
- [14] J. Pu, S. Yu, and Y. Li, "Role of inclusions in flux aided backing submerged arc welding," *Journal of Materials Processing Technology*, vol. 240, pp. 145–153, 2017.
- [15] N. Yan, S. F. Yu, and Y. Chen, "Inclusions, microstructure and properties of flux copper backing submerged arc weld metal," *Science and Technology of Welding and Joining*, vol. 20, no. 5, pp. 418–424, 2015.
- [16] B. Hinton, "Corrosion inhibition with rare earth metal salts," *Journal of Alloys Compounds*, vol. 180, pp. 15–25, 1992.
- [17] C. Wang, F. Jiang, and F. Wang, "The characterization and corrosion resistance of cerium chemical conversion coatings for 304 stainless steel," *Corrosion Science*, vol. 46, no. 1, pp. 75–89, 2004.
- [18] E. Gharibshahiyan, A. H. Raouf, N. Parvin, and M. Rahimian, "The effect of microstructure on hardness and toughness of low carbon welded steel using inert gas welding," *Materials and Corrosion*, vol. 32, no. 4, pp. 2042–2048, 2011.
- [19] C. Zhang, X. Song, P. Lu, and X. Hu, "Effect of microstructure on mechanical properties in weld-repaired high strength low alloy steel," *Materials and Corrosion*, vol. 36, pp. 233–242, 2012.
- [20] B. Basu and R. Raman, "Microstructural variations in a high-strength structural steel weld under isoheat input conditions," *Welding Journal (Miami, Fla)*, vol. 81, no. 11, 2002.
- [21] G. Spanos, R. W. Fonda, R. A. Vandermeer, and A. Matuszeski, "Microstructural changes in HSLA-100 steel thermally cycled to simulate the heat-affected zone during welding," *Metallurgical and Materials Transactions A: Physical Metallurgy and Materials Science*, vol. 26, no. 12, pp. 3277–3293, 1995.
- [22] Y. Cai, R. Liu, Y. Wei, and Z. Cheng, "Influence of Y on microstructures and mechanical properties of high strength steel weld metal," *Materials & Design (1980-2015)*, vol. 62, pp. 83–90, 2014.
- [23] T. Koseki and G. Thewlis, "Inclusion assisted microstructure control in C-Mn and low alloy steel welds," *Materials Science and Technology*, vol. 21, no. 8, pp. 867–879, 2005.
- [24] C. A. Williams, P. Unifantowicz, N. Baluc, G. D. W. Smith, and E. A. Marquis, "The formation and evolution of oxide particles in oxide-dispersion-strengthened ferritic steels during processing," *Acta Materialia*, vol. 61, no. 6, pp. 2219–2235, 2013.
- [25] R. A. Ricks, P. R. Howell, and G. S. Barritte, "The nature of acicular ferrite in HSLA steel weld metals," *Journal of Materials Science*, vol. 17, no. 3, pp. 732–740, 1982.
- [26] R. M. Fernández-Domene, E. Blasco-Tamarit, D. M. García-García, and J. García-Antón, "Effect of alloying elements on the electronic properties of thin passive films formed on carbon steel, ferritic and austenitic stainless steels in a highly concentrated LiBr solution," *Thin Solid Films*, vol. 558, pp. 252–258, 2014.
- [27] Y. Chen, T. Hong, M. Gopal, and W. P. Jepson, "EIS studies of a corrosion inhibitor behavior under multiphase flow conditions," *Corrosion Science*, vol. 42, no. 6, pp. 979–990, 2000.
- [28] G. A. Zhang and Y. F. Cheng, "Corrosion of X65 steel in CO₂-saturated oilfield formation water in the absence and presence of acetic acid," *Corrosion Science*, vol. 51, no. 8, pp. 1589–1595, 2009.
- [29] H.-Y. Ha, M.-H. Jang, T.-H. Lee, and J. Moon, "Interpretation of the relation between ferrite fraction and pitting corrosion resistance of commercial 2205 duplex stainless steel," *Corrosion Science*, vol. 89, no. C, pp. 154–162, 2014.
- [30] D. H. Kang and H. W. Lee, "Study of the correlation between pitting corrosion and the component ratio of the dual phase in duplex stainless steel welds," *Corrosion Science*, vol. 74, pp. 396–407, 2013.

Research Article

The Analysis of the Influence of Various Factors on the Development of Stress Corrosion Defects in the Main Gas Pipeline Walls in the Conditions of the European Part of the Russian Federation

A.V. Afanasyev,¹ A. A. Mel'nikov,¹ S. V. Konovalov ,^{1,2} and M. I. Vaskov³

¹Samara National Research University, 34 Moskovskoye Shosse, Samara 443086, Russia

²Wuhan Textile University, 1 Fang Zhi Road, Wuhan 430073, China

³"Gazprom Transgaz Samara" LLC, 106a Novo-Sadovaya Str., Samara 443086, Russia

Correspondence should be addressed to S. V. Konovalov; ksv@ssau.ru

Received 20 December 2017; Revised 17 April 2018; Accepted 2 May 2018; Published 3 June 2018

Academic Editor: Jerzy A. Szpunar

Copyright © 2018 A.V. Afanasyev et al. This is an open access article distributed under the Creative Commons Attribution License, which permits unrestricted use, distribution, and reproduction in any medium, provided the original work is properly cited.

This paper considers the factors influencing the formation and development of stress corrosion defects detected during the inspection and overhaul of the main gas pipeline section. The surveyed gas pipeline is made of large diameter steel pipes made by controlled rolling, produced by various companies, with the predominance of pipes produced by the Khartsyzsk Pipe Plant (KhPP). The correlation between the geometric parameters of defects is described, which makes it possible to estimate the depth of cracks by external parameters. Mechanical tests by cyclic loading of samples containing cracks, based on the site operation data for the last 11 years, showed no crack growth in the absence of a corrosive medium. Micro-X-ray spectral analysis of metal and corrosion products showed no trace of the influence of hydrogen sulphide and nonmetallic inclusions (sulphides) on the development process of SCC. According to the results of the research, the process of development of stress corrosion on the main gas pipelines located in the European part of the Russian Federation is described. The organization operating the gas pipeline is recommended to take into consideration the results of this work during drawing up their repair plan.

1. Introduction

To date, more than a third (36%) of accidents occur on the main gas pipelines (MG) of the Unified Gas Supply System (UGSS) belonging to «Gazprom» PJSC as a result of the development of stress corrosion defects or stress corrosion (hereinafter referred to as SCC). In the world practice of transporting natural gas through pipelines, this type of damage has the highest specific gravity among all other causes of accidents; therefore, during diagnostic examinations this type of defects is given the highest priority [1–3]. At the same time, along with the improvement of diagnostic tools, the number of newly detected CTC defects on UGS facilities is growing every year. If earlier, about 2,000 CWN defects were detected per year by methods of in-tube flaw detection (ILI) by magnetic shells; now with the use of electromagnetic-acoustic

projectiles (EMA) this figure reaches 10,000 defects per year [4]. A large number of SCC defects are revealed by methods of nondestructive testing (NDT) in pits and during major overhauls. The absolute majority of defects detected by all inspection methods (almost 92%) have a measured depth of less than 10% of the wall thickness [5, 6]. According to experts, SCC crack of different depths was identified or is more likely to be detected in more than a million pipe sections during the next surveys [7–9]. This statement is consistent with the current trend to increase the number of small defects found.

The repair by replacing even a small part of these pipes will lead to a reduction in the total volume of UGSS pipeline overhaul due to the specific increase in the individual sections repair cost [10–12]. At the same time, the degree of defects' danger, the depth of which is less than 10–15% of the wall



FIGURE 1: Investigated pipeline section.

thickness, under condition that access of corrosive medium to them is restricted, is determined by many researchers as insignificant [13–16]. At the present time, there are methods of repairing the pipelines polymer insulation, which do not allow the cracks to develop and threaten the reliability of pipelines for a long time [17, 18]. However, methods for an accurate assessment of the SCC cracks depth are not developed, and the factors that influence the distribution of SCC defects in extended sections are not always considered systematically during major overhauls.

Thus, the development of systematic methods of combating negative manifestations of stress corrosion in the form of accidents (identification, assessment, and targeted removal of only those defects that may lead to an accident in the foreseeable future with account of repair of insulation on other defects) is an urgent task.

The purpose of this study is to determine the factors that affect the distribution of SCC defects and the rate of their development during the main gas pipelines operation period. The second goal is to determine the parameters by which the depth of cracks can be estimated.

2. Materials and Methods

2.1. Field Studies on the Gas Pipeline Extended Section. For detailed consideration of operational factors and sampling, a section of main gas pipeline located in the eastern part of the European part of the Russian Federation with a length of 25 km was selected (Figure 1).

The selection criteria for the site were the presence of pipes of various types and the possibility of subsequent objective control of their technical condition. It was planned to evaluate the cyclicity over a long period of operation and compare the data of the ILI and the rejection results obtained during upcoming major overhaul (100% NDT of the pipe surface). In addition, a comparison of the electrometric and physical profile of the section with a real distribution of SCC defects was carried out.

2.2. Estimation of Cracks Depth by Their External Manifestations. To create a mechanism for estimating the depth of SCC cracks using direct measurements of their geometric parameters, 15 samples were made from the rejected pipes, and 157 cracks were selected and described on these samples (Figure 2).

The surface of the samples was polished, the largest cracks in the colony were selected, and their length and width were measured. After that, the sample was cut and the depth of the cracks was directly measured on the cross section.

2.3. Cyclic Tests with a Load Similar to the Operational Load. To determine the effect of cyclic loading on the development of SCC defects under operating conditions with the excluded access of the corrosive medium to cracks, cyclic tests of 4 model samples were carried out under four-point loading conditions with accordance to the accepted industry method [19]. To justify the choice of cyclic test modes, the whole range of pressure fluctuations over a period of 11 years of operation was constructed based on the data from the operating modes log for selected pipeline section. The average value of the pressure (P_{av}) was defined as 5.84 MPa and the cycles with the greatest pressure deviations were identified. During the selected period, the pipeline section experienced 18 cycles of loading and unloading with the maximum deviation from the P_{av} in the range of 17–35%.

In the full spectrum of oscillations, a time interval (T) was determined, inside which the upper and lower half-periods were analyzed. In these half-cycles, the cycles with the greatest amplitude deviations from P_{av} , equal to $2 \pm 11\%$ of the working pressure (P_w), were identified. The parameters of the cyclic pressure change processes in each half-period (P_{cpc}) were calculated (Figure 3). Based on the analysis of operating conditions of the investigated section of the main gas pipeline, it was found that the total number of pressure drop cycles within one year could be divided into two parts: 30 pulsation cycles with an amplitude in the range of $2 \pm 11\%$ of P_w and 2 major cycles with an amplitude in the range of 17–35% of P_w .

As a result of the analysis the most conservative loading regime was chosen for the testing of model samples, which simulated the work of main gas pipeline for 20 years of operation in real conditions. The load variation interval varied from 1.1 MPa to 7.4 MPa (the maximum working pressure allowed on the pipeline section), which is characterized by the asymmetry coefficient of the cycle ($R = 0.15$). The total number of cycles was calculated as the total number of all types of cycles affecting the gas pipeline for the year, multiplied by the planned interval of operation, equal to 20 years. Thus, the loading mode of the model samples was carried out in three stages with a change in the load every 640 cycles. The tests were carried out on a tensile machine using a four-point loading scheme (Figure 4).

To monitor the state of stress corrosion cracks, one control crack was selected on each sample, the photographic images of which were recorded with a metallographic microscope before the start of the tests, after the second stage, and at the end of the third stage of the test. The control was carried out relative to the initial state programmatically by measuring the number of pixels in the image along the line connecting the beginning and end of the crack.

2.4. Electron Microscopy. Cracks, cuts, and open corrosion cracks were studied by electron microscopy and micro-X-ray spectral analysis. In the course of the study, micro-X-ray spectral analysis of the elemental composition of corrosion

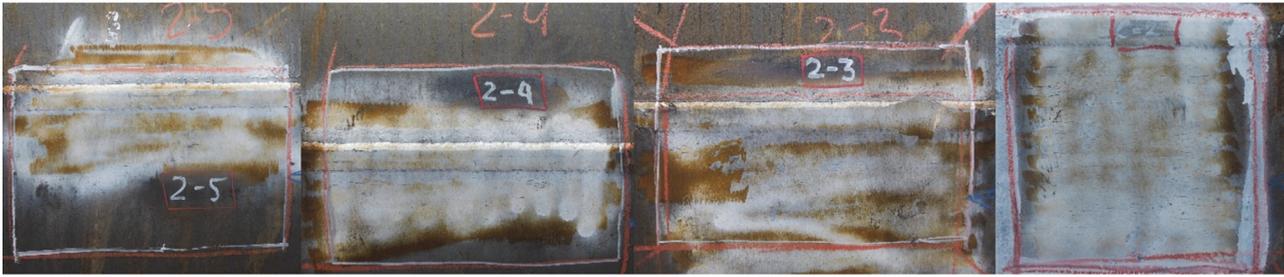


FIGURE 2: Samples with SCC cracks.

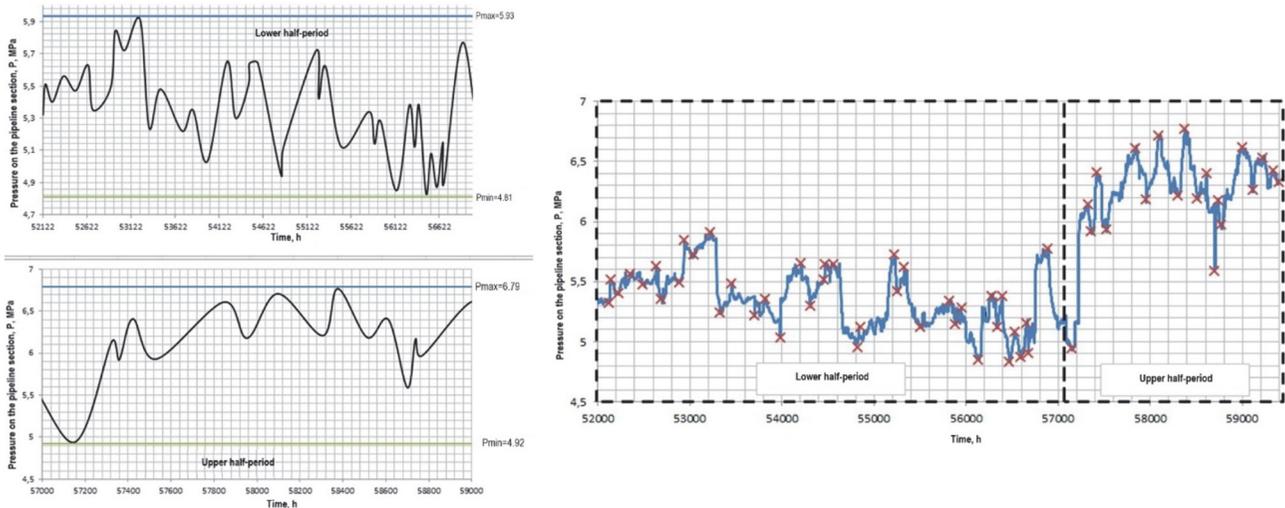


FIGURE 3: The upper and lower half-cycles of the oscillations in the chosen time interval (T).

products was carried out, and surface maps of the distribution of elements along the surface of destruction were made.

The fractographic and microscopic analysis of the crack surface was carried out on a TESCAN scanning electron microscope with VEGA software at magnifications up to 4000 times [19].

Spectral analysis to determine the quantitative chemical composition of the elements was carried out using the OXFORD INCAx-act energy dispersing attachment in accordance with ISO 15632: 2002.

Identification of the fracture behaviour by the type of surface relief was carried out in accordance with [20].

The general view of the TESCAN VEGA SBH Easy Probe scanning electron microscope and the OXFORD INCAx-act energy dispersing attachment is shown in Figure 5.

3. Results and Discussion

The density of the SCC defect distribution detected by the NDT during the overhaul was more than 97 times higher than expected by the results of the ILI. The average density of SCC defects on single-seam pipes (imported) is 50 times less than on double-seam pipes produced at Khartsyzsk Pipe Plant (KhPP). It was noted that stress corrosion damage localized mainly near the longitudinal weld. SCC defects of maximum

depth (up to 36% of the wall thickness) were also found on the KhPP pipes.

The density of the distribution of SCC defects correlates with the number of KhPP pipes in the pipeline layout. At the same time, the noted characteristics of the external environment, as the value of the electrical resistance of the soil and the height differences along the section profile, do not significantly affect the distribution of defects. (Figure 6)

During the overhaul, more than 13.5 km of pipes were rejected on the site, more than 11.5 km (more than 85%) of them due to SCC defects. In total, more than 58% of all the double-seam KhPP pipes inspected at the 25-kilometer section were rejected due to SCC defects. For single-seam pipes, including imported pipes, the rejection rate due to SCC was only 7%.

The majority of defects detected during NDT (more than 92%) have a depth of less than 10% of the wall thickness, which is below the detection threshold of magnetic in-tube flaw detectors. Therefore, undetected SCC defects can be present on other sections of the pipeline, and inspection with more sophisticated in-tube flaw detectors or NDT inspections in pits (for example, during the overhaul by re-insulation) will most likely reveal them.

During the research, it was established that there is a dependence between the main external parameters of SCC

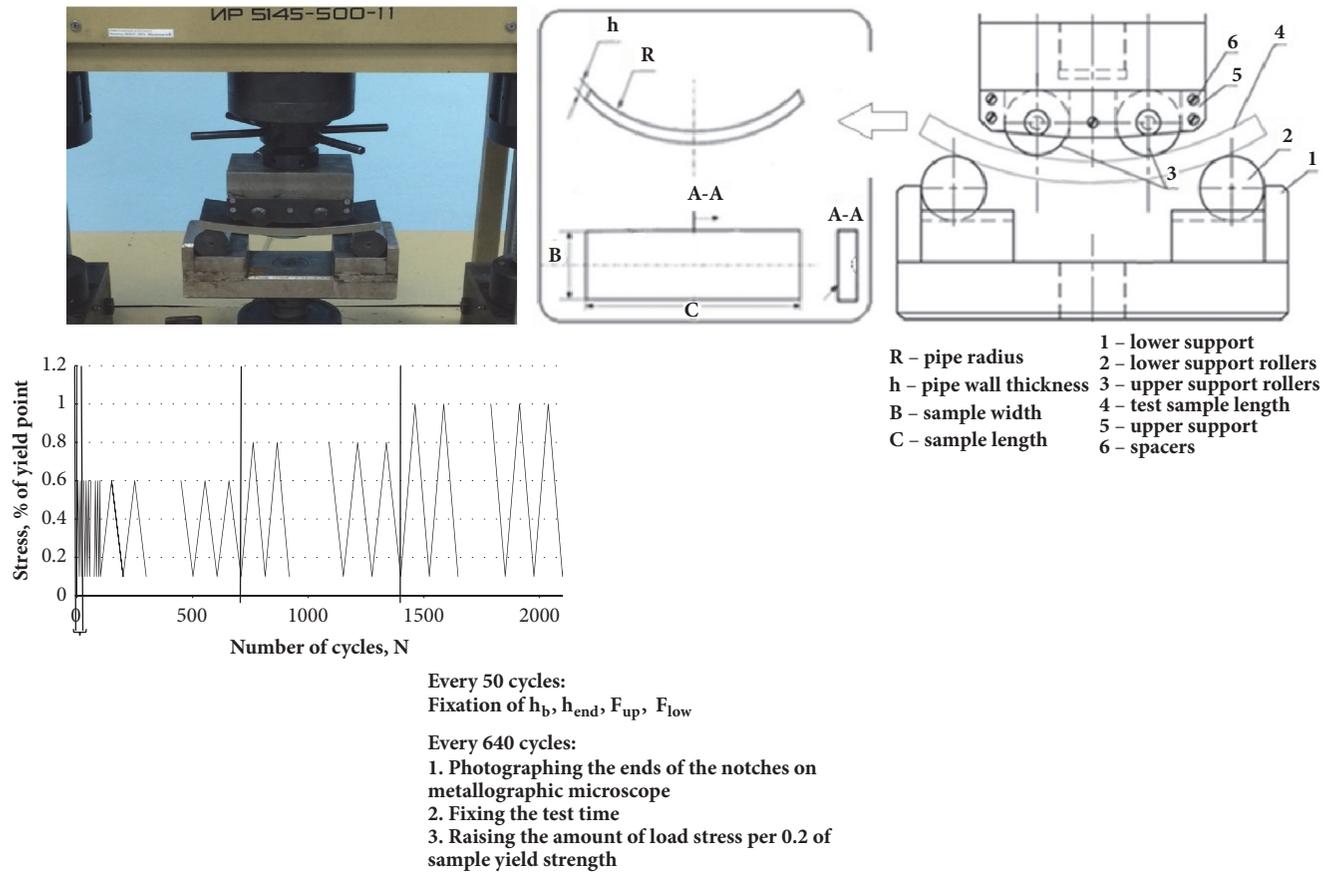


FIGURE 4: Cyclic testing of samples according to the four-point loading scheme.



FIGURE 5: General view of the TESCAN VEGA SBH Easy Probe scanning electron microscope.

cracks. The crack length-to-width ratio was 10:1 and the width-to-depth ratio was 0.06: 1. Thus, at a depth of 1-1.5 mm, the opening width is 0.06 mm; with a depth of 2-2.5 mm, the opening width is 0.12 mm (Figures 7(a) and 7(b)).

Measurement of the crack opening width was carried out using a measuring magnifier with an accuracy of ± 0.01 mm. In this case, the absolute limit error for the two measurements was ± 0.016 mm and the relative errors for each of the

measurements were $\delta 1 = 28\%$ (section A) and $\delta 2 = 24\%$ (section B), respectively.

After carrying out the cyclic tests, which were controlled by the metallographic method (Figures 8 and 9), it was found that, in the absence of a corrosive environment, the stress corrosion crack retained its original state after all the test stages. During the tests, no formation of new cracks-branches and other changes in the morphology of the crack apex was recorded. Thus, during the three stages of testing cycles simulating the operation of the real pipeline section (load-unload cycles), the development of existing stress corrosion cracks has not occurred (Figure 9).

Ten cracks were opened out by excessive force in order to study the resulting fracture. Analysis of the fracture surface at small magnifications showed that the upper part of the crack is completely filled with oxides. The soil brine constantly permeated and oxidized the internal surface of the crack during the operation life of the pipeline. The oxides formed also wedged and deformed the inner surface. Micro-X-ray spectral analysis of the elemental composition of corrosion products also showed that the cracks are completely filled with oxide. The distribution of various elements along the fracture surface is represented on the distribution maps of the elements (Figure 10).

As it can be seen from the distribution maps of the elements, there are no obvious phase boundaries. Corrosion

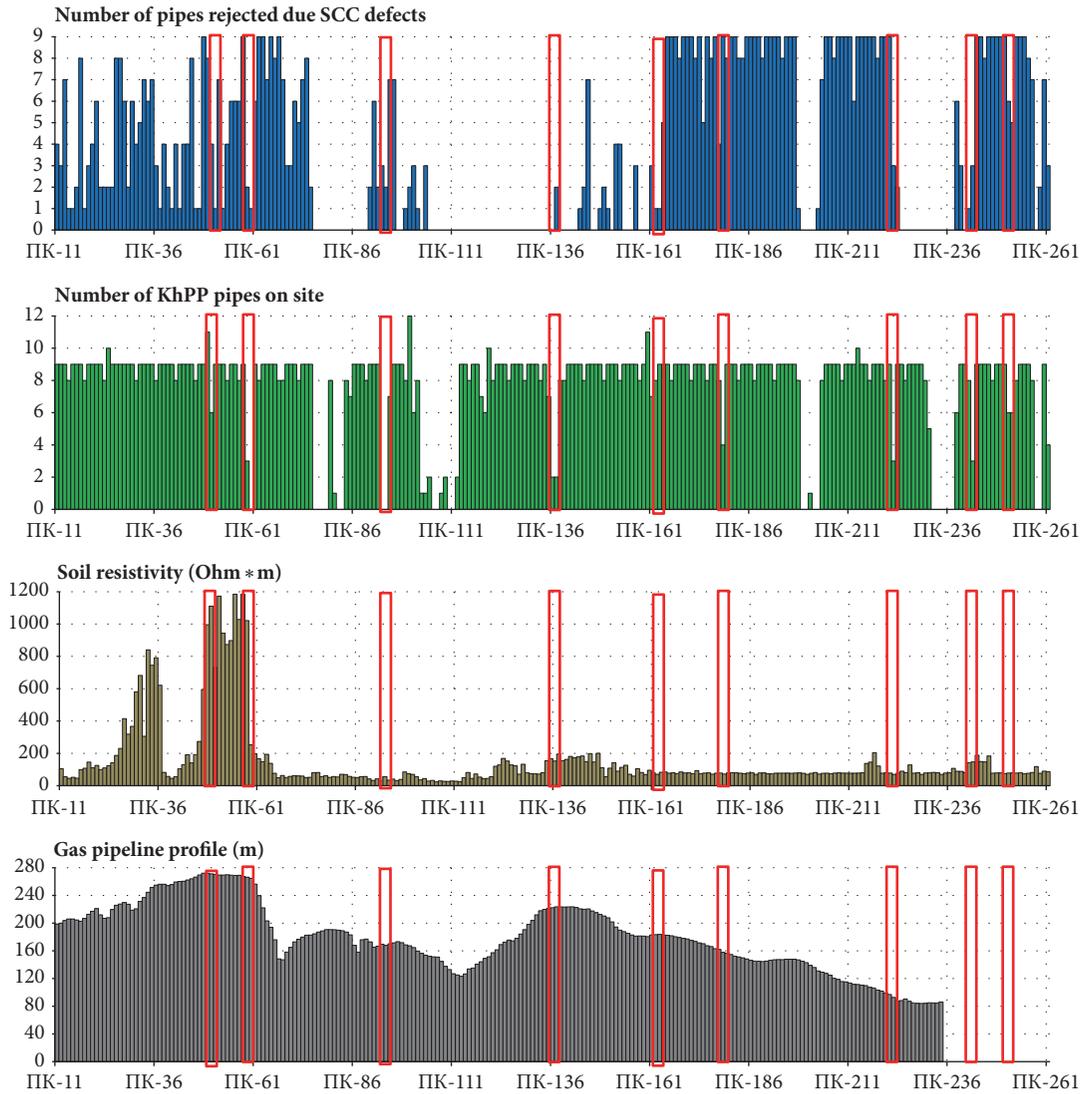


FIGURE 6: Number of pipes with SCC defects, number of KhPP pipes, soil characteristics, and section profile. The X-axis indicates the distance along the pipeline route. Pipeline sections with a small number of pipes produced by KhPP are marked in red.

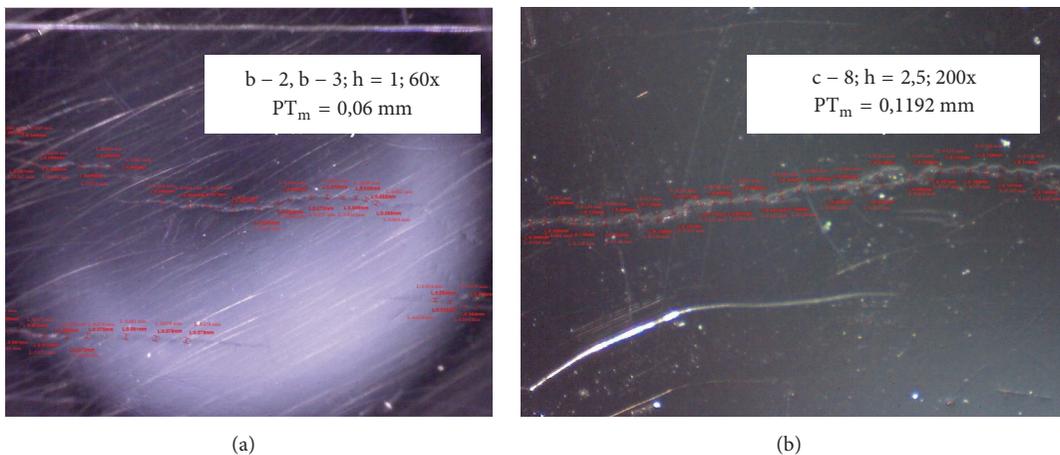
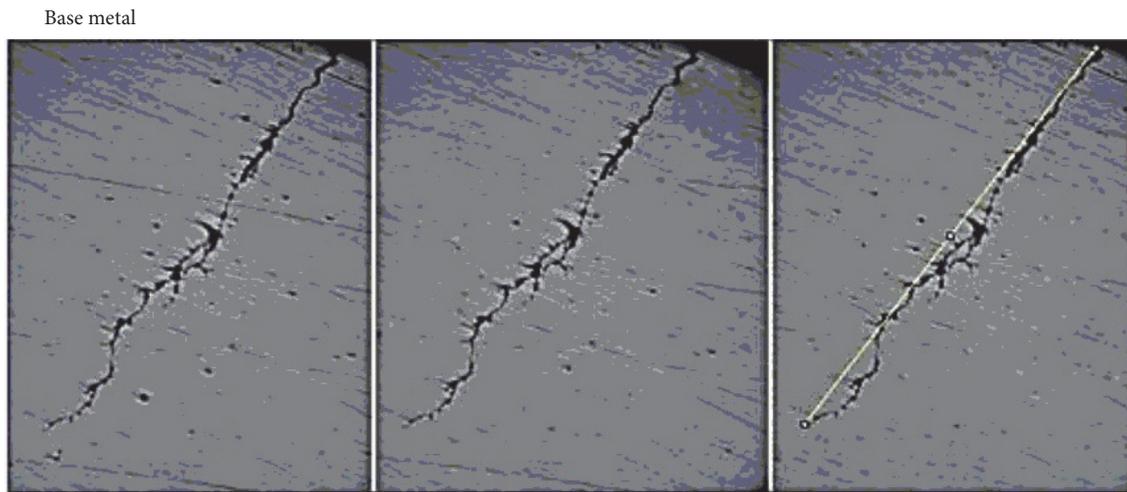


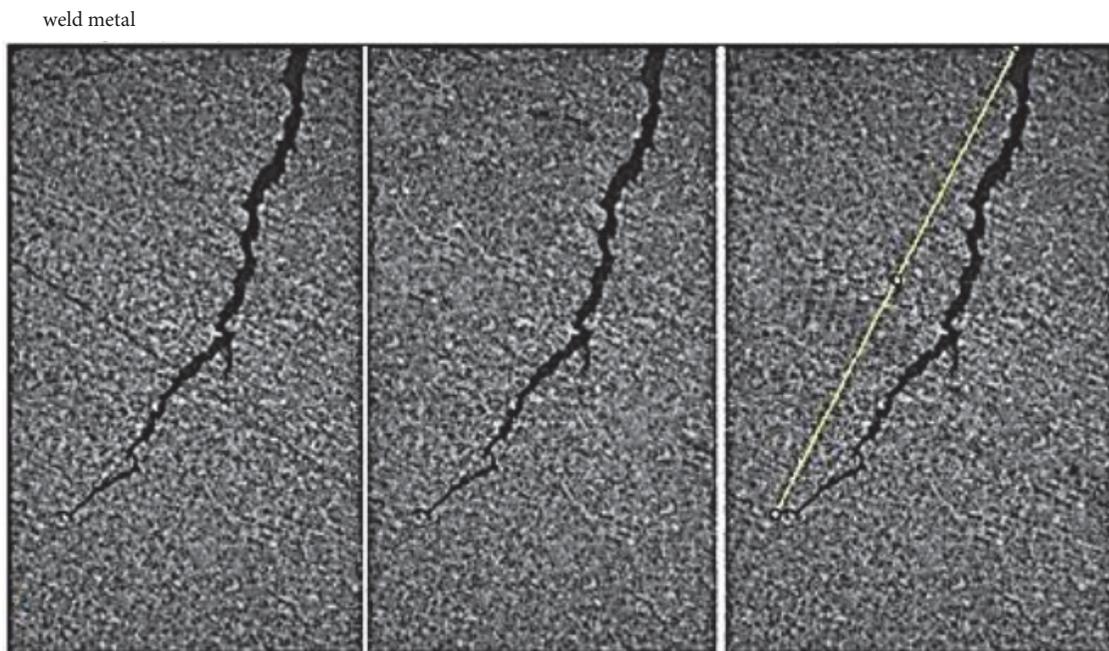
FIGURE 7: Microscopic examination of cracked sections.



Results

| | Mean | Angle | Length |
|---|---------|----------|---------|
| 1 | 166.487 | -127.035 | 347.001 |
| 2 | 110.040 | -127.569 | 344.426 |
| 3 | 113.190 | -127.730 | 346.439 |

FIGURE 8: Results of crack depth stepwise measurement in the base metal of model sample.



Results

| | Mean | Angle | Length |
|---|---------|----------|---------|
| 1 | 106.151 | -117.282 | 286.021 |
| 2 | 104.792 | -117.196 | 284890 |
| 3 | 105.432 | -117.375 | 285118 |

FIGURE 9: Results of crack depth stepwise measurement in the model sample with longitudinal weld section.

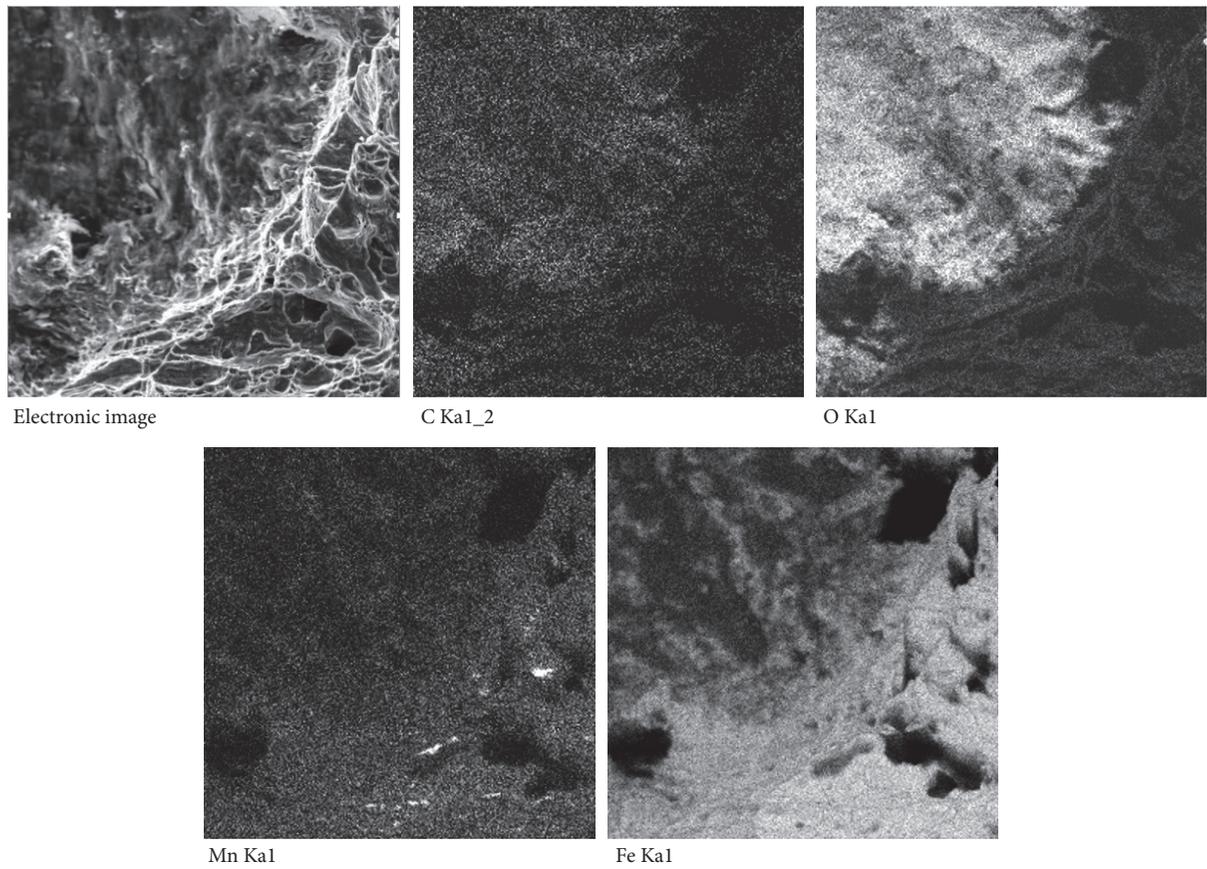


FIGURE 10: Elements distribution maps.

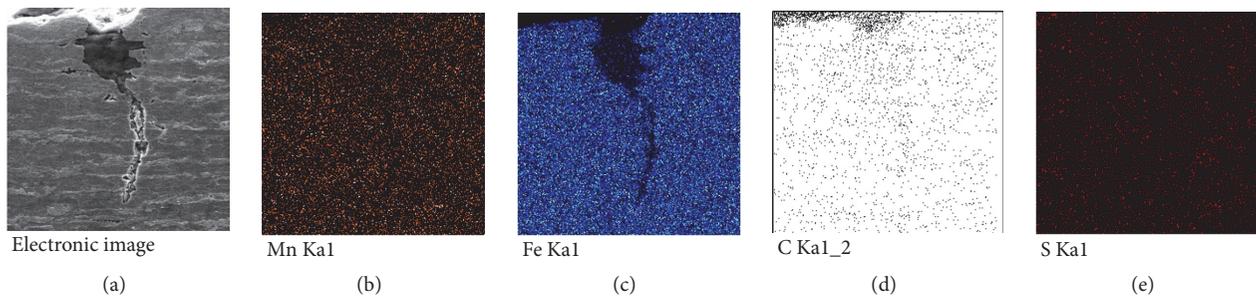


FIGURE 11: Maps of elements distribution in a stress corrosion crack: (a) electronic image of the crack; (b) distribution of manganese; (c) distribution of iron; (d) distribution of carbon; (e) distribution of sulfur.

products are evenly distributed inside the crack. The images in the iron, oxygen, and carbon spectra are homogeneous and equally bright, indicating either a monophasic break in the oxide or even mixture of several phases. The expected composition of corrosion products is either a homogeneous Fe_2O_3 or a mixture of Fe_2O_3 and FeCO_3 .

To determine the effect of metallurgical impurities and additives on the development of cracks, the surface of the sections was also mapped in the spectra of sulfur and manganese. Due to limitations of the method, spectrometric data were not used to quantify the ratio of oxygen and carbon in corrosion products and in the base metal. During the

mapping process, the main goal was to identify points with a local increased content of individual chemical elements corresponding to nonmetallic inclusions, their subsequent detailed analysis in case of revealing their influence on the process of material destruction, and subsequent detailed analysis of such points in case of revealing their influence on the process of material destruction.

The maps show an image of cracks in the samples in the spectra of iron, oxygen, carbon, sulfur, and manganese (Figure 11). An increased sulfur content in corrosion products was not observed, as evidenced by the different brightness of the elements spectrum image in the transition from the base

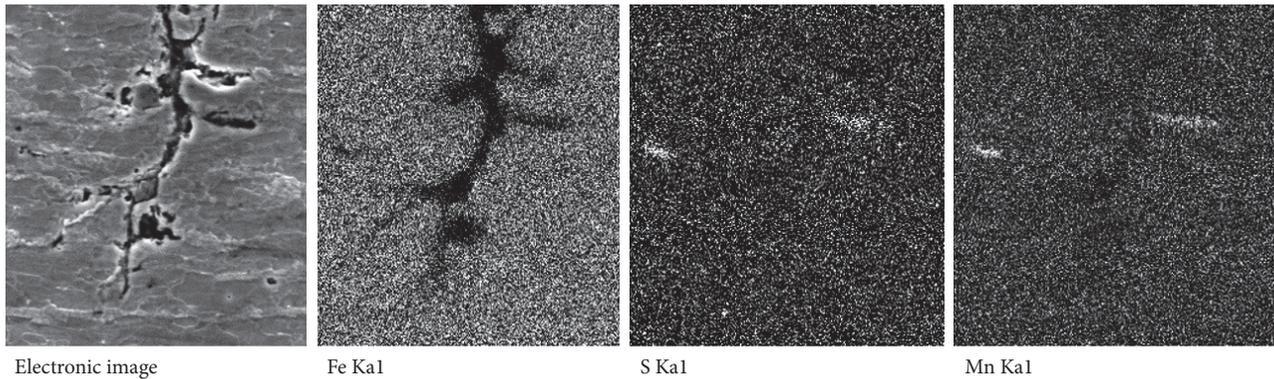


FIGURE 12: Maps of elements distribution in a stress corrosion crack. Increased local sulfur content (manganese sulphide).

metal to the crack. A reduced content of iron and manganese and a high content of oxygen and carbon in the products of corrosion were noted (Figure 11).

The sulfur content in the corrosion products does not exceed the sulfur content in the base metal. Images in the spectra of manganese and sulfur are homogeneous and equally bright both in the cross section of the base metal and in the section of the crack. In some samples, a lower sulfur content can be noted with the exception of some local points (Figure 12).

Thus, the coincidence of the increased concentration of manganese and sulfur in some sections of the map indicates the presence of sulphide nonmetallic inclusion. As seen in the electronic image, these nonmetallic inclusions are not the sources of development of destruction. In the remaining volume of the crack, the sulfur content does not exceed the sulfur content of the metal, and the total contamination of the material with sulfur does not go beyond technical specifications.

Based on the data obtained as a result of the research, it is possible to assume a scenario for the development of SCC defects in the main gas pipeline.

During the construction of the pipeline, film insulation materials with on-site application were used, which during the period of operation lost their necessary technological properties. This is reflected in the fact that, during the operation of the pipeline, corrugations and pockets appeared in some places on the insulation coating. Corrosion-active soil electrolyte penetrated damaged insulation areas.

Later, these corrosion pits continued their growth and became concentrators of mechanical stresses in the pipeline wall. The source of these stresses were constant pressure pulsations from operating gas pumping units and gas temperature fluctuations due to the nonstationary operation of the gas compressor station.

The first microdeformations appeared, leading to the appearance of sharp cracks. Further, the cracks developed irregularly, under the influence of operational loads. In the development of the defect, a continuous process of corrosion was of decisive importance, stimulated by a constant inflow of heat along with the transported medium. The soil brine continued to penetrate into the cracks, wash out corrosion

products, and deliver portions of the new electrolyte to the crack vertex.

Analysis of the effectiveness of various methods of non-destructive testing has shown that a colony of cracks can be identified by all available mass methods used in the oil and gas industry. However, in order to improve the efficiency of SCC defect detection, it is necessary to take into account and track factors that increase the predisposition of sites to this type of destruction.

The morphology of the detected defects corresponds to modern concepts of SCC defects. Defects are identified as cracks on the bottom of corrosive pits. They are grouped in colonies, oriented along the axis of the tube during their growth and branch along the section with the tendency to merge with one another.

The effect of sulfur and its compounds on the process of stress corrosion is not a significant factor, as there was no increased sulfur content in corrosion products. The phase composition of the corrosion products within the cracks is homogeneous across the crack cross section. The phase boundaries and the sections, which differ sharply in chemical composition, were not found.

Traces of the predominant effect of impurities and non-metallic inclusions were not found. The structure of the metal is homogeneous and corresponds to the structure of rolled metal.

It was found that there is a consistent pattern between the width of the opening and the length of the crack. A simple statistical generalization showed that the length-to-width ratio could be described as 10:1 and the width-to-depth ratio as 0.06:1. Since the majority of SCC cracks in the investigated samples are the same in origin, size, and morphology, it can be said that such a regularity exists in this particular case of SCC.

The appearance of cracks can be influenced by a variety of technological factors, laid down at various stages of the life cycle of the product. Such a factor can be the contamination of the pipe metal by harmful impurities and the presence of residual stresses in the pipe wall after and during manufacture at the stage of pipe production. In addition, these factors can include increased values of stresses in the pipeline wall, which arose due to flaws in construction design and installation

work at the pipeline construction stage. This includes the nonprojected position of the pipe in the trench, unplanned soil movements, and welding stresses. The nonstationary operation mode of the pipeline also has a great influence, namely, the constant pulsation of the pressure and temperature of the pumped medium. Equally important is the corrosive activity of the ground in contact with the pipeline and the quality of the anticorrosive insulation at the stage of gas pipeline operation period.

Film insulation with on-site application does not provide long-term protection of the pipe body from SCC defects. After several years, due to soil movement and degradation of the coating, corrugations and pockets are formed in it, which collect soil moisture. Such conditions create a favorable environment for the development of corrosion defects. In the future, under the influence of these conditions and in the presence of an appropriate stress state, SCC defects can form. The insulation coatings used in newly constructed and repaired pipelines must provide long-term reliable protection of the pipe body against the corrosive effects of the environment in the operating conditions of main gas pipelines.

The main factor that can be detected and affects the distribution of stress corrosion, with other factors being equal, are the technological features of the pipe materials embedded in the product during its production stage. Presumably, this is the degree of local plastic deformation and the number of transitions during the formation of the pipe and sheet material and the thermal and high-speed welding of the longitudinal seam of two-seam pipes. To confirm this assumption, it is necessary to assess the residual stresses on the wall of the affected pipe and draw a map of them.

The presence of a corrosive medium is a prerequisite for the destruction of the pipeline wall due to the development of a SCC defect.

4. Confirmations

The presence of empirical dependence should be verified on a large statistical sample. Also, it is necessary to connect the external manifestations of SCC (the length of cracks and their opening) with the depth of stress corrosion damage. If such a relationship is confirmed in other cases of SCC, then it will be possible to describe the growth of a crack and the rate of its propagation in the general case with the sufficient accuracy. It will also be possible to build a mathematical model of the crack and calculate the residual life cycle of the pipeline using the finite element method.

Such an approach will make it safer to reuse the KhPP double-seam pipes during major overhaul, which is allowed only after a comprehensive evaluation of each pipe. In determining the degree of danger of each specific defect, a methodology for estimating the static strength of gas main pipeline with colonies of corrosion cracks is tested and used in "Gazprom transgaz Samara" LLC [21]. If, in addition to the nondestructive testing methods used in the survey, the external crack parameters are used and the calculation is performed using the largest depth obtained by different methods, then the assessment of the SCC crack danger will become more accurate.

The organization operating the gas pipeline is recommended to take into consideration the results of this work during drawing up their repair plan.

Conflicts of Interest

The authors declare that there are no conflicts of interest regarding the publication of this paper.

References

- [1] S. V. Alimov, A. B. Arabej, and I. V. Ryaxovskix, *The concept of diagnosis and repair of main gas pipelines in regions with a high predisposition to stress corrosion Gazovaya promyshlennost*, vol. 724, 2015.
- [2] Y. E. Cheng, *Stress Corrosion of Pipeline*, vol. 257, John & Sons Publishing, Hoboken, NJ, USA, 2013.
- [3] F. King, "Stress corrosion cracking of carbon steel used fuel containers in a Canadian deep geological repository in sedimentary rock," report No. NWMO TR-2010-21, Toronto, Canada, 2010.
- [4] A. I. Mixajlov, *Detection, identification and assessment of the depth of stress corrosion using combined magnetoacoustic in-tube flaw detectors// III Scientific and Practical Seminar "Increasing the Reliability of Main Gas Pipes Affected by Stress Corrosion Cracking"*, "Gazprom VNIIGAZ" LLC, Moscow, 2017.
- [5] I. Ryakhovskikh, R. Bogdanov, T. Esiev, and A. Marshakov, "Stress corrosion cracking of pipeline steel in near-neutral pH environment," in *Proceedings of Materials Science Technology*, Pittsburgh, PA, USA, 2014.
- [6] Y. A. Perlovich, O. A. Krymskaya, M. G. Isaenkova et al., "OP Conference Series: Materials Science and Engineering 10, Development, Production and Application," in *Proceedings of the 10th International School-Conference on Materials for Extreme Environment: Development, Production and Application, MEEDPA 2015*, p. 012009, 2016.
- [7] A. I. Zaitsev, I. G. Rodionova, O. N. Baklanova, K. A. Udod, T. S. Esiev, and I. V. Ryakhovskikh, "Structural factors governing main gas pipeline steel stress corrosion cracking resistance," *Metallurgist*, vol. 57, no. 7-8, pp. 695-706, 2013.
- [8] V. Linton, E. Gamboa, and M. Law, "Strategies for the repair of stress-corrosion cracked gas transmission pipelines: Assessment of the potential for fatigue failure of dormant stress-corrosion cracks due to cyclic pressure service," *Journal of pipeline engineering*, vol. 6, no. 4, pp. 207-217, 2007.
- [9] U. Marewski, *UKOPA/GP/009. Near neutral pH and high pH stress corrosion cracking: industry good practice guide*, U. Marewski and M. Steiner, Eds., UK onshore pipeline operators' association, Ambergate, Derbyshire, 2016.
- [10] M. Gintten, "An integrated approach to the integrity management of stress corrosion cracking in pipelines: a case study," in *Proceedings of the Proc. of Rio Pipeline Conference Exposions*, M. Gintten, T. Penney, I. Richardson et al., Eds., 2013.
- [11] A. B. Arabej, O. N. Melyoxin, I. V. Ryaxovskix et al., "Research into the possibility of long-term operation of pipes with low stress corrosion damage," *Vesti gazovoj nauki*, vol. 27, no. 3, pp. 4-11, 2016.
- [12] R. V. Aginej, S. S. Gus'kov, V. V. Mussonov, R. A. Sadrtidinov, and V. A. Lapin, "Investigations of geometric parameters and peculiarities of the location of stress-corrosion damage on main gas pipelines," *Vesti gazovoj nauki*, vol. 27, no. 3, pp. 102-107, 2016.

- [13] R. Bogdanov, A. Marshakov, V. Ignatenko, I. Ryakhovskikh, and D. Bachurina, "Effect of hydrogen peroxide on crack growth rate in X70 pipeline steel in weak acid solution," *Corrosion Engineering, Science and Technology*, vol. 52, no. 4, pp. 294–301, 2017.
- [14] W. Chen, R. Kania, R. Worthingham, and G. V. Boven, "Transgranular crack growth in the pipeline steels exposed to near-neutral pH soil aqueous solutions: The role of hydrogen," *Acta Materialia*, vol. 57, no. 20, pp. 6200–6214, 2009.
- [15] X. Chen, Q. Yuan, B. Madigan, and W. Xue, "Long-term corrosion behavior of martensitic steel welds in static molten Pb-17Li alloy at 550°C," *Corrosion Science*, vol. 96, pp. 178–185, 2015.
- [16] X. Chen, Z. Shen, X. Chen, Y. Lei, and Q. Huang, "Corrosion behavior of CLAM steel weldment in flowing liquid Pb-17Li at 480 °c," *Fusion Engineering and Design*, vol. 86, no. 12, pp. 2943–2948, 2011.
- [17] A. B. Arabey, O. N. Melekhin, O. V. Burutin et al., "Studying the Possibility of Long-Term Operation of Pipes with Insignificant SCC," *3R*, no. 01-02, pp. 104–110, 2017.
- [18] Y. Perlovich, O. Krymskaya, M. Isaenkova, N. Morozov, I. Ryakhovskikh, and T. Esiev, "Effect of layer-by-layer texture inhomogeneity on the stress corrosion of gas steel tubes," *Materials Science Forum*, vol. 879, pp. 1025–1030, 2017.
- [19] C. J. B. Reed, *Electron Probe Analysis and Raster Microscopy (Translation)*, Moscow, Texnosfera, 2008.
- [20] RD 50-672-88. Methodical instructions. Calculations and strength tests. Classification of metals fracture types// Moscow, VNIIGAZ, 2010– 56 p.
- [21] V. A. Subbotin, I. V. Scherbo, S. A. Kholodkov, and M. G. Giorbelidze, "Estimation of static strength of sections of the linear pipeline portion with a colony of corrosion fine cracks," *Samara State Aerospace University Bulletin*, vol. 47, no. 5, pp. 151–157, 2015 (Russian).

Research Article

Pitting Corrosion of the Resistance Welding Joints of Stainless Steel Ventilation Grille Operated in Swimming Pool Environment

Mirosław Szala  and Daniel Łukasik

Department of Materials Engineering, Faculty of Mechanical Engineering, Lublin University of Technology, Nadbystrzycka 36D, 20-618 Lublin, Poland

Correspondence should be addressed to Mirosław Szala; m.szala@pollub.pl

Received 28 January 2018; Accepted 2 April 2018; Published 9 May 2018

Academic Editor: Kai Wang

Copyright © 2018 Mirosław Szala and Daniel Łukasik. This is an open access article distributed under the Creative Commons Attribution License, which permits unrestricted use, distribution, and reproduction in any medium, provided the original work is properly cited.

This work focuses on the pitting corrosion of ventilation grilles operated in swimming pool environments. The ventilation grille was made by resistance welding of stainless steel rods. Based on the macroscopic and microscopic examinations, the mechanism of the pitting corrosion was confirmed. Chemical composition microanalysis of sediments as well as base metal using scanning electron microscopy and energy-dispersive spectroscopy (SEM-EDS) method was carried out. The weldments did not meet the operating conditions of the swimming pool environment. The wear due to the pitting corrosion was identified in heat affected zones of stainless steel weldment and was more severe than the corrosion of base metal. The low quality finish of the joints and influence of the welding process on the weld metal microstructure lead to accelerated deposition of corrosion effecting elements such as chlorine.

1. Introduction

The aesthetic appearance and the ease of keeping the surface clean, good strength properties, ductility, weldability, and corrosion resistance make the use of stainless steels encouraging for elements of the construction and equipment of swimming pools like ventilation grilles. Although polymer materials such as ABS (acrylonitrile butadiene styrene) and PVC (polyvinyl chloride) are relatively cheaper than stainless steel and can also be operated in pool conditions, none of them matches all the mentioned beneficial properties of stainless steel. Stainless steel elements are used to make swimming pool equipment, such as stairs, ladders, ventilation systems (e.g., ventilation grilles), barriers, drainage grills, or other decorative elements. These components can be made from stainless steel grades such as 1.4301, 1.4404, 1.4539, and 1.4547 [1–4], and their chemical composition is presented in Table 1.

According to the environmental corrosivity categories described by the standard [5], the interior of the swimming pool is classified as C4, on a 5-degree scale of corrosiveness

(C1: very low, C5: a very large corrosivity category). That is why one of the basic criteria for the metal materials selection used to build structures and elements of the swimming pool is their resistance to corrosion phenomena. Hence, the operating conditions of metal elements in the pool environment are unstable and difficult to describe, which can prevent grades dedicated to specific applications from meeting the requirements. The high price of more corrosion resistant stainless steel grades containing more expensive alloy components often prompts designers to choose cheaper, more available materials with inferior corrosion resistance. For example, it is a common mistake to use cheaper steel grade like 1.4301 instead of, for example, 1.4401 or 1.4404. The first of these materials is widely used in the construction of food processing equipment and industrial installations, but it corrodes easily in the swimming pool environment [6]. Grade 1.4404, due to the presence of molybdenum and nitrogen, is described in the literature, as dedicated to the production of equipment and design of swimming pools [1–4]. However, in specific swimming pool applications, elements manufactured

TABLE 1: Chemical composition of selected stainless steels according to EN 10088-1 standard [8].

| Steel grade | | Nominal chemical composition [% by mass] | | | | | |
|--------------------|-----------------------|--|-----------|-----------|---------|-----------|--------------|
| Name | Number | C | N | Cr | Mo | Ni | Other |
| X8CrNi18-8 | 1.4301 ^(a) | ≤0,070 | ≤0,11 | 17,5~19,5 | - | 8,0~10,5 | - |
| X2CrNi18-9 | 1.4307 ^(a) | ≤0,030 | ≤0,11 | 17,5~19,5 | - | 8,0~10,5 | - |
| X5CrNiMo17-12-2 | 1.4401 ^(a) | ≤0,070 | ≤0,11 | 16,5~18,5 | 2,0~2,5 | 10,0~13,0 | - |
| X2CrNiMo17-12-2 | 1.4404 ^(a) | ≤0,030 | ≤0,11 | 16,5~18,5 | 2,0~2,5 | 10,0~13,0 | - |
| X1CrNiMoCu25-20-5 | 1.4539 ^(b) | ≤0,020 | ≤0,15 | 19,0~21,0 | 4,0~5,0 | 24,0~26,0 | Cu = 1,2~2,0 |
| X1CrNiMoCuN20-18-7 | 1.4547 ^(c) | ≤0,020 | 0,18~0,25 | 19,5~20,5 | 6,0~7,0 | 17,5~18,5 | Cu = 0,5~1,0 |

^(a)Si ≤ 1,0; Mn ≤ 2,0; P_{max} = 0,045; S ≤ 0,015; ^(b)Si ≤ 0,7; Mn ≤ 2,0; P_{max} = 0,030; S ≤ 0,010; ^(c)Si ≤ 0,7; Mn ≤ 1,0; P_{max} = 0,030; S ≤ 0,010.

from stainless steel grade 1.4404 undergo pitting corrosion, as described in [7].

Works [1–4, 6, 7, 9] describe examples of negative consequences of corrosion phenomena, observed for stainless steels used for swimming pool equipment. The effects of the general or pitting corrosion are usually losses related to the necessity of exchanging corroded elements, such as the case of corrosion of the ventilation duct [6] and drain [7] operated in the pool. In the case of load-bearing elements, pitting corrosion can cause the development of stress corrosion [9, 10]. Pitting is an extremely localized attack that is manifested by holes, or pits, in the metal surface as well as especially in heat affected zones of weld joints [11–13]. Pitting is a particularly insidious form of corrosion since it is difficult to detect until the structure has been severely attacked [4, 6, 7, 12, 14].

In preventing the occurrence of corrosion phenomena of steel elements used in swimming pools, the technological nature of their construction and assembly (e.g., welding) plays an important role. Designing elements should be carried out based on principles such as maintaining high surface smoothness, making structures without sharp corners and undercuts, designing self-cleaning structures, protecting gaps against accumulation of water and sediments in them, using appropriate joining techniques with high care, and the quality of the welding joints finish, so that the joints would have corrosion resistance similar to the base material [1, 12].

Stainless steel corrosion in elements operated in swimming pool environment is considered as a real problem. The literature survey indicates that there is little information about pitting corrosion of stainless steel resistance welding joints. Authors focus mainly on investigating the corrosion of fusion welding processes (e.g., [11, 15–17], [18, p. 304]), none of them influenced by pool environment. The conducted literature review indicates only one paper related to pitting corrosion of resistance welding weldment used in pools [6]. Hence, it can be acclaimed that the state of the art in the field of pitting corrosion resistance of stainless steel weldments operated at swimming pool environments is not entirely investigated.

The aim of the article is to investigate the corrosion of a ventilation grille operated in a swimming pool environment. The grille was made by resistance welding of stainless steel shaped rods.

2. Material and Methodology of Research

The ventilation grille was made of welded stainless steel rods. The tested element was part of the swimming pool ventilation system. The grille was mounted indoors and located at the inlet of the ventilation duct on the wall and had no direct contact with the pool water. The swimming pool atmosphere was characterized by significant humidity resulting from evaporation of pool water. The grille was operated for just a few months until it detected visible corrosion changes and its disassembly.

The temperature of the ventilation system elements was lower than the air temperature in the swimming pool. Chlorinated pool water had a pH close to 7.0. This led to the condensation of water vapor on the ventilation grille, creating conditions for corrosion phenomena to occur on its surface.

Figure 1 shows the examined element and was taken after dismantling the element, dictated by the change of the colour of the grille surface to “rusty.” The presence of corrosion deposit products and pits was observed mainly in areas of joint heat affected zones (HAZ).

In order to recognize the corrosion mechanism, macroscopic and microscopic observations of the worn areas of ventilation grille focused on heat affected zones of resistance welded grille were made. Macroscopic examinations based on the observation of the surface and joint areas were made using a Nikon SMZ 1500 stereomicroscope. To reveal the topography of pitting surfaces, the samples were cleaned using ultrasonic washer in order to remove corrosion products and the steel grille was cross-sectioned on a metallographic cutter (Brillant 200) and then investigated using a Nikon MA200 metallographic microscope. Phenom World ProX scanning electron microscope with chemical composition of the steel and corrosive sediments analysis using SEM-BSD (backscatter electron detector) and SEM-topo modes were carried out.

3. Results

The object of our investigation was the ventilation grille presented in Figure 1. The weldment areas were mostly severely affected by corrosion, which is visible in optical photographs given in Figure 2 as well as in metallographic weldment cross section in Figure 3. Additionally, in photographs acquired

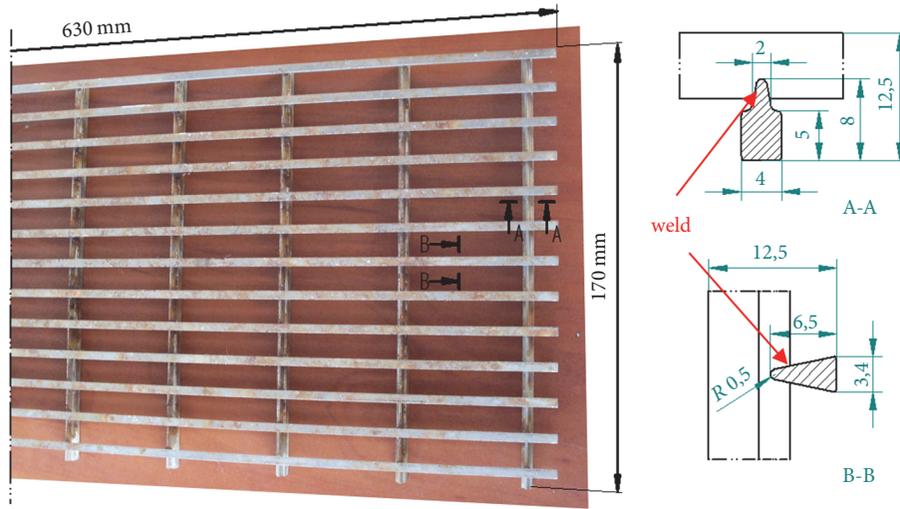


FIGURE 1: Ventilation grille made by resistance welding of stainless steel rods, dimensions in mm.

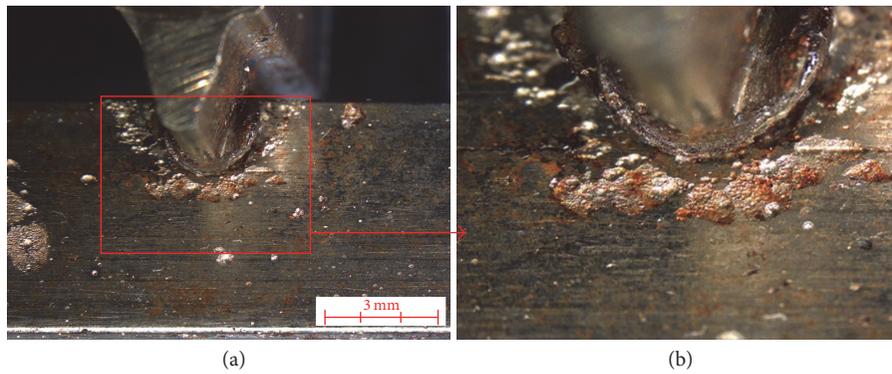


FIGURE 2: Resistance welding weldment corrosion (a) and magnified HAZ (b), stereoscopic microscope.

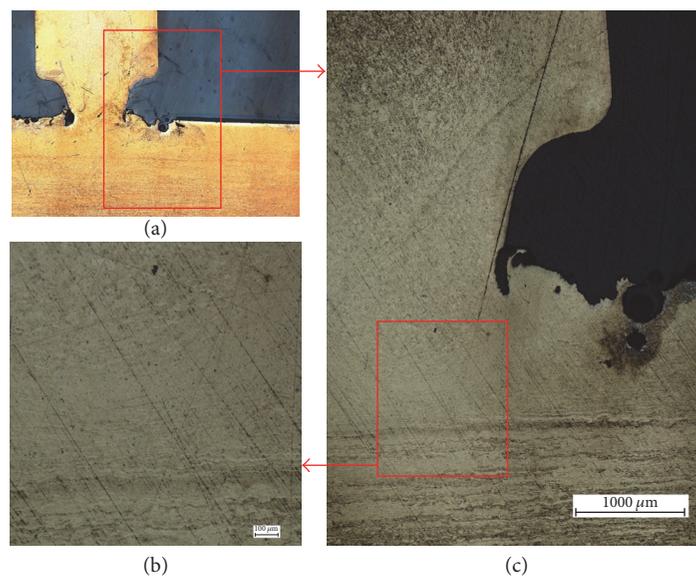


FIGURE 3: Corrosion pits observed in the cross section of joint (a) in the HAZ; (b, c) magnified selected area of microstructure of base metals and heat affected zone presented, metallographic microscope.

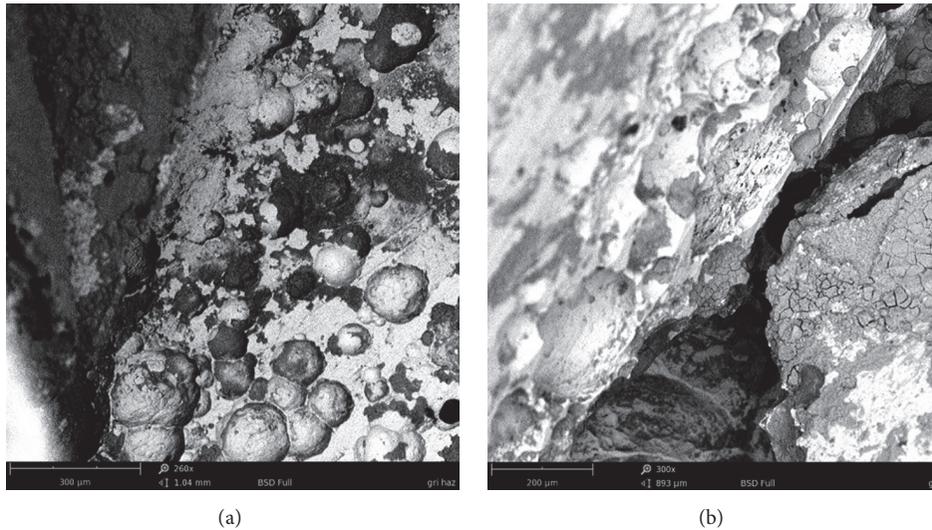


FIGURE 4: The effect of pitting observed in the HAZ (a) and crack between grille rods (b), SEM-BSD.

by the scanning electron microscope, corrosion pits and corrosive sediments are identified, Figure 4. Furthermore, Figure 5, Figure 6, and Table 2 contain the results of chemical composition of base metal and corrosive sediments.

4. Discussion

Stainless steels achieve corrosion resistance thanks to the passive layer of oxides spontaneously formed on the surface of the products. The passive film can be damaged and its restoration depends on the specific characteristics of the material and the environment. In the absence of a passive layer or its damage, the process of corrosion damage is intensified. The investigated grille was manufactured by electric resistance welding, as shown in Figures 1 and 2.

In addition, microstructure of weldment, which differs from the base metal, mostly affects corrosion resistance of stainless steel as presented in Figure 3(a). Results of metallographic investigations of the weldment acknowledged the anisotropy of the structure of welded rods, which derives from metal forming processes, so the area of the weldment that is plastically deformed and influenced by resistance welding process hence contains different microstructure from base metal (Figures 3(b) and 3(c)). In [11, 12], phenomena associated with welded joints, such as dendritic segregation, precipitation of secondary phases, formation of unmixed zones, recrystallization, and grain growth, are listed as influencing the corrosion resistance of the heat affected zone (HAZ). The operating conditions of the ventilation system resulted in deposition of chlorine condensate on the ventilation grille. The cyclic nature of the process led to an increase in the concentration of chlorine in selected places on the surface of the grille. This intensified the occurrence of local corrosion phenomena, including pitting corrosion. It is common knowledge that, at a higher temperature, the oxide film ceases to form due to the lower solubility of oxygen in the solution and the penetration potential decreases with

increasing temperature. Garcia et al. [11] gave information that fusion welding processes can cause local changes in the composition of the welded material, which can alter the stability of the passive layer and its corrosion behaviour [15]. In addition, from the microstructural point of view, the formation of δ -ferrite in stainless steel is another parameter taken into account, since it can be prejudicial because of its susceptibility to attack in a corrosion medium [11, 16], such as a swimming pool, a chlorine-rich environment. According to the literature, the pitting corrosion resistance in pool environment of stainless steel element can be increased using steels with a molybdenum content above 2.5% and chromium above 17% by weight, containing nitrogen.

Leda claims [19] that near nonmetal inclusions, grain boundaries, dislocations, surface nonuniformities, and the probability of corrosion attack increase. The metallurgical purity and homogeneity of steel elements have a great influence on corrosion resistance [13]. Also, the lack of nonmetallic inclusions, especially those located on the surface, in stainless steel such as sulphur are factors that improve corrosion resistance [20]. On the contrary, in the investigated grille, areas of poor weldment finish and surface nonuniformities were identified, visible in Figure 2. They were produced during the resistance welding process due to heat imputed, force used in resistance welding process, and atmosphere. These areas must have been finishing, machined, and chemically etched after welding. Poor metal finish of weldment accelerates concentration of corrosive deposits (e.g., chlorine-rich) that can influence corrosion of weldment. In order to prevent the corrosion of the ventilation grille to remove chlorine-containing deposits from its surface, it is possible to periodically wash its surface. We also proposed that grilles produced by resistance welding process could not meet requirements of harsh operating pool environment due to difficulties connecting to finishing treatment of weldment.

The formation of corrosion pits on stainless steel elements in the atmosphere of the swimming pool is caused mostly

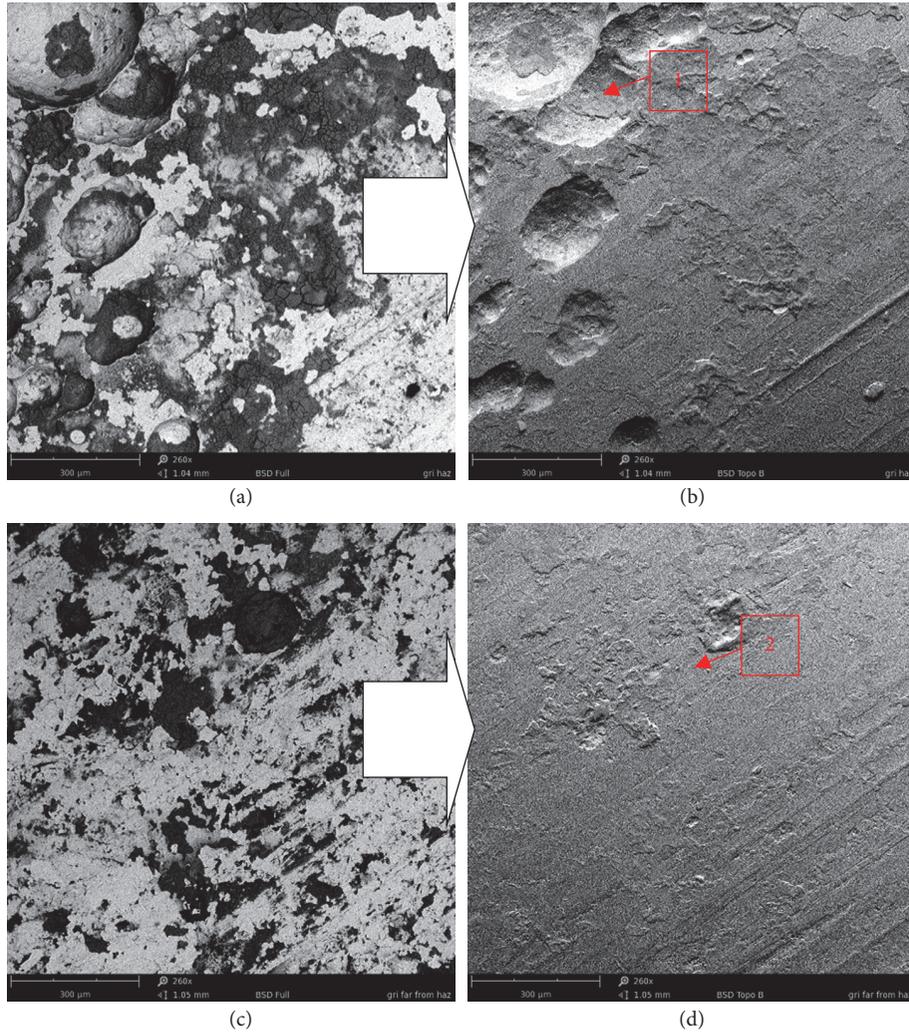


FIGURE 5: Comparison of grille surfaces observed in the heat affected zone HAZ (a, b) and in distance of HAZ (c, d). SEM-BSD and SEM-BSD-topo modes. Points 1 and 2 are locations of chemical analysis; results presented in Figure 6 and Table 2.

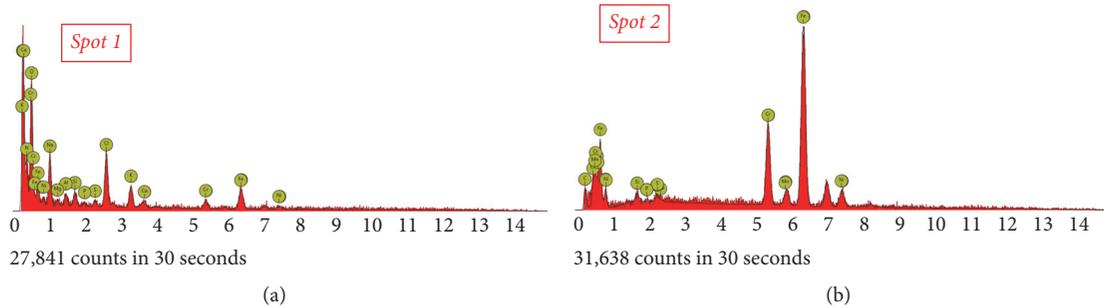


FIGURE 6: Spectrogram (SEM-EDS) obtained due to chemical analysis conducted in spots marked in Figure 5: (a) a corrosive sediment and (b) surface of base metal.

by increased temperature and high concentration of chlorine ions in the air. As a result of pitting corrosion attack, the tested ventilation grille corrosion products and corrosion pits were noted, as shown in Figures 2, 3, 4, and 5, especially in the heat affected zone (HAZ). The dimensions of pits on the surface of the element reached 1 mm. The depths of pits observed on the

cross-sectional surface of the test piece were approx. 0.3 mm (Figure 2). On the contrary, base metal was less corroded (Figure 3). On the whole, the morphology of identified pits indicates pitting corrosion attack [6, 7, 10].

Examination of HAZ acknowledged visible severe pitting action, Figures 3 and 4(a), and generation of deep cracks

TABLE 2: The results of chemical composition analysis at spot 1 (sediment) and spot 2 (metal surface) in Figure 5.

| Element | Spot 1: sediment | | Spot 2: base metal | |
|------------|----------------------|-----------|----------------------|-----------|
| | Concentration [wt.%] | Error [%] | Concentration [wt.%] | Error [%] |
| Aluminium | 1.3 | 7.8 | - | - |
| Calcium | 0.8 | 10.5 | - | - |
| Carbon | 8.3 | 2.0 | 1.0 | 6.9 |
| Chlorine | 5.3 | 3.0 | - | - |
| Chromium | 2.1 | 7.4 | 16.8 | 2.3 |
| Iron | 8.0 | 4.2 | 67.0 | 1.5 |
| Magnesium | 0.9 | 13.5 | - | - |
| Manganese | - | - | 1.9 | 10.5 |
| Molybdenum | - | - | 1.8 | 13.1 |
| Nickel | 2.0 | 12.6 | 10.3 | 5.2 |
| Nitrogen | 11.0 | 3.6 | - | - |
| Oxygen | 44.4 | 2.2 | - | - |
| Phosphorus | 0.3 | 18.0 | 0.2 | 51.6 |
| Potassium | 2.6 | 4.8 | - | - |
| Silicon | 1.0 | 7.4 | 0.8 | 14.2 |
| Sodium | 11.6 | 3.4 | - | - |
| Sulfur | 0.5 | 12.9 | 0.2 | 16.4 |

in between welded rods, Figures 3 and 4(b). Inside crack corrosion pits and corrosive deposits were identified. While comparing areas presented in Figure 5, it is clearly visible that the HAZ was affected by corrosion compared to the base metal. In the vicinity of the HAZ, the occurrence of pits and corrosion deposits is evident.

Results of chemical analysis of the corrosion deposits and welded steel are presented qualitatively in Figure 6(a) and quantitatively in Table 2. Spectroscopic analysis of base metal (Figure 6(b), Table 2) indicated that the investigated element could have been manufactured from stainless steel grade 1.4401 or 1.4404 (Table 1); however, it is known that the content of carbon could not be properly identified properly by SEM-EDS method. Deposits contain chemical elements which came from swimming pool environment and are used for swimming pool water treatment (e.g., Cl, Ca, Table 2). In particular, chlorine compounds play a major role in the pitting corrosion processes [6, 7] and content of chlorine in deposits equals 5.3%. In addition, the relatively high temperature of water and air in the swimming pool causes evaporation of chlorinated pool water. Ventilation systems in swimming pools often work in a closed circuit, which makes the metal elements used at the pool exposed to the effects of moist air characterized by increased concentration of chlorine ions or chlorine compounds (chloramines) [4, 7]. The mentioned factors definitely favour the occurrence of corrosion phenomena, mainly general, stress, and pitting corrosion. However, to characterize a corrosive sediment precisely, for further understanding the nature of the sediments, the XRD (X-ray diffraction) investigations should be employed. The intensification of corrosion phenomena was also influenced by poor weldment finish that accelerates deposition of corrosive elements (e.g., chlorine). In order to prevent ventilation grille from corrosion, the systematic

removal of chlorine-containing sediments from its surface must be taken into account.

5. Conclusions

The case study on the subject of the pitting corrosion of resistance welding joints found in the stainless steel ventilation grille utilised in a swimming pool environment was investigated in the work. The following conclusions can be drawn on the basis of the conducted analysis.

The results confirmed that pitting corrosion was the main corrosion mechanism of the stainless steel ventilation grille. Heat affected zone (HAZ) of resistance welded joint of grille operated in swimming pool environment was lower than resistance of stainless steel based material.

The investigated ventilation grille was manufactured from stainless steel type Cr-Ni-Mo, probably grade 1.4401 or 1.4404. Pitting corrosion affects mostly the weldment area due to its microstructure which differs from the base metal. The intensification of corrosion phenomena was also influenced by poor weldment finish which accelerates deposition of corrosive elements (e.g., chlorine).

The environment as well as the operating conditions of an element affects the corrosive wear of stainless steel grille. The increase in concentration of chlorine deposited on the corroded grille areas has been identified. Chlorine plays a major role in the pitting corrosion processes of stainless steel.

In order to prevent ventilation grille from corrosion, the removal of chlorine-containing sediments from its surface must be taken into account.

Conflicts of Interest

The authors declare that there are no conflicts of interest regarding the publication of this paper.

References

- [1] N. Baddoo and P. Cutler, "Stainless steel in indoor swimming pool buildings," *Technical Note: Swimming Pools*, 2007.
- [2] "Stress corrosion cracking failure," <http://www.corrosion-doctors.org/Forms-SCC/swimming.htm>.
- [3] C. Houska and J. Fritz, *Successful Stainless Swimming Pool Design*, Nickel Institute, 2017.
- [4] "Stainless steel in swimming pool buildings - selecting and using stainless steel to cope with changes in swimming pool design," Nickel Development Institute, 2010, https://www.nickelinstitute.org/~Media/Files/TechnicalLiterature/StainlessSteelInSwimmingPoolBuildings_12010_.pdf.
- [5] ISO 12944-1:2001, "Paints and varnishes — Corrosion protection of steel structures by protective paint systems — Part 1: General introduction".
- [6] P. Sedek, J. Brózda, and J. Gazdowicz, "Pitting corrosion of the stainless steel ventilation duct in a roofed swimming pool," *Engineering Failure Analysis*, vol. 15, no. 4, pp. 281–286, 2008.
- [7] M. Szala, K. Beer-Lech, and M. Walczak, "A study on the corrosion of stainless steel floor drains in an indoor swimming pool," *Engineering Failure Analysis*, vol. 77, pp. 31–38, 2017.
- [8] "PN-EN 10088-1:2014 - Stainless steels. Part 1: List of stainless steels".
- [9] J. Woodtli and R. Kieselbach, "Damage due to hydrogen embrittlement and stress corrosion cracking," *Engineering Failure Analysis*, vol. 7, no. 6, pp. 427–450, 2000.
- [10] D. A. Horner, B. J. Connolly, S. Zhou, L. Crocker, and A. Turnbull, "Novel images of the evolution of stress corrosion cracks from corrosion pits," *Corrosion Science*, vol. 53, no. 11, pp. 3466–3485, 2011.
- [11] C. Garcia, F. Martin, P. de Tiedra, Y. Blanco, and M. Lopez, "Pitting corrosion of welded joints of austenitic stainless steels studied by using an electrochemical minicell," *Corrosion Science*, vol. 50, no. 4, pp. 1184–1194, 2008.
- [12] J. N. DuPont, J. C. Lippold, and S. D. Kiser, *Welding Metallurgy and Weldability of Nickel-Base Alloys*, John Wiley & Sons, Inc, 2009.
- [13] S. J. Kim, S. G. Hong, and M.-S. Oh, "Effect of metallurgical factors on the pitting corrosion behavior of super austenitic stainless steel weld in an acidic chloride environment," *Journal of Materials Research*, vol. 32, no. 7, pp. 1343–1350, 2017.
- [14] I. Lenart and M. Szala, "Korozja wżerowa eksploatowanej na pływalni kratki wentylacyjnej wykonanej ze stali nierdzewnej," in *Prace Naukowe Młodych Badaczy: TYGIEL*, M. Szala, Ed., pp. 208–223, Lublin: Politechnika Lubelska, 2013.
- [15] E. Zumelzu, J. Sepúlveda, and M. Ibarra, "Influence of microstructure on the mechanical behaviour of welded 316 L SS joints," *Journal of Materials Processing Technology*, vol. 94, no. 1, pp. 36–40, 1999.
- [16] R. Chen, P. Jiang, X. Shao, G. Mi, and C. Wang, "Effect of magnetic field applied during laser-arc hybrid welding in improving the pitting resistance of the welded zone in austenitic stainless steel," *Corrosion Science*, vol. 126, pp. 385–391, 2017.
- [17] J. Kim, B. Lee, W. Hwang, and S. Kang, "The Effect of Welding Residual Stress for Making Artificial Stress Corrosion Crack in the STS 304 Pipe," *Advances in Materials Science and Engineering*, vol. 2015, pp. 1–7, 2015.
- [18] X. Li, B. Gong, C. Deng, and Y. Li, "Failure mechanism transition of hydrogen embrittlement in AISI 304 K-TIG weld metal under tensile loading," *Corrosion Science*, vol. 130, pp. 241–251, 2018.
- [19] H. Leda, "Materiały inżynierskie w zastosowaniach biomedycznych," *Wydawnictwo Politechniki Poznańskiej*, 2012.
- [20] E. A. Abd El Meguid, N. A. Mahmoud, and S. S. Abd El Rehim, "Effect of some sulphur compounds on the pitting corrosion of type 304 stainless steel," *Materials Chemistry and Physics*, vol. 63, no. 1, pp. 67–74, 2000.

Research Article

Corrosion and Leaching Behaviours of Sn-0.7Cu-0.05Ni Lead-Free Solder in 3.5 wt.% NaCl Solution

Jan-Ervin C. Guerrero,¹ Drexel H. Camacho ,¹ Omid Mokhtari,² and Hiroshi Nishikawa²

¹Chemistry Department, De La Salle University, 2401 Taft Avenue, 0922 Manila, Philippines

²Joining and Welding Research Institute, Osaka University, 11-1 Mihogaoka, Ibaraki, Osaka 567-0047, Japan

Correspondence should be addressed to Drexel H. Camacho; drexel.camacho@dlsu.edu.ph

Received 6 December 2017; Accepted 5 March 2018; Published 2 May 2018

Academic Editor: Arvind Singh

Copyright © 2018 Jan-Ervin C. Guerrero et al. This is an open access article distributed under the Creative Commons Attribution License, which permits unrestricted use, distribution, and reproduction in any medium, provided the original work is properly cited.

The corrosion and leaching behaviour of a new ternary Sn-0.7Cu-0.05Ni alloy in 3.5 wt.% NaCl solution is reported herein. Potentiodynamic polarization measurements show that Sn-0.7Cu-0.05Ni has the highest corrosion rate. Results of the 30-day Sn leaching measurement show that Sn-Cu-Ni joint has slight decrease attributed to the formation of thin passivation film after 15 days. The leaching amounts of Sn are observed to be higher in solder joint than in solder alloy due to the galvanic corrosion happening on the surface. EDS and XRD results of the corroded surface confirm that the corroded product is made up of oxides of tin.

1. Introduction

Solder, a fusible metal alloy used to join metal pieces, is a staple material in the electronics industry. It functions as an adhesive or joining material to provide electrical continuity between the active silicon die, the substrate, and the printed wiring boards [1]. Solder alloys made up of tin and lead (Sn-Pb) predominate the manufacturing and electronics industries for years. However, due to the bad effects of lead and its compounds to human health and the environment [2], its use has been widely limited if not banned.

Global lead-free regulations started with the US banning lead (Pb) in gasoline additives, plumbing, and construction [3]. Japan pioneered the use of lead-free solders in the electronics industry and the European Union (EU) passed the restriction of the use of certain hazardous substances (ROHS) in electrical and electronic equipment banning the use of lead, mercury, and cadmium, among others [4]. Thus, there was a critical necessity to look for alternatives to Pb solders for the electronics industry. For solders to be a good environmentally benign substitute to Pb, it should be cost-effective and should mimic the properties of Pb, that is, low melting temperature (around 183°C), good mechanical, thermal, and electrical properties. Almost every lead-free solder

in the market is Sn-based solders such as Sn-Ag-Cu and Sn-Cu [1]. At present, there is no common standard for lead-free electronic products since each country or region has its own recommended lead-free solders. In the US, the National Electronic Manufacturing Initiative, Inc., (NEMI) recommends Sn-3.9Ag-0.6Cu as the lead-free solder. Japan, through the Japan Electronic and Information Technology Association (JEITA), recommends the use of Sn-3.0Ag-0.5Cu solder alloy, while the European Consortium recommends Sn-3.8Ag-0.5Cu as the lead-free solder. Overall, the most common type of lead-free solder (LFS) used worldwide is the alloy made up of Sn-Ag-Cu. Alternative Pb-free solder systems such as Sn-Ag, Sn-Bi, Sn-Zn, and Sn-Cu have been developed [1, 5, 6] but uncertainties in their integrity and reliability limited their use in consumer products [7]. New types of lead-free solders are being used by some companies in Japan; Panasonic and Hitachi use Sn-Ag-Bi, Sharp uses Sn-Bi, and Sony uses Sn-Ag-Bi-Cu and Sn-Ag-Bi-Ge solder alloys in their products [3, 4]. New lead-free solder alloys are being studied [8–10] and reliable solders for general and specific applications are still highly sought.

The ternary alloy Sn-0.7Cu-0.05Ni has been shown to be a potential Pb-free solder [11] where the wettability of the alloy was shown to be comparable with some other lead-free

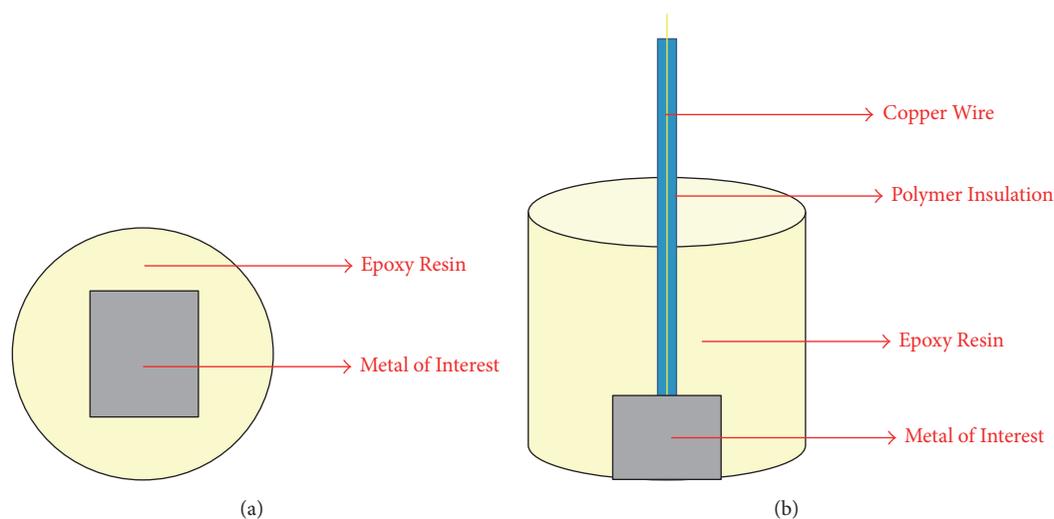


FIGURE 1: Schematic diagram of the working electrode. (a) Bottom view; (b) side view.

solders [12]. The low experimental wetting angle is a consequence of the addition of Ni in Sn-0.7% wt. Cu. Increasing the amount of Ni also decreases the void percentage and Cu_3Sn growth in Sn-Cu solder alloy [13]. The tensile properties and wettability in solder joints with Cu also improved as a result of adding 0.05 wt.% Ni [14]. The addition of 0.05 wt.% Ni to Sn-0.7Cu solder was shown to effectively reduce the formation of intermetallic compound (IMC) layer at the interface during the reflow process and for inhibiting the growth of IMC during the aging process [15].

To study further the potential of Sn-0.7Cu 0.05Ni solder alloy, there is a need to assess its corrosion behaviour as it is an important factor to consider in formulating new solder materials [16]. The presence of moisture and corrosive salts/ions triggers the corrosion activity of these solder metals affecting the form, fit, and function of the electronic device [17, 18]. Corrosion behaviours of lead-free solders are mainly studied using sodium chloride (NaCl) electrolyte to simulate the seawater condition using different types of lead-free solders [19–24]. Li et al. [20] reported that lead-free solders such as Sn-3.5Ag, Sn-0.7Cu, and Sn-3.8Ag-0.7Cu exhibit better corrosion resistance than Sn-Pb solder in 3.5 wt.% NaCl solution, where Sn-3.5Ag solder was found to be the most resistant among them. Lead-free solder exhibits better corrosion resistant because it exhibits lower passivation current density, lower corrosion current density after the breakdown of the passivation film, and a more stable passivation film on the surface compared to Sn-Pb solder. By investigating the corrosion behaviours of new lead-free solders, the fatigue life of the material can be predicted. A cursory survey of the literature reveals zero investigation on the corrosion behaviour of the new ternary Sn-0.7Cu-0.05Ni alloy. The goal of the present study is to investigate the corrosion resistance of Sn-0.7Cu-0.05Ni as compared to commercially used solder alloys and metal and study the leaching behaviour of tin in the alloys and in their corresponding joints in 3.5 wt% NaCl solution.

2. Materials and Methods

2.1. Materials

2.1.1. Preparation of Working Electrode. The compositions of the solder alloys used in the study are Sn-0.7 wt.% Cu-0.05 wt.% Ni, Sn-3.0 wt.% Ag-0.5 wt.% Cu and Sn-0.8 wt.% Cu, 60 wt.% Sn-40 wt.% Pb, and pure Sn metal. The alloys were cut using low-speed cut-off saw into square blocks (approximate dimension of $0.5 \times 0.5 \times 0.5$ cm). Each metal piece was attached to an insulated Cu wire by hand soldering using the same metal alloy to provide electrical connections and then cold-mounted using epoxy resin as shown in Figure 1. The specimens were ground using SiC paper/sand paper up to 1200 grit, rinsed with distilled water, and cleaned in an ultrasonic cleaner for 2 mins. The surface area exposed to the test solution was $0.5 \pm 0.2 \text{ cm}^2$.

2.1.2. Preparation of Solder Alloy and Solder Joint for Leaching Measurement. Solder joints were prepared by joining a previously acid-cleaned (HNO_3/MeOH) copper plate ($5 \times 10 \times 2$ mm) with similarly sized lead-free solder plate using a solder paste. The coupled metals were heated on a hot plate at 230°C until the solders stuck on the Cu plate. For leaching experiments, the samples were prepared as shown in Figure 2.

2.1.3. Preparation of Solution. The corrosion test was carried out at room temperature in air-saturated aqueous solution of 3.5 wt.% NaCl prepared by dissolving 17.5 grams of analytical grade NaCl dissolved in deionized water to make a 500 mL solution.

2.2. Methods

2.2.1. Potentiodynamic Polarization Method–Tafel Plot. Electrochemical measurements were carried out in a single compartment cell using a standard three-electrode setup: Ag/AgCl (3 M KCl) as a reference electrode, a platinum sheet

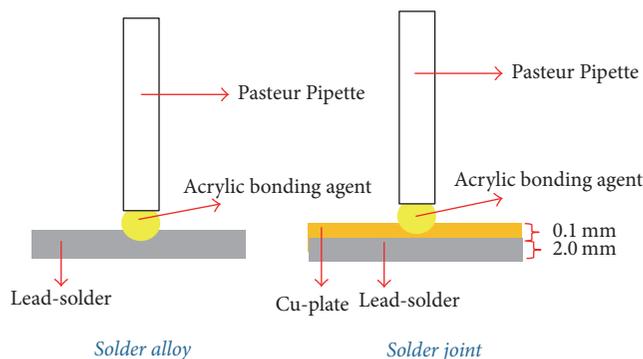


FIGURE 2: Preparation of samples for leaching measurements.

(0.64 cm^2) as a counter electrode, and the lead-free solders as the working electrode. All the measurements were done under N_2 conditions. Metrohm Autolab PGSTAT 128 N was used as an electrochemical interface to control and record the potential. The samples were immersed in 250 mL corrosive medium inside the cell at room temperature for 180 s to attain a steady-state potential or open circuit potential (OCP). Potentiodynamic polarization curves were determined at -1500 to 500 mV range distinctive for the lead-free solder used on the study at an ASTM scan rate of 1.00 mV/s ; step potential is at 0.45 mV and is presented in the form of typical polarization curves $\log I$ versus voltage. From the Tafel plot, the corrosion current (I_{CORR}), corrosion potential (E_{CORR}), polarization resistance (R_p), and corrosion rate (CR) of the metal alloys were calculated using the corrosion rate, Tafel slope method (Autolab application note COR02).

2.2.2. Leaching Measurements. For the leaching/dissolution measurement, the method by Cheng et al. [25] was adopted with slight modification. Small test cells containing 15 mL of test solutions were placed in a temperature-controlled oil bath at $45 \pm 3^\circ\text{C}$. Every 3 days, oxygen was injected into the test solutions by gas flowmeter with a flow rate of 46 mL/min for 5 mins to keep the solution under low saturation of oxygen. Two mL of fresh test solutions was added to the test cell every 7 days or when the solution is reduced to keep the solution at 15 mL. The testing periods were done for 7, 15, and 30 days. After immersion for the subscribed period, 15 mL was taken and diluted into a 25 mL volumetric flask with deionized water. If there exists some precipitation in the test solution, sodium phosphate solution was used to dissolve the precipitates. The concentration of Sn in the diluted solution was analyzed using Atomic Absorption Spectrophotometer (Shimadzu AA-6300 Atomic Absorption Spectrophotometer) and the leaching amount per surface area of each element in the solders and their joints were calculated.

2.2.3. Surface Morphology and Elemental Analysis. The corroded surfaces of the samples were investigated using field-emission scanning electron microscopies (FESEM) (JEOL JSM-5310) and SEM (JEOL JSM-6500F) both equipped

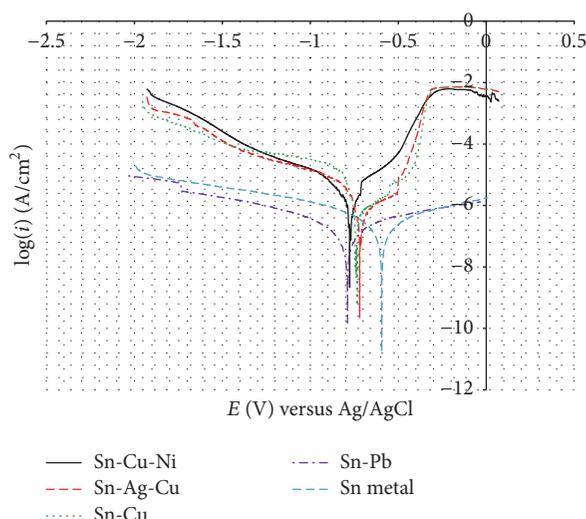


FIGURE 3: Potentiodynamic polarization curves of Sn and solder alloys in 3.5 wt.% NaCl solution under N_2 atmosphere. Scan range: from -1500 to 500 mV ; scan rate: 1.00 mV/s ; step potential: 0.45 mV .

with an energy dispersive X-ray spectroscopy (EDS). X-ray diffraction (XRD) measurements were performed with a diffractometer (Rigaku Ultima IV) using $\text{Cu-K}\alpha$ radiation ($\lambda = 1.5405 \text{ \AA}$) at an accelerating voltage of 40 kV . The diffracted beam was scanned in steps of 0.02° across a 2θ range of 20 – 90° .

3. Results and Discussion

3.1. Potentiodynamic Polarization Method–Tafel Plot. The Sn-0.7CuNi0.05 (referred to herein as Sn-Cu-Ni) in 3.5 wt.% NaCl solution showed a Tafel plot positioned at (E_{CORR}) -0.78 mV versus Ag/AgCl (Figure 3). As compared to Sn-3.0Ag-05Cu (referred to herein as Sn-Ag-Cu) and Sn-0.8Cu (referred to herein as Sn-Cu) alloys, there is an observed shift of corrosion potential E_{CORR} of lead-free solders to a less negative value following the sequence Sn-Cu-Ni < Sn-Cu < Sn-Ag-Cu. During the anodic polarization process, a stable passivation film is formed on the surface of the metal alloys (*vide infra*). This passivation film determines the corrosion behaviour of the solder in the given media. The shift to a less negative potential signifies a formation of a more stable passivation film [26], which protects the solders and increases their corrosion resistance. The polarization resistance (R_p) data (Table 1) showed that Sn-Pb solder has the highest R_p ($805.250 \text{ K}\Omega$) and lowest corrosion rate ($0.1949 \times 10^{-2} \text{ mm/yr}$) compared to the lead-free solders. Between the three lead-free solder alloys, Sn-Cu-Ni showed the highest corrosion rate and Sn-Ag-Cu showed the lowest corrosion rate in 3.5 wt.% NaCl solution.

3.1.1. Microstructure Characterization of the Lead-Free Solders. The microstructure of solders before potentiodynamic polarization (Figure 4(a)) is a smooth surface showing the polishing lines and EDS analysis confirms the elemental

TABLE 1: Summary of corrosion parameters of metal alloys in 3.5 wt.% NaCl solution.

| Sample | E_{corr} (V) versus Ag/AgCl | I_{corr} ($\mu\text{A}/\text{cm}^2$) | R_p ($\text{k}\Omega$) | CR (mm/yr) $\times 10^{-2}$ |
|----------|---|--|-------------------------------|--|
| Sn-Cu-Ni | -0.78 | 8.98 | 14.94 | 4.87 |
| Sn-Ag-Cu | -0.73 | 3.06 | 43.86 | 1.71 |
| Sn-Cu | -0.75 | 3.91 | 28.26 | 2.07 |
| Sn-Pb | -0.79 | 0.39 | 805.25 | 0.19 |
| Sn | -0.59 | 0.55 | 406.02 | 0.23 |

E_{corr} : corrosion potential, I_{corr} : corrosion current density, R_p : polarization resistance, and CR: corrosion rate.

TABLE 2: Surface element concentration of different solders before potentiodynamic polarization in 3.5 wt.% NaCl solution.

| | Surface element composition (atom%) | | | | |
|----------|-------------------------------------|------|------|------|-------|
| | Sn | Ag | Cu | Ni | Pb |
| Sn-Cu-Ni | 98.59 | - | 1.27 | 0.14 | - |
| Sn-Ag-Cu | 96.74 | 2.74 | 0.52 | - | - |
| Sn-Cu | 98.97 | - | 1.38 | - | - |
| Sn-Pb | 59.03 | - | - | - | 40.97 |
| Sn | 100.00 | - | - | - | - |

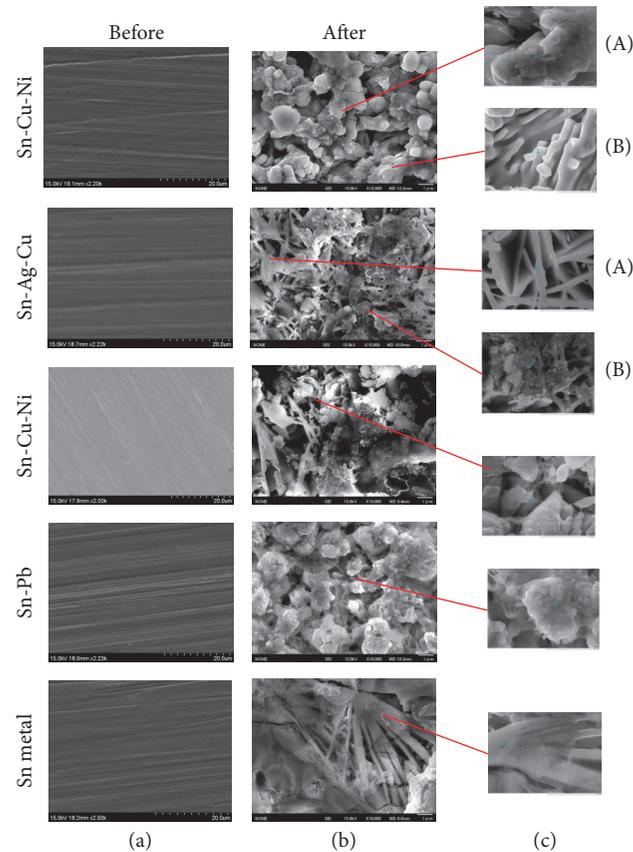


FIGURE 4: The microstructure of the metal surfaces on different solders before (a), after (b), and distinct morphologies on specified points (c) after potentiodynamic polarization tests in 3.5 wt.% NaCl solution.

composition of each solder (Table 2). After potentiodynamic polarization in 3.5 wt.% NaCl solution (Figure 4(b)), the microstructure of corroded Sn-Cu-Ni alloy had a porous flake-like surface while the Sn-Ag-Cu and Sn-Cu solders showed fibrous network oriented randomly on the surface in agreement with the observations of Li et al., [20]. Notable is the flake-like microstructures in Sn-Cu-Ni, which is similar in some respect to the Sn-Pb alloy. The EDS analysis on the surface of the corroded samples on each specified point was determined (Figure 4(c) and Table 3) and revealed the presence of Sn, O, and Cl indicating that the corrosion products are composed of the oxides and chlorides of tin. In conventional electrochemical reaction, Sn acts as an anode and reacts with Cl^- from the medium to form SnCl_2 , which results in pitting and severed dissolution of Sn [27].

The cross-section of the metals after potentiodynamic polarization (Figure 5) showed visible corrosion layers distinct from the bulk metal. EDS analysis of the cross-section area (Table 4) for both lead and lead-free solders showed the top layer having similar corrosion products composed of Sn-rich and O-rich areas with $<1\%$ Cl. The Sn-Pb solder showed an outer layer rich in O while the inner layer was rich in Sn. The formation of oxides on the surface of the Sn-Pb solder indicates the presence of a stable passivation film that protects the metal from corroding. This explains why Sn-Pb solder has a better corrosion resistance than lead-free solders. In the case of the lead-free solders, since they have a different composition than Sn-Pb, the thin layer of oxides that formed on the surface of the alloy is not enough to protect the metal from the electrochemical process.

TABLE 3: Surface element concentration of different solders *after* potentiodynamic polarization in 3.5 wt.% NaCl solution on specific points as indicated in Figure 4(c).

| | Surface element concentration (atom%) | | | | | | |
|--------------|---------------------------------------|----|------|----|----|-------|-------|
| | Sn | Ag | Cu | Pb | Ni | Cl | O |
| Sn-Cu-Ni (A) | 20.40 | - | 1.90 | - | - | 3.50 | 74.20 |
| Sn-Cu-Ni (B) | 56.70 | - | 0.80 | - | - | 0.20 | 42.30 |
| Sn-Ag-Cu (A) | 23.60 | - | - | - | - | 8.70 | 67.70 |
| Sn-Ag-Cu (B) | 32.30 | - | 0.20 | - | - | 12.10 | 55.40 |
| Sn-Cu | 20.50 | - | 0.10 | - | - | 10.70 | 68.70 |
| Sn-Pb | 28.40 | - | - | - | - | 0.60 | 71.00 |
| Sn | 29.90 | - | - | - | - | 15.00 | 55.10 |

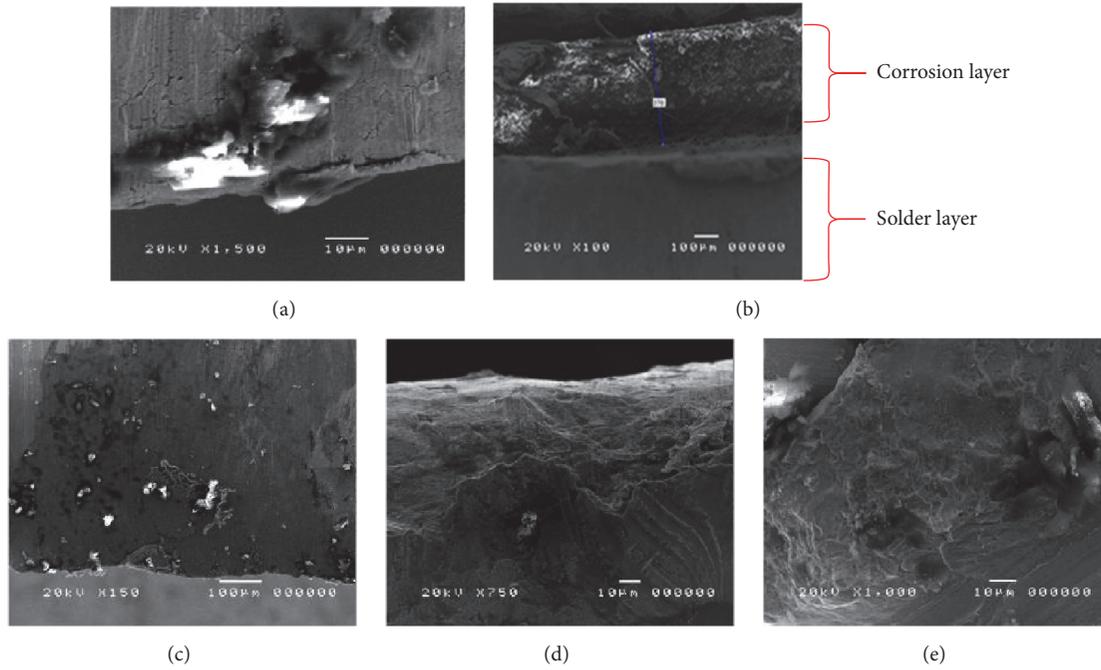
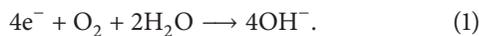


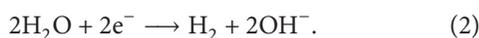
FIGURE 5: Cross-section image of the solders after potentiodynamic polarization test in 3.5 wt.% NaCl solution. (a) Sn; (b) Sn-Pb; (c) Sn-Ag-Cu; (d) Sn-Cu-Ni; (e) Sn-Cu.

3.1.2. Phase Composition Analysis of Corrosion Product on the Surface of the Solder Sample. The XRD diffractograms of corrosion products (Figure 6) showed corresponding XRD peaks attributed to tin oxides (SnO and SnO₂) and some chlorides. When compared with the XRD results of Yan and Xian [28] peaks for tin hydroxide (Sn(OH)₂) were also observed particularly for Sn-Pb and Sn metal [25]. These oxides effectively protect the metal. The oxides, however, were not visibly detected in Pb-free solders indicating nil or minimal formation of the passivation layer.

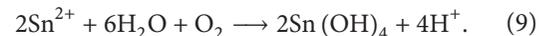
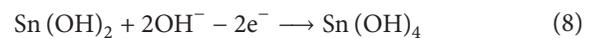
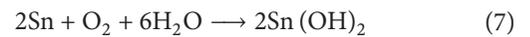
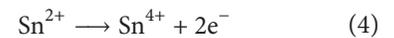
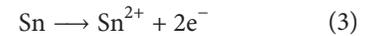
During potentiodynamic polarization measurements, the reduction of oxygen in the neutral aqueous solution (1) initially occurs [20]



Once the current reaches 10 mA/cm², bubbles were observed from the solution caused by the evolution of hydrogen from the cathode.



The following plausible anodic reactions would occur [17, 19]:



Formation of tin oxides is thermodynamically favourable thus tin hydroxides can dehydrate easily to form SnO and SnO₂ [25, 29]. Although not detected in XRD due to its trace concentration relative to Sn, the potential corrosion products

TABLE 4: Cross-section element concentration of different solders after Potentiodynamic polarization tests in 3.5 wt.% NaCl solution.

| | Cross-section element concentration (atom%) | | | | | | |
|-----------------|---|------|------|------|-------|------|-------|
| | Sn | Ag | Cu | Ni | Pb | Cl | O |
| Sn-Cu-Ni | | | | | | | |
| Top layer | 63.99 | - | 0.60 | 0.22 | - | 0.92 | 33.91 |
| Inner layer | 98.59 | - | 1.27 | 0.14 | - | - | - |
| Sn-Ag-Cu | | | | | | | |
| Top layer | 40.95 | 1.12 | 0.17 | - | - | 0.15 | 57.27 |
| Inner layer | 97.36 | 2.01 | 0.63 | - | - | - | - |
| Sn-Cu | | | | | | | |
| Top layer | 64.58 | - | 0.72 | - | - | 0.60 | 33.35 |
| Inner layer | 99.30 | - | 0.70 | - | - | - | - |
| Sn-Pb | | | | | | | |
| Top layer | 6.85 | - | - | - | 3.91 | 0.91 | 88.03 |
| Inner layer | 60.16 | - | - | - | 39.84 | - | - |
| Sn | | | | | | | |
| Top layer | 32.62 | - | - | - | - | 0.37 | 66.41 |
| Inner layer | 99.85 | - | - | - | - | 0.15 | - |

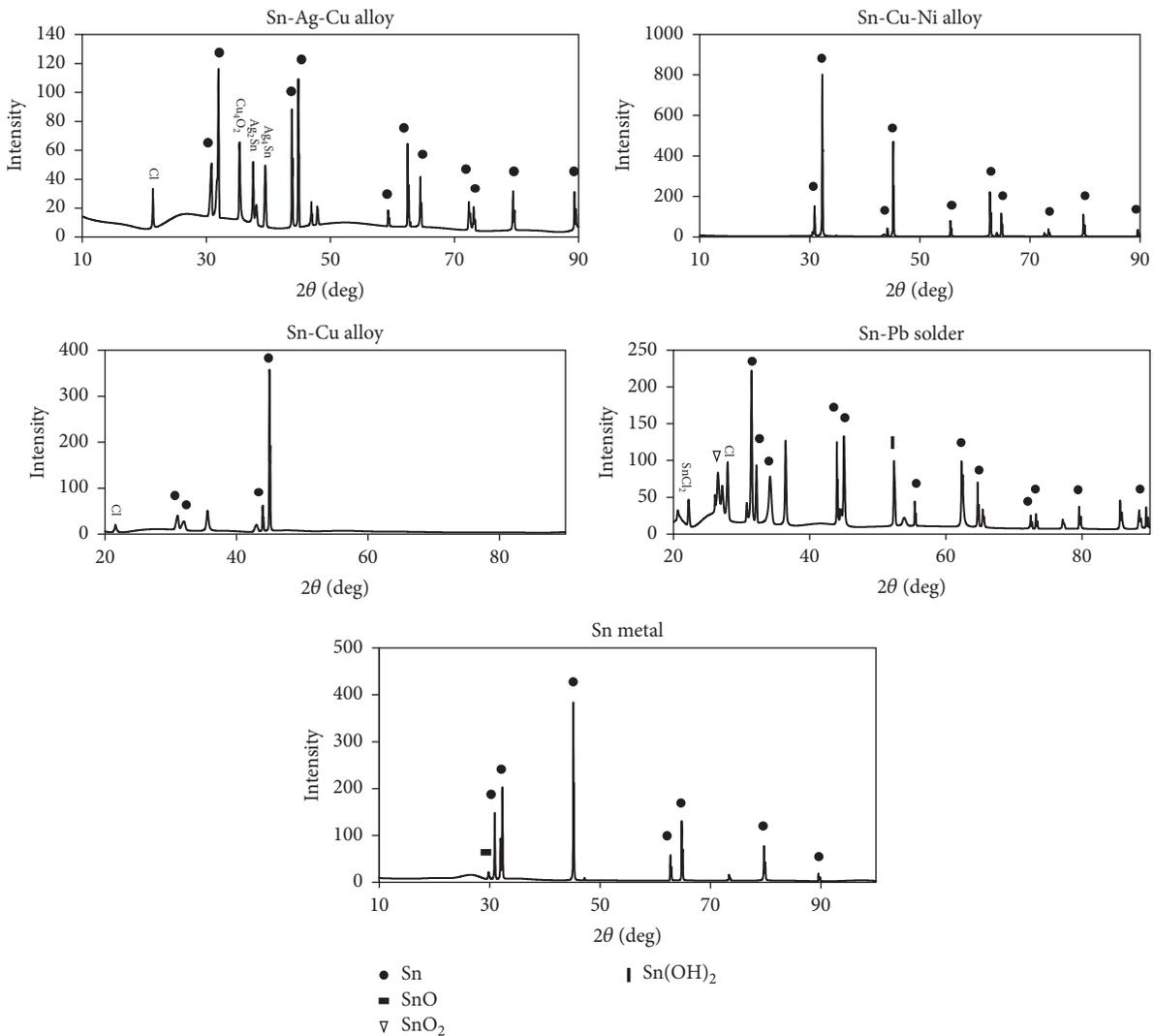
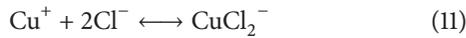
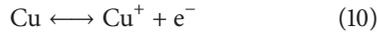
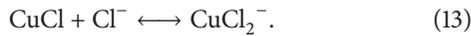
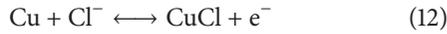


FIGURE 6: XRD patterns of surface product on different solder material after potentiodynamic polarization test.

of copper and nickel are metal chlorides. Corrosion of copper is dependent on the presence of chloride ions either through direct formation of cupric chloride



or through the electro-dissolution of copper [30]



The anodic polarization of copper alloys in NaCl solution lowers the fracture stresses as measured in slow strain experiments making copper alloys under cyclic stresses to have lower service lives in chloride solutions [31]. Thus, chlorides penetrate into the material crevices allowing for corrosion of susceptible atoms such as copper to occur. For nickel corrosion, the initial step is nickel hydration to facilitate dissolution and this can occur when water transport into the material is enhanced. The transport of water is dependent on chloride environment. This was observed when we compared the potentiodynamic polarization of Sn-Cu-Ni alloy in neutral chloride-containing medium ($E_{\text{corr}} = -0.776$ V versus Ag/AgCl, $I_{\text{corr}} = 8.982 \mu\text{A}/\text{cm}^2$) and in acidic chloride-free electrolyte (0.1 M HNO₃; $E_{\text{corr}} = -0.356$ V versus Ag/AgCl, $I_{\text{corr}} = 4.34 \mu\text{A}/\text{cm}^2$). A sudden shift of corrosion potential to a less negative value is observed attributed to the formation of the passivation film. The absence of chloride in HNO₃ medium promotes barrier creation preventing hydration and corrosion to occur. This suggests that Sn-Cu-Ni alloy has high corrosion resistance in an acidic chloride-free environment. Chlorides even in small amounts can break the protective films initiating the occurrence of corrosion.

3.2. Soldering Properties and Leaching Measurements. During the preparation of the solder joints with copper substrates, a better surface finish of the joints was observed when Sn-Cu-Ni solder was used compared to Sn-Cu alloys. The design of adding Ni to common Sn-Cu alloy improved the soldering property [32]. These observations were consistent with the unique morphology of the intermetallic compound (IMC) layer reported by Harcuba et al. [33]. The IMC was described as noncompact islands of solder entrapped in the IMC phase and that the IMC layer contains more Ni than the solder. Nickel addition promoted the significant acceleration of the growth kinetics of the IMC layer.

The solder joints and the raw Pb-free solder alloys were subjected to corrosive media immersion to determine the leaching behaviour (Figure 7). The amount of Sn leached correlates with the corrosion rate of the alloys [25, 29, 34]. Since the results of potentiodynamic polarization test showed that all of the three Pb-free solders had higher corrosion rate than the Sn-Pb solder and Sn metal, leaching amounts of Sn were done only for the Pb-free solders. The leaching amounts of Sn after immersion in 3.5 wt.% NaCl solution after 30 days are observed to be greater for solder joints compared to its corresponding alloy. Sn-Ag-Cu alloy had the highest leaching

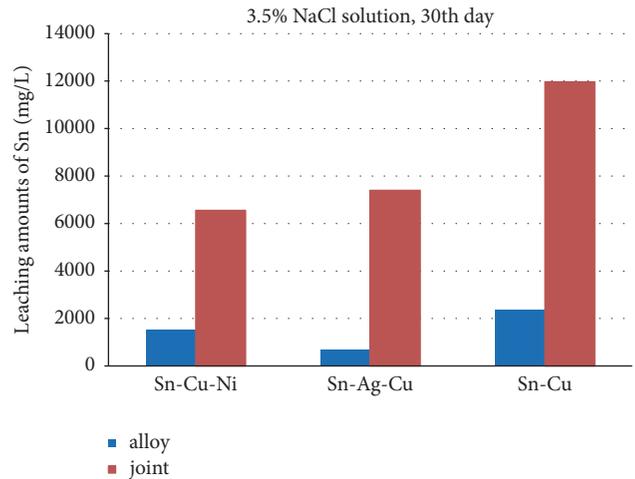


FIGURE 7: Atomic Absorption Spectroscopy (AAS) results on Tin (Sn) leaching from lead-free solder alloy and joint after 30 days.

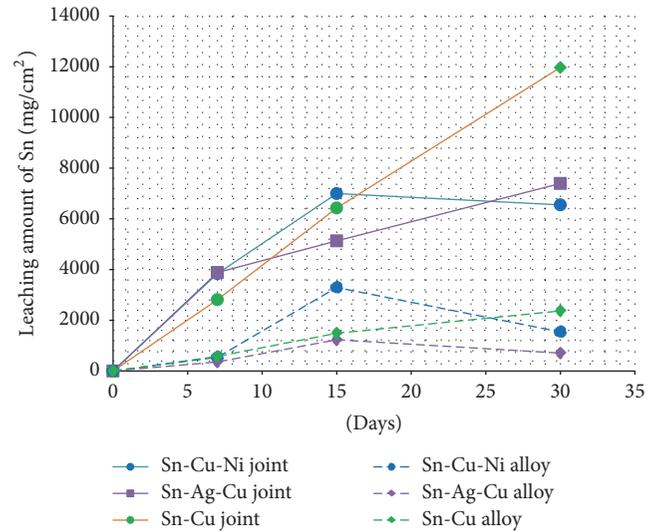


FIGURE 8: Leaching kinetics of Sn from Sn-Ag-Cu, Sn-Cu-Ni, and Sn-Cu alloy and their joints in 3.5 wt.% NaCl solution.

of Sn for the solder alloys followed by Sn-Cu alloy while Sn-Cu-Ni had the lowest leaching amount after 30 days. For solder joints, leached Sn follows the order Sn-Cu > Sn-Ag-Cu > Sn-Cu-Ni.

Leaching kinetics of Sn from the metals (Figure 8) show that solder joints gave a higher amount of leached Sn compared to their alloy counterparts. The use of Cu-substrate in the solder joint setup affects the leaching behaviour of Sn. This is because dissimilar metals having different oxidation potentials in contact with each other experience galvanic corrosion [25, 29], which does not occur in solder alloys alone. According to Lao et al., [29] the current density of the solder joint is almost twofold higher than its corresponding solder alloy. Thus, the galvanic cell (anode = Sn; cathode = Cu) accelerates the leaching amount of Sn from the joint.

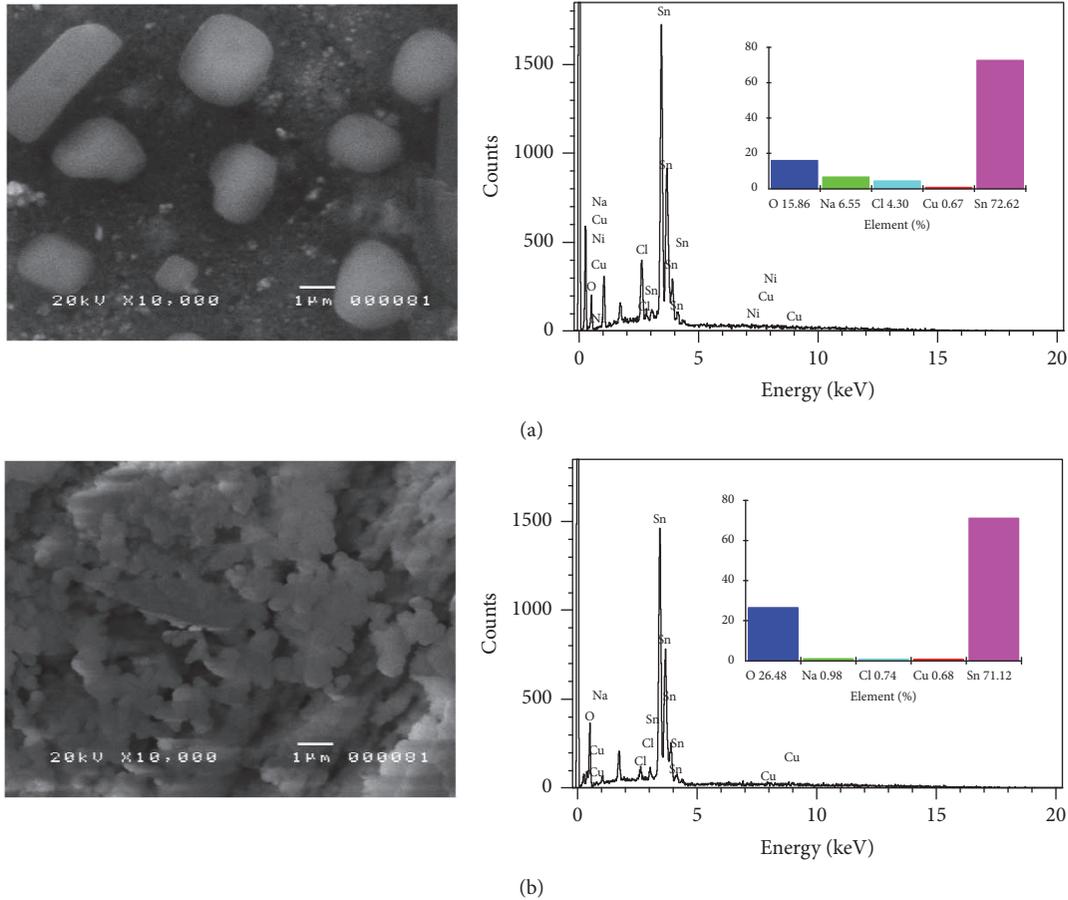


FIGURE 9: Surface morphology analysis of Sn-Cu-Ni (a) solder alloy and (b) solder joint and their corresponding EDS spectra after 30-day leaching measurements in 3.5 wt.% NaCl solution.

The microstructure analysis of Sn-Ni-Cu solder after 30-day immersion in NaCl solution (Figure 9) showed a more corroded surface for the joint and microstructure is composed of platelet-like materials on the surface. EDS analysis on the surface showed high amounts of Sn and O suggesting that the corrosion products are composed primarily of oxides of Sn and small amounts of chlorides. This is further confirmed by the detection of XRD patterns specific to SnO_2 (Figure 10). Similarly, corresponding peaks for Sn(OH)_2 were detected from Yan and Xian [28].

3.2.1. Microstructure of Corrosion Products on Solder Surface.

The microstructures of the corrosion surface were monitored as the exposure to the corrosive media increases. Generally, as the alloy (Figure 11) was exposed to the salt solution, the surface changed dramatically from smooth to porous with the formation of plate-like structures attributed to the weakly bonded corrosion products that form on the surface. These compounds, which have been identified in EDS and XRD as oxides of tin are typical corrosion products. The formation of these compounds is a result of a charge transfer reaction between Sn metal, salt ion, atmospheric O_2 , and H_2O during anodic polarization following the mechanism proposed by Mohran et al. [35]. These corrosion products

are weakly held by the bulk metal and can easily chip-off into the solution in agreement with the leaching experiments. The microstructural changes that can be observed for Sn-Cu-Ni are the noticeable degree of high corrosion product (platelet-like structure) after 7-day exposure compared to Sn-Ag-Cu and Sn-Cu. The corrosion products are formed along the cracks, which allow the water to seep-in triggering the corrosion reaction. As the exposure time increases, the entire surface was covered with corrosion products.

For the solder joints, the microstructure changes were likewise monitored (Figure 12). A more dramatic morphology can be observed characterized by branched crystallites, sponge-like structure, networked branches, and platelet-like materials. The formation of these microstructures occurs within 7-day exposure and increases gradually as time increases. This is the consequence of galvanic reaction that occurs since the solder joints are in contact with the Cu metal as substrate. The galvanic reaction triggers the very fast corrosion process. The EDS analysis of these microstructures reveals O and Sn-rich surface indicating oxides of Sn formation, which was further confirmed by XRD as SnO_2 (Figure 10).

Generally, the surfaces of the alloys show some corrosion product as evidenced by the plate-like structures. The surfaces

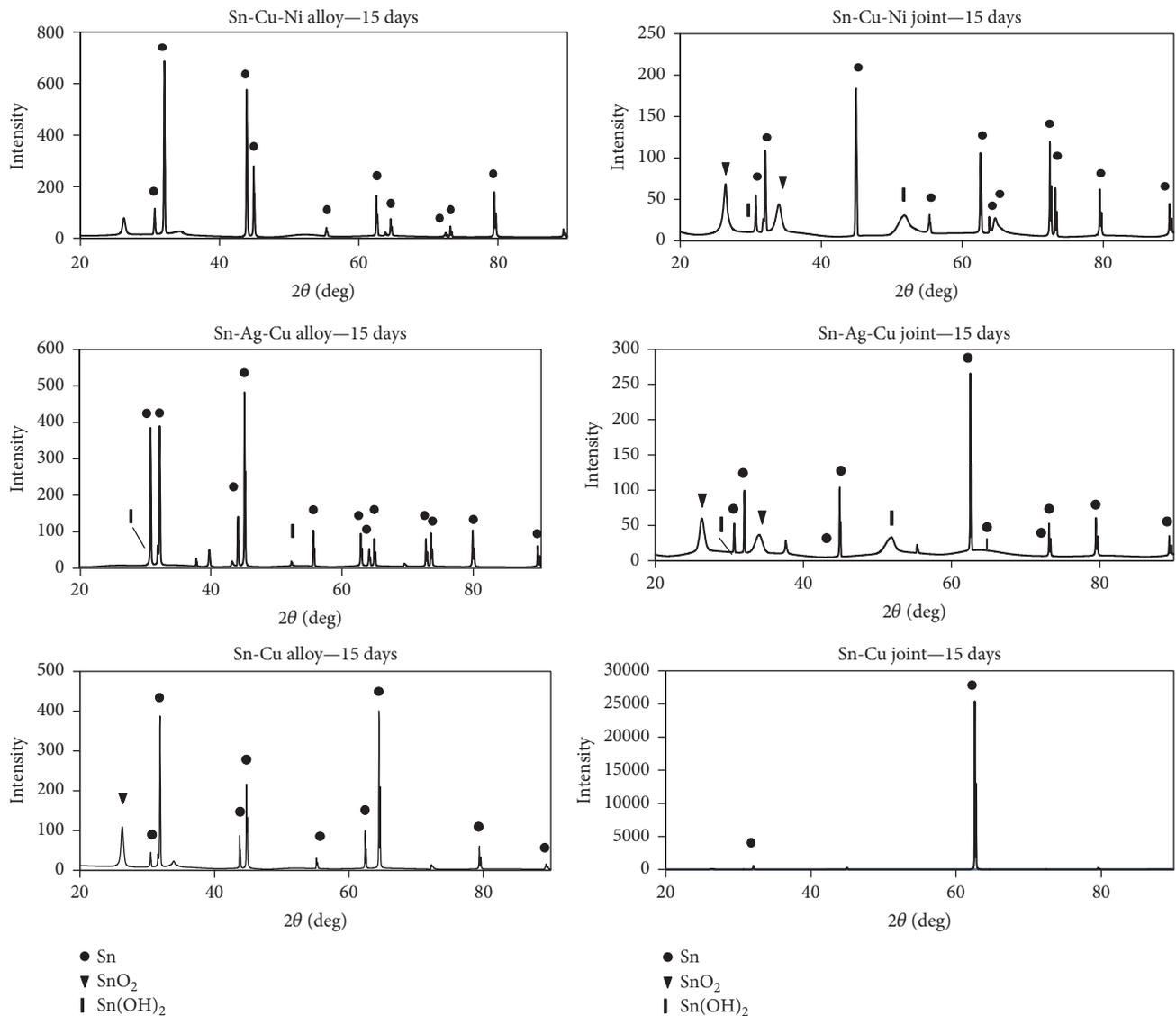


FIGURE 10: XRD patterns of surface product of Sn-Ag-Cu, Sn-Cu-Ni, and Sn-Cu solder alloy and joint after 15-day immersion in 3.5 wt.% NaCl solution.

are covered by a small degree of corrosion layer suggesting minimal corrosion on the alloy surface. However, the surface of the joint showed a high degree of corrosion with the entire surface covered with corrosion products forming nanocrystals and sponges. Similar morphology was reported by Lao et al., [29] in the leaching measurement of Sn-0.75Cu solder alloy and joint in simulated soil solutions. The corrosion layer formed on the surface of the alloy forms a protecting film that has a shielding effect on the Sn ion transport between the solder and the solution. However, in the case of the solder joint, the loosely bound corrosion layer can break-off easily. The corrosion products that made up the surface would no longer protect the substrate resulting in plenty of leaching amounts of Sn coming from the solder joint.

The result of potentiodynamic polarization and leaching tests in 3.5 wt.% NaCl solution is conflicting. Results for the Tafel extrapolation show that Sn-Cu-Ni has the highest

corrosion rate, while the 30-day immersion of the solder alloy and joint in NaCl solution showed the lowest amount of leached Sn for all the solders understudied. This was attributed to the rapid analysis in an electrochemical process, where corrosion is forcibly induced on the surface of the metal by applying voltage. A rapid measurement can influence the formation of the passivation film on the surface of the metal. On the other hand, the long exposure time with the corrosive media in leaching experiments allows an actual electrochemical process to occur and measured progressively. In these conditions, the formation of corrosion product is gradual and there is longer timeframe for the stabilization and formation of the passivation film.

These results are significant since, in electronic processes, the solder alloy is not used alone. Rather it is used in contact with other metals mostly Cu in most electronic substrates. These lead-free solders therefore, once in a corrosive media

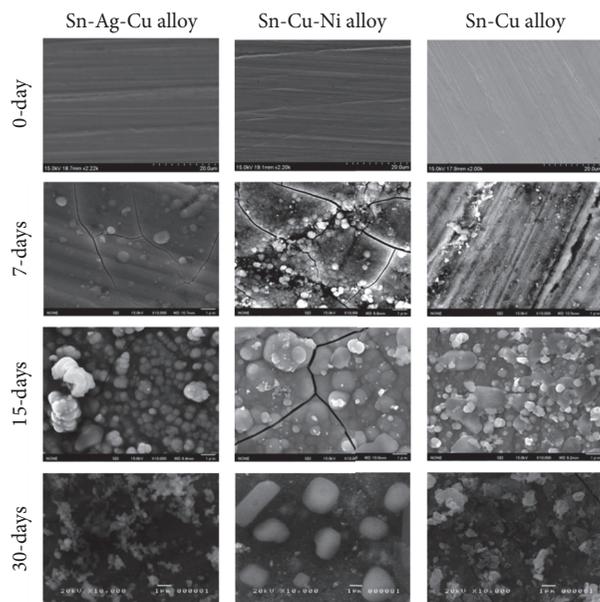


FIGURE 11: SEM image of lead-free solder alloy after 7, 15, and 30 days leaching measurement in 3.5 wt.% NaCl solution.

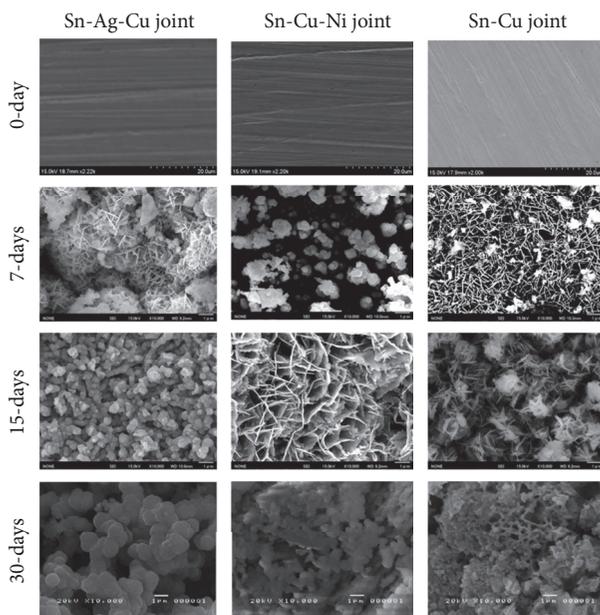


FIGURE 12: SEM image of lead-free solder joint after 7, 15, and 30 days leaching measurement in 3.5 wt.% NaCl solution.

such as aqueous NaCl atmosphere, are prone to corrosion even within 7 days of exposure. The corrosion reaction is triggered by the galvanic reaction that occurs when this happens inside an electronic gadget. The interconnections and electrical connectivity are lost affecting the form, features, and function of the device.

4. Conclusions

The corrosion behaviour of Sn-Cu-Ni lead-free solder was described for the first time. In 3.5 wt.% NaCl environment,

potentiodynamic polarization test revealed that the new Sn-Cu-Ni solder has higher corrosion rate compared to Sn-Cu and Sn-Ag-Cu. However, longer exposure of the Sn-Cu-Ni alloy and joint to the corrosive medium for up to 30 days showed the lowest leaching rate of Sn compared to Sn-Cu and Sn-Ag-Cu solders. Generally, alloys have lower leaching rate compared to the corresponding joint due to the galvanic reaction occurring in the joint setup. For chloride-containing solution, the corrosion and leaching behaviour of Sn-Ag-Cu is better compared to Sn-Ni-Cu and Sn-Cu. Further study is underway in acidic and basic media and will be reported elsewhere.

Conflicts of Interest

There are no conflicts of interest related to this paper.

Acknowledgments

This work was supported by the Accelerated Science and Technology Human Resource Development Program (ASTHRDP) of the Department of Science and Technology, Science Education Institute (DOST-SEI). Jan-Ervin C. Guerrero is grateful for the Japan Sakura Science Program.

References

- [1] M. Abtey and G. Selvaduray, "Lead-free solders in micro-electronics," *Materials Science and Engineering: A Structural Materials: Properties, Microstructure and Processing*, vol. 27, no. 5, pp. 95–141, 2000.
- [2] S. Tong, Y. von Schirnding, and T. Prapamontol, "Environmental lead exposure: a public health problem of global dimensions," *Bulletin of the World Health Organization*, 2000, [http://www.who.int/bulletin/archives/78\(9\)1068.pdf](http://www.who.int/bulletin/archives/78(9)1068.pdf).
- [3] J. H. Lau and K. Liu, "Global Trends in Lead-free soldering," *International Journal of Advanced Packaging Technology*, vol. 13, no. 2, pp. 25–28, 2004.
- [4] S. Garesan and M. Pecht, *Lead Free Electronics*, IEEE Press/John Wiley & Sons, Inc, Hoboken, NJ, USA, 2006.
- [5] K. Sukanuma, "Advances in lead-free electronics soldering," *Current Opinion in Solid State & Materials Science*, vol. 5, no. 1, pp. 55–64, 2001.
- [6] N. Chawla, "Thermomechanical behaviour of environmentally benign Pb-free solders," *International Materials Reviews*, vol. 54, no. 6, pp. 368–384, 2009.
- [7] K. Zeng and K. N. Tu, "Six cases of reliability study of Pb-free solder joints in electronic packaging technology," *Materials Science and Engineering: Reports*, vol. 38, no. 2, pp. 55–106, 2002.
- [8] D. K. Mu, S. D. McDonald, J. Read, H. Huang, and K. Nogita, "Critical properties of Cu₆Sn₅ in electronic devices: recent progress and a review," *Current Opinion in Solid State & Materials Science*, vol. 20, no. 2, pp. 55–76, 2016.
- [9] H. R. Kotadia, P. D. Howes, and S. H. Mannan, "A review: on the development of low melting temperature Pb-free solders," *Microelectronics Reliability*, vol. 54, no. 6-7, pp. 1253–1273, 2014.
- [10] G. Zeng, S. McDonald, and K. Nogita, "Development of high-temperature solders: review," *Microelectronics Reliability*, vol. 52, no. 7, pp. 1306–1322, 2012.

- [11] H. Nishikawa, J. Y. Piao, and T. Takemoto, "Effect of Ni addition on interfacial reaction between Sn-Cu solder and Cu base metal," in *Joining of Advanced and Specialty Materials VII, Proceedings from Materials Solutions 2004 on Joining of Advanced and Specialty Materials*, T. J. Lienert, Ed., vol. 35, pp. 208–211, Columbus, OH, USA, October 2006.
- [12] B. L. Silva, N. Cheung, A. Garcia, and J. E. Spinelli, "Evaluation of solder/substrate thermal conductance and wetting angle of Sn-0.7 wt%Cu-(0–0.1 wt%Ni) solder alloys," *Materials Letters*, vol. 142, pp. 163–167, 2015.
- [13] J.-W. Yoon, B.-I. Noh, B.-K. Kim, C.-C. Shur, and S.-B. Jung, "Wettability and interfacial reactions of Sn-Ag-Cu/Cu and Sn-Ag-Ni/Cu solder joints," *Journal of Alloys and Compounds*, vol. 486, no. 1–2, pp. 142–147, 2009.
- [14] L. Yang, J. Ge, Y. Zhang, J. Dai, H. Liu, and J. Xiang, "Investigation on the Microstructure, Interfacial IMC Layer, and Mechanical Properties of Cu/Sn-0.7Cu-xNi/Cu Solder Joints," *Journal of Electronic Materials*, vol. 45, no. 7, pp. 3766–3775, 2016.
- [15] H. Nishikawa, J. Y. Piao, and T. Takemoto, "Interfacial reaction between Sn-0.7Cu (-Ni) solder and Cu substrate," *Journal of Electronic Materials*, vol. 35, no. 5, pp. 1127–1132, 2006.
- [16] S. Farina and C. Morando, "Comparative corrosion behaviour of different Sn-based solder alloys," *Journal of Materials Science: Materials in Electronics*, vol. 26, no. 1, pp. 464–471, 2014.
- [17] K. Pietrzak, M. Grobelny, K. Makowska et al., "Structural aspects of the behavior of lead-free solder in the corrosive solution," *Journal of Materials Engineering and Performance*, vol. 21, no. 5, pp. 648–654, 2012.
- [18] M. Reid and L. F. Garfias-Mesias, "Corrosion of electronics: lead-free initiatives," in *Uhlig's Corrosion Handbook*, R. W. Revie, Ed., pp. 565–570, John Wiley & Sons, Inc, Hoboken, NJ, USA, 3rd edition, 2011.
- [19] K.-L. Lin and T.-P. Liu, "The electrochemical corrosion behaviour of Pb-free Al-Zn-Sn solders in NaCl solution," *Materials Chemistry and Physics*, vol. 56, no. 2, pp. 171–176, 1998.
- [20] D. Li, P. P. Conway, and C. Liu, "Corrosion characterization of tin-lead and lead free solders in 3.5 wt.% NaCl solution," *Corrosion Science*, vol. 50, no. 4, pp. 995–1004, 2008.
- [21] W. R. Osório, E. S. Freitas, J. E. Spinelli, and A. Garcia, "Electrochemical behavior of a lead-free Sn-Cu solder alloy in NaCl solution," *Corrosion Science*, vol. 80, pp. 71–81, 2014.
- [22] M. Liu, W. Yang, Y. Ma, C. Tang, H. Tang, and Y. Zhan, "The electrochemical corrosion behavior of Pb-free Sn-8.5Zn-XCr solders in 3.5 wt.% NaCl solution," *Materials Chemistry and Physics*, vol. 168, pp. 27–34, 2015.
- [23] A. Kamarul Asri and E. Hamzah, "Corrosion behaviour of lead-free and Sn-Pb solders in 3.5wt% NaCl," *Advanced Materials Research*, vol. 686, pp. 250–260, 2013.
- [24] U. S. Mohanty and K.-L. Lin, "Electrochemical corrosion behaviour of Pb-free Sn-8.5Zn-0.05Al-XGa and Sn-3Ag-0.5Cu alloys in chloride containing aqueous solution," *Corrosion Science*, vol. 50, no. 9, pp. 2437–2443, 2008.
- [25] C. Q. Cheng, F. Yang, J. Zhao, L. H. Wang, and X. G. Li, "Leaching of heavy metal elements in solder alloys," *Corrosion Science*, vol. 53, no. 5, pp. 1738–1747, 2011.
- [26] A. Wierzbicka-Miernik, J. Guspiel, and L. Zabdyr, "Corrosion behavior of lead-free SAC-type solder alloys in liquid media," *Archives of Civil and Mechanical Engineering*, vol. 15, no. 1, pp. 206–213, 2015.
- [27] A. Sharma, S. Das, and K. Das, "Electrochemical corrosion behavior of CeO₂ nanoparticle reinforced Sn-Ag based lead free nanocomposite solders in 3.5wt.% NaCl bath," *Surface and Coatings Technology*, vol. 261, pp. 235–243, 2015.
- [28] Z. Yan and A.-P. Xian, "Corrosion of Ga-doped Sn-0.7Cu solder in simulated marine atmosphere," *Metallurgical and Materials Transactions A: Physical Metallurgy and Materials Science*, vol. 44, no. 3, pp. 1462–1474, 2013.
- [29] X.-D. Lao, C.-Q. Cheng, X.-H. Min et al., "Corrosion and leaching behaviors of Sn-based alloy in simulated soil solutions," *Transactions of Nonferrous Metals Society of China*, vol. 26, no. 2, pp. 581–588, 2016.
- [30] F. Arjmand and A. Adriaens, "Influence of pH and chloride concentration on the corrosion behavior of unalloyed copper in NaCl solution: a comparative study between the micro and macro scales," *Materials*, vol. 5, no. 12, pp. 2439–2464, 2012.
- [31] B. D. Craig and D. S. Anderson, Eds., *Handbook of Corrosion Data*, ASM International, Materials Park, OH, USA, 2nd edition, 1995.
- [32] T. Ventura, C. M. Gourlay, K. Nogita, T. Nishimura, M. Rappaz, and A. K. Dahle, "The influence of 0-0.1 wt.% Ni on the microstructure and fluidity length of Sn-0.7Cu-xNi," *Journal of Electronic Materials*, vol. 37, no. 1, pp. 32–39, 2008.
- [33] P. Harcuba, M. Janeček, and M. Slámová, "The effect of Cu and Ni on the structure and properties of the IMC formed by the reaction of liquid Sn-Cu based solders with Cu substrate," in *Proceedings of Contributed Papers (WDS '08)*, part III, pp. 220–224, Prague, Czech, June 2008.
- [34] M. Mori, K. Miura, T. Sasaki, and T. Ohtsuka, "Corrosion of tin alloys in sulfuric and nitric acids," *Corrosion Science*, vol. 44, no. 4, pp. 887–898, 2002.
- [35] H. S. Mohran, A.-R. El-Sayed, and H. M. Abd El-Lateef, "Anodic behavior of tin, indium, and tin-indium alloys in oxalic acid solution," *Journal of Solid State Electrochemistry*, vol. 13, no. 8, pp. 1279–1290, 2009.